



(19) **United States**

(12) **Patent Application Publication**
Guo et al.

(10) **Pub. No.: US 2019/0319152 A1**
(43) **Pub. Date: Oct. 17, 2019**

(54) **SUPER-HYDROPHOBIC SURFACES AND METHODS FOR PRODUCING SUPER-HYDROPHOBIC SURFACES**

(71) Applicant: **University of Rochester**, Rochester, NY (US)

(72) Inventors: **Chunlei Guo**, Rochester, NY (US); **Anatoliy Y. Vorobyev**, Saint Catharines (CA)

(73) Assignee: **University of Rochester**, Rochester, NY (US)

(21) Appl. No.: **16/456,226**

(22) Filed: **Jun. 28, 2019**

Publication Classification

(51) **Int. Cl.**
H01L 31/054 (2006.01)
B23K 26/0622 (2006.01)
B23K 26/352 (2006.01)
C22F 3/00 (2006.01)
H01L 31/0232 (2006.01)
B23K 26/00 (2006.01)
B23K 26/082 (2006.01)

(52) **U.S. Cl.**
 CPC *H01L 31/0547* (2014.12); *B23K 26/0624* (2015.10); *B23K 26/3568* (2018.08); *B23K 26/355* (2018.08); *B23K 2103/12* (2018.08); *H01L 31/02327* (2013.01); *B23K 26/0006* (2013.01); *B23K 26/082* (2015.10); *C22F 3/00* (2013.01)

Related U.S. Application Data

(63) Continuation of application No. 14/593,465, filed on Jan. 9, 2015, which is a continuation-in-part of application No. 13/604,951, filed on Sep. 6, 2012, which is a continuation-in-part of application No. 12/188,258, filed on Aug. 8, 2008, now abandoned, which is a continuation-in-part of application No. 11/862,449, filed on Sep. 27, 2007, now abandoned.

(60) Provisional application No. 60/847,916, filed on Sep. 29, 2006.

(57) **ABSTRACT**

A metal or metal alloy including a region with hierarchical micro-scale and nano-scale structure shapes, the surface region is super-hydrophobic and has a spectral reflectance of less than 30% for at least some wavelengths of electromagnetic radiation in the range of 0.1 μm to 10 μm. Methods for forming the hierarchical micro-scale and nano-scale structure shapes on the metal or metal alloy are also described.

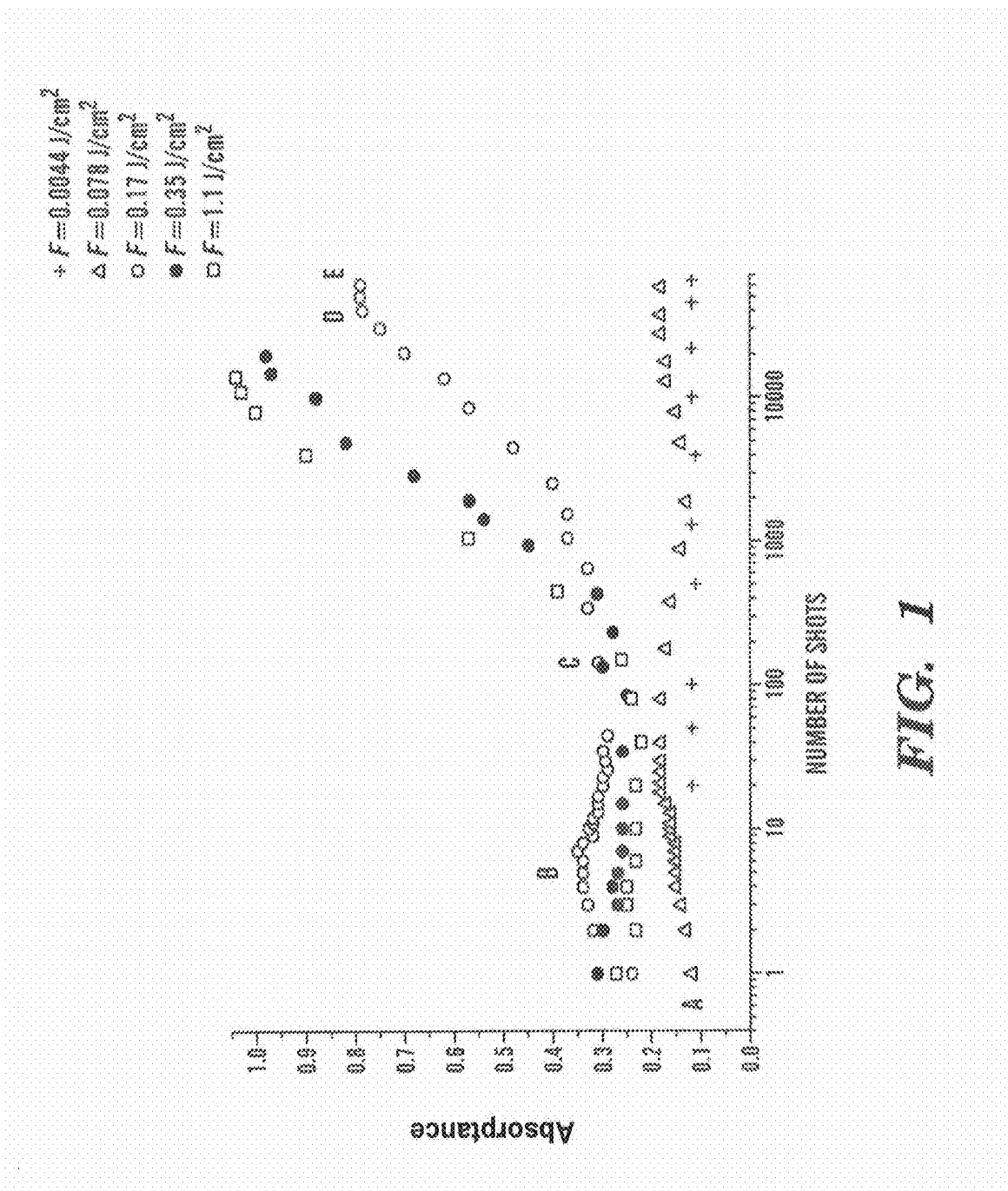


FIG. 1

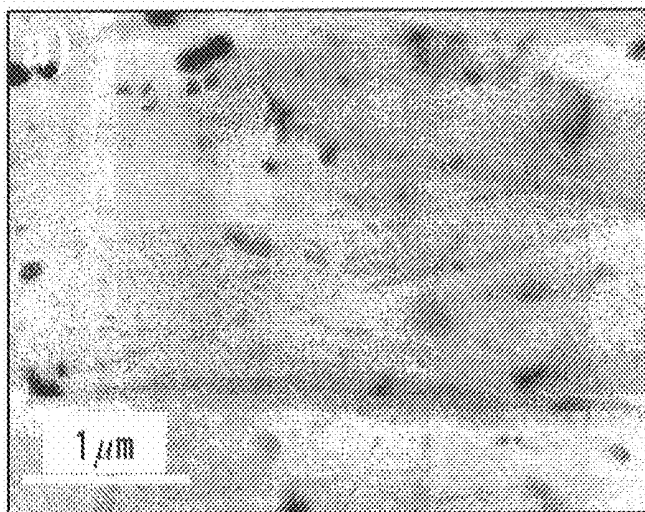


FIG. 2A

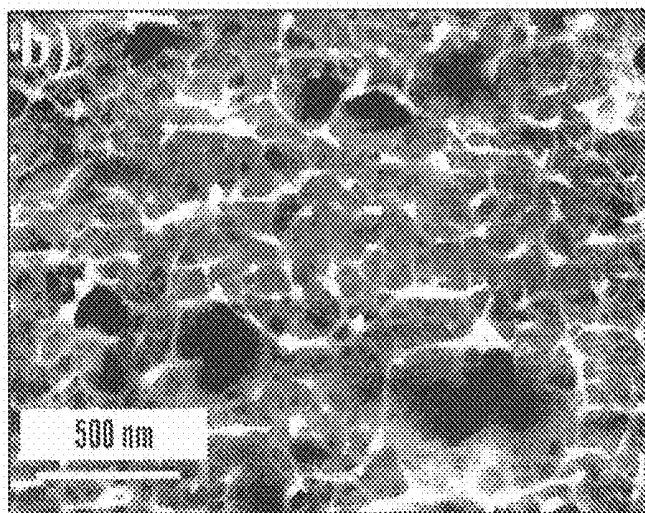


FIG. 2B

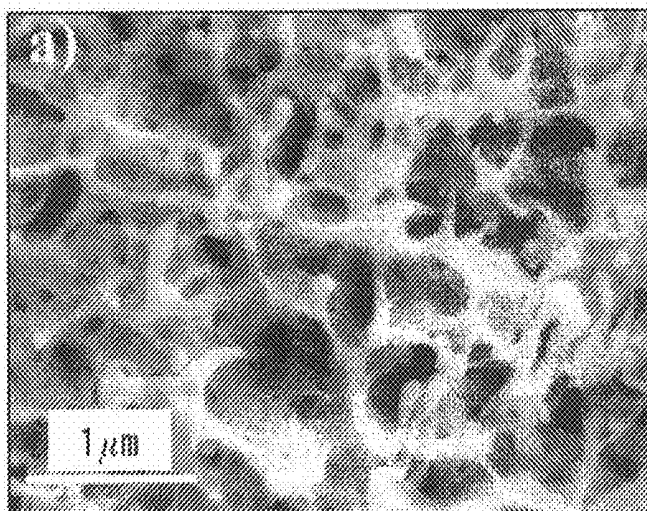


FIG. 3A

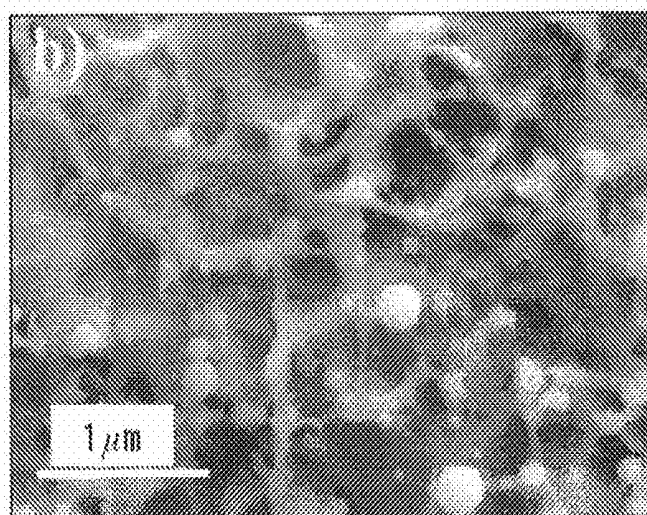


FIG. 3B

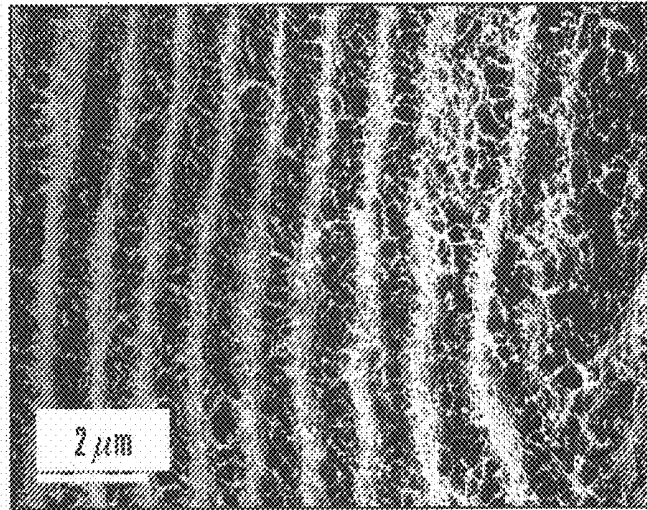


FIG. 4A

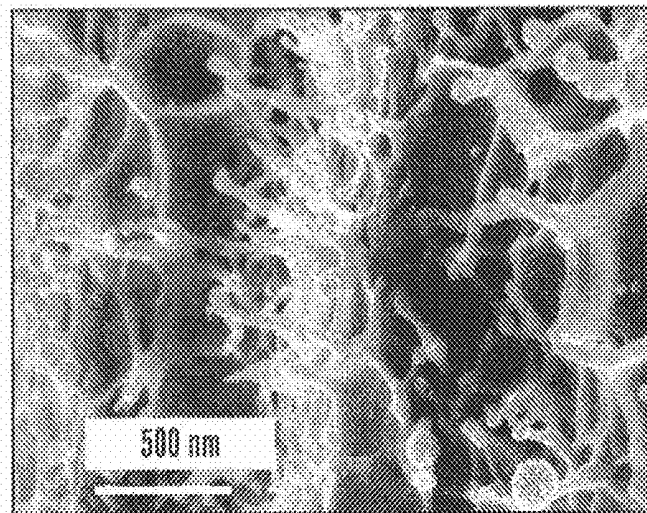


FIG. 4B

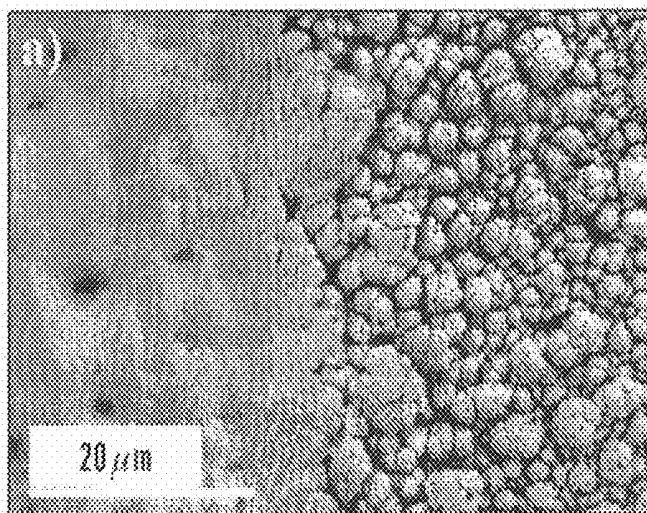


FIG. 5A

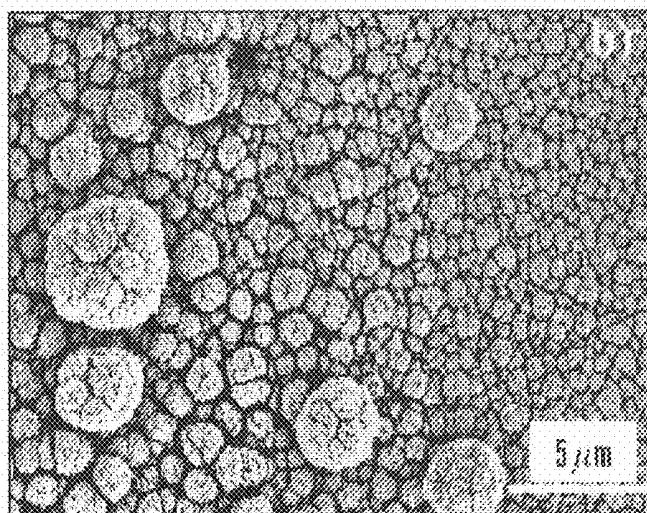


FIG. 5B

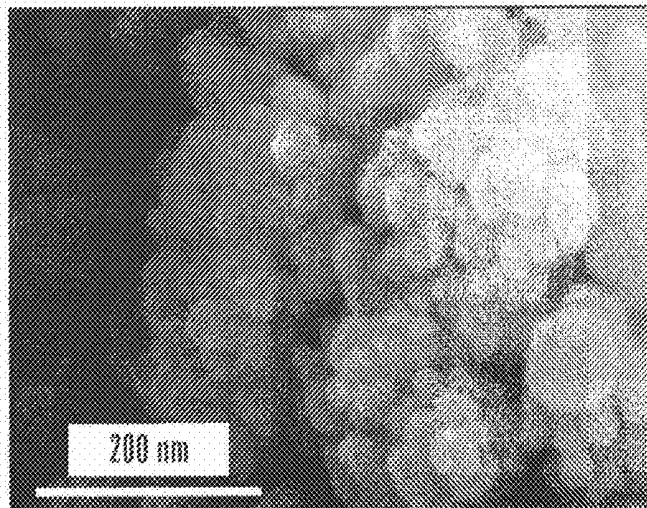


FIG. 6

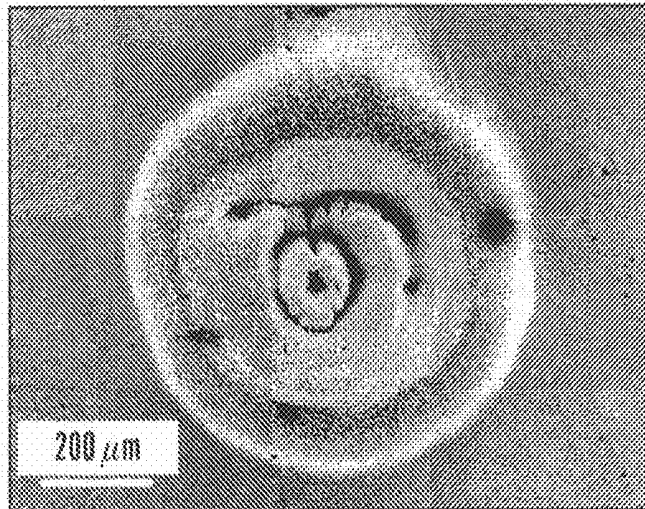


FIG. 7A

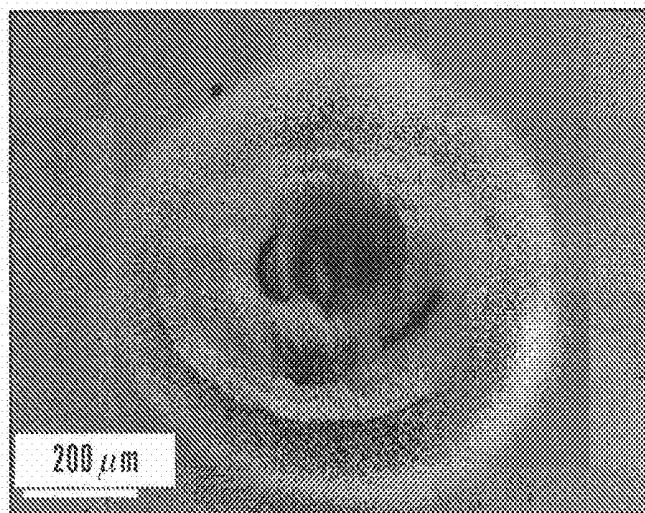


FIG. 7B

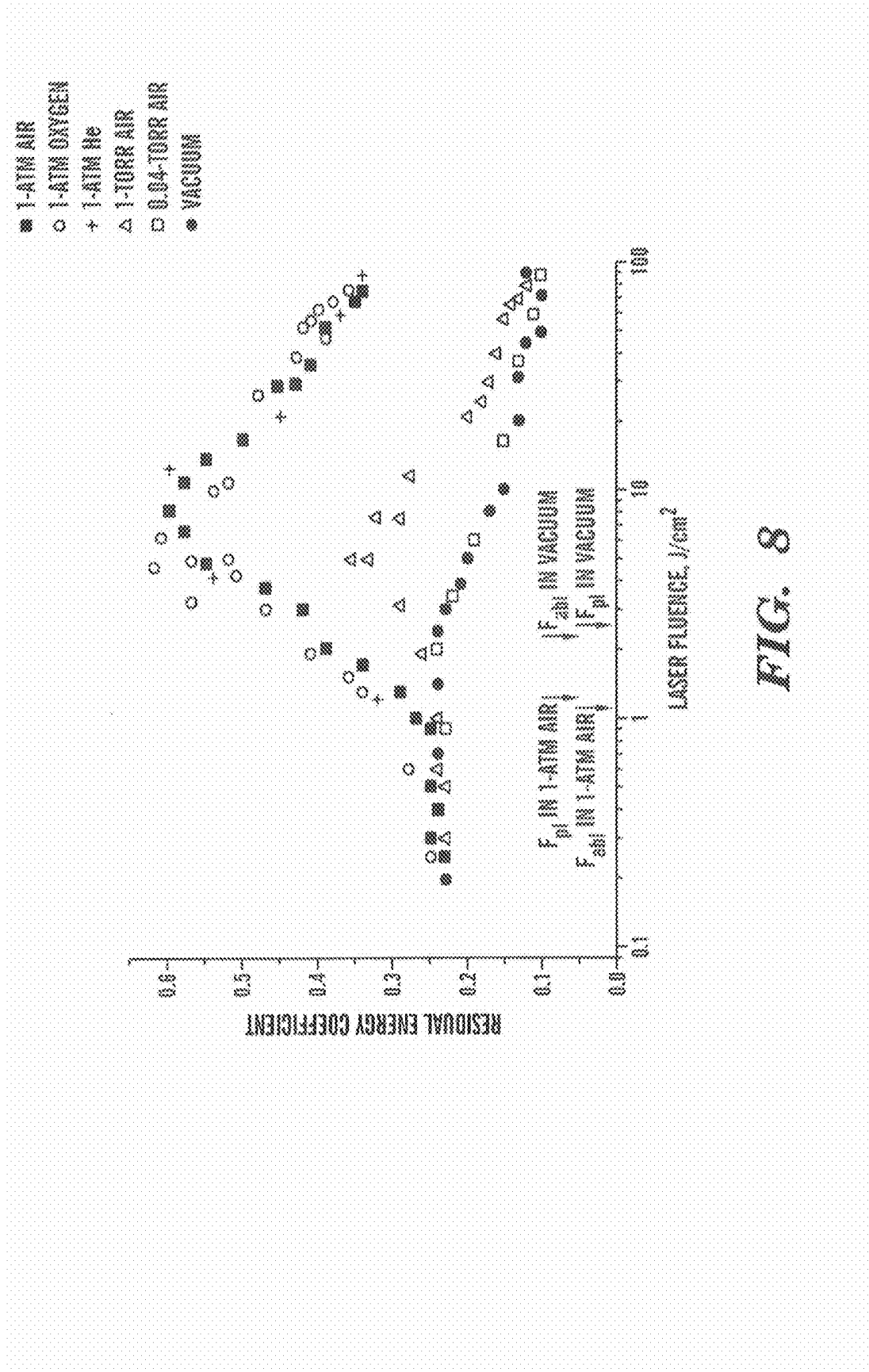


FIG. 8

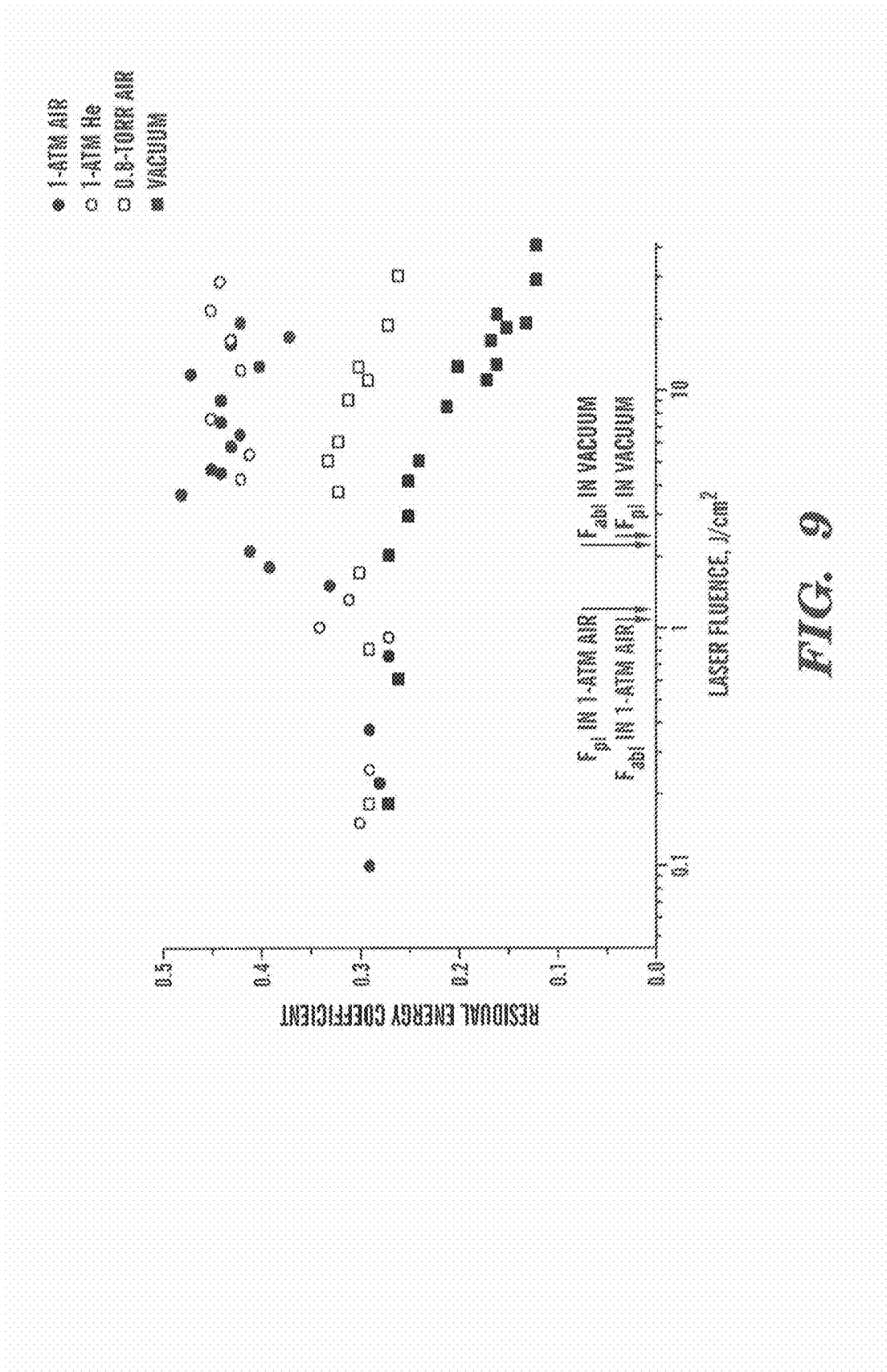


FIG. 9

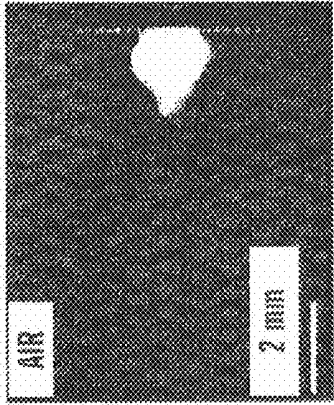
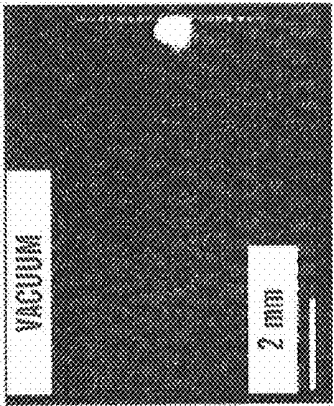


FIG. 10A

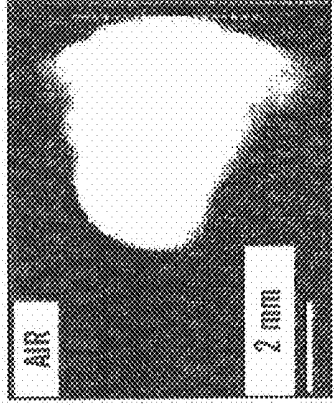
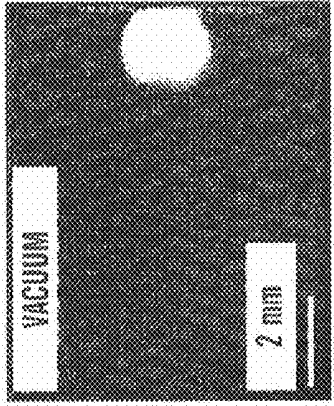


FIG. 10B

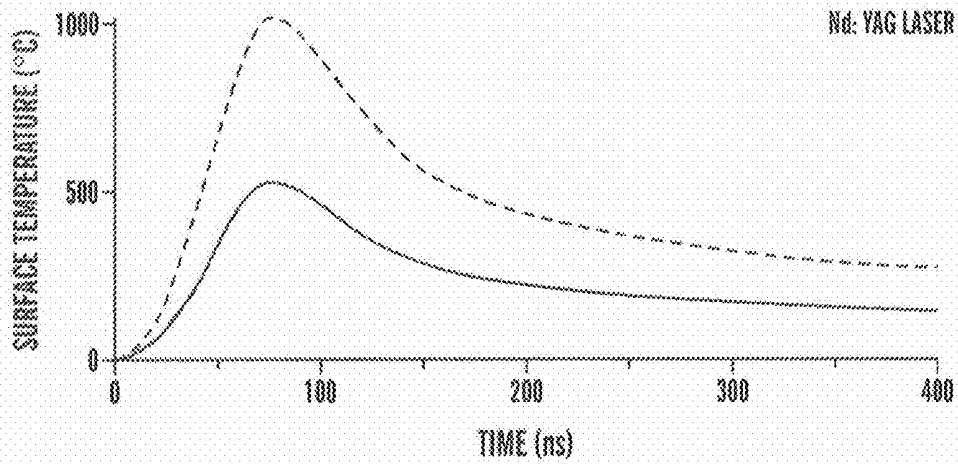


FIG. 11A

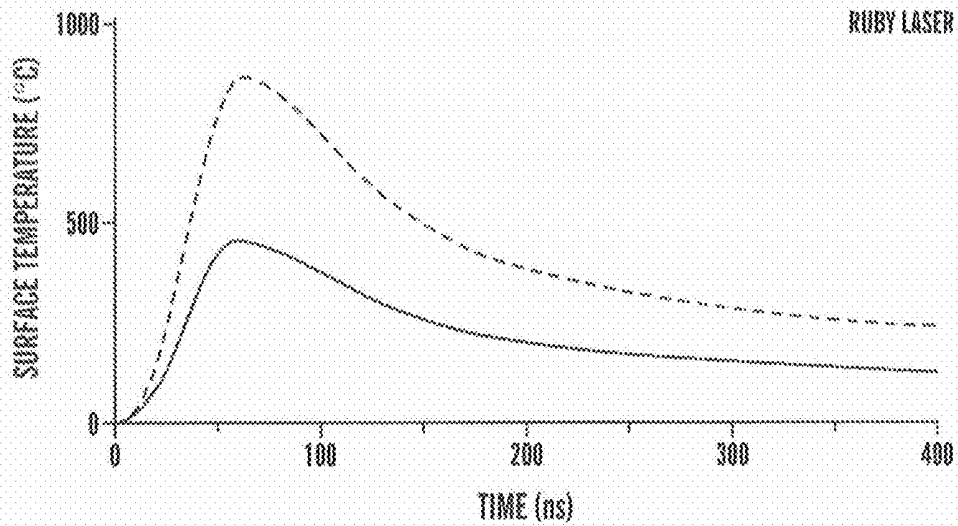


FIG. 11B

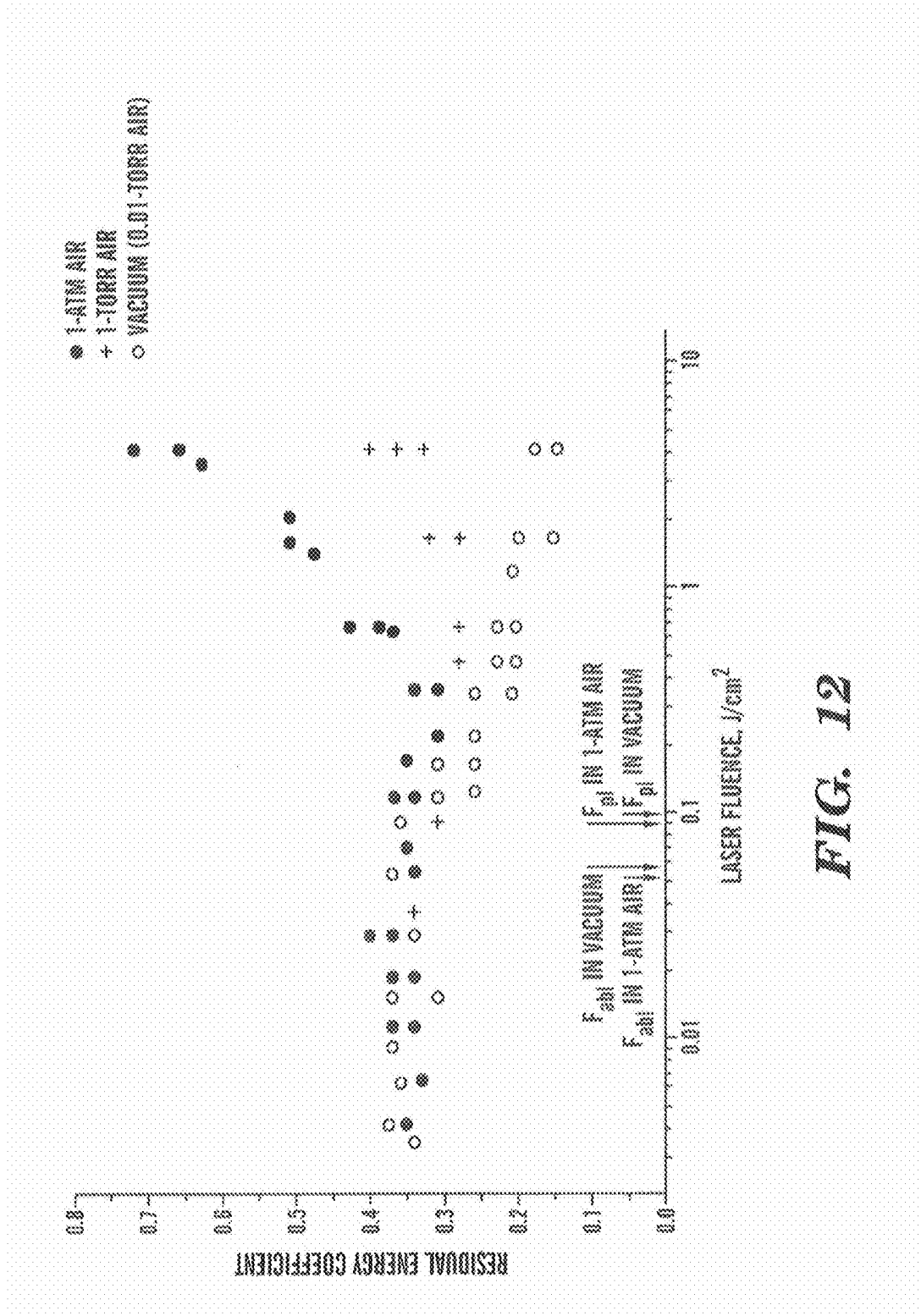


FIG. 12

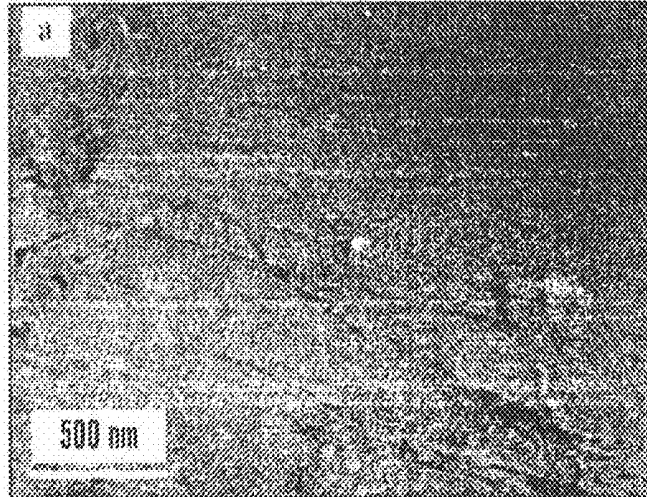


FIG. 13A

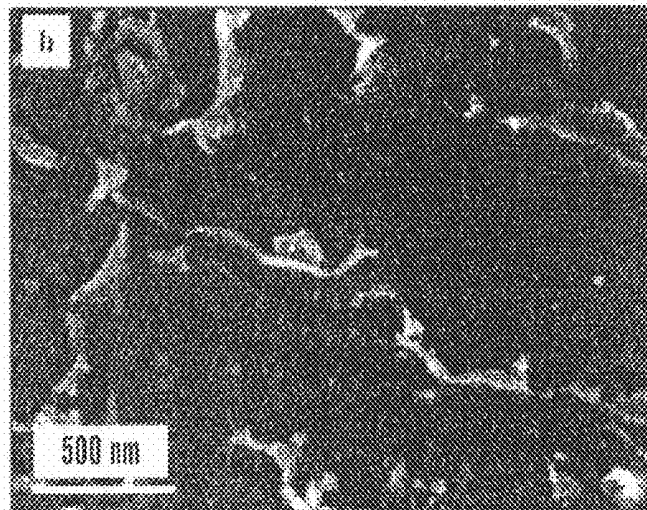


FIG. 13B

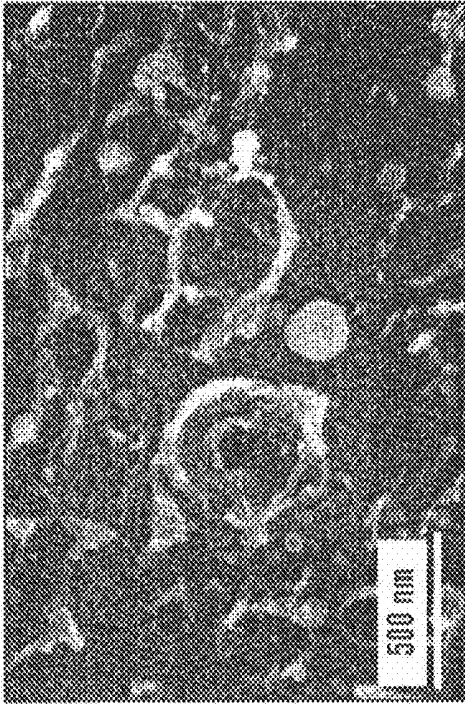


FIG. 14

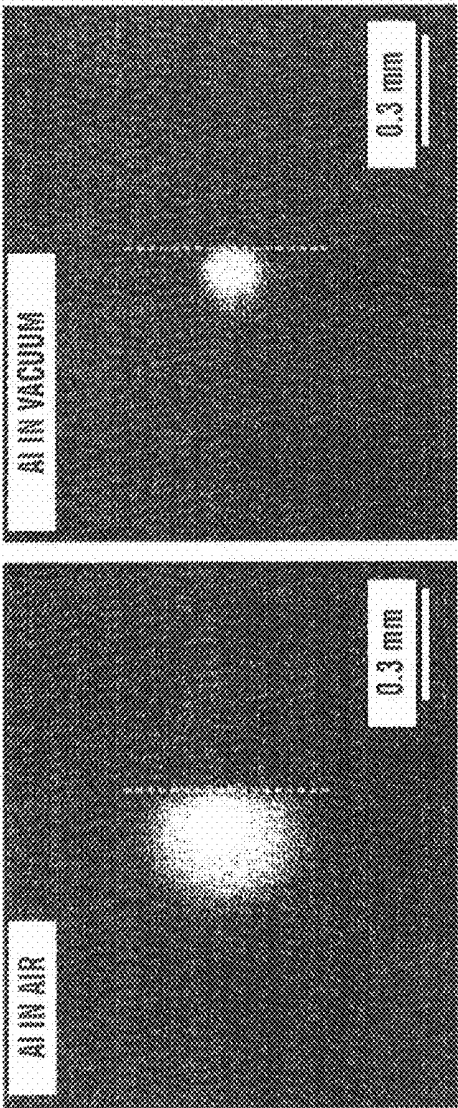


FIG. 15

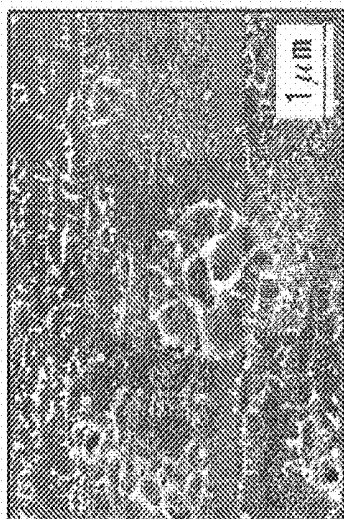


FIG. 16B

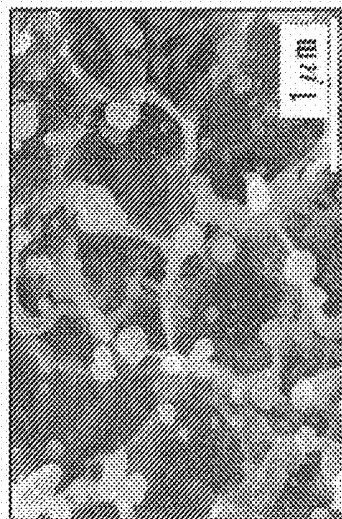


FIG. 16D

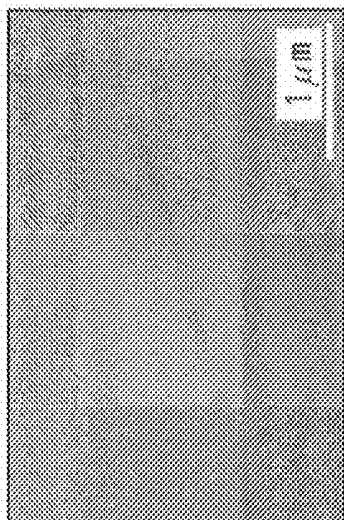


FIG. 16A

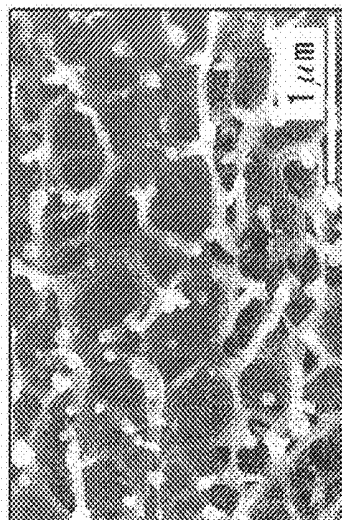


FIG. 16C

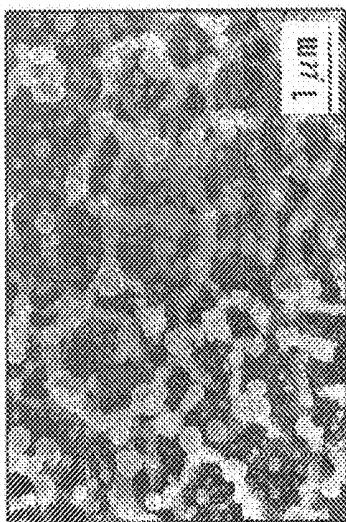


FIG. 17B



FIG. 17D

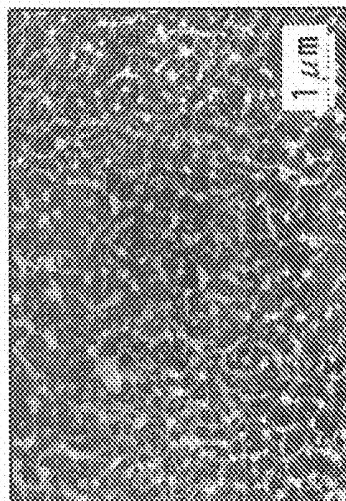


FIG. 17A

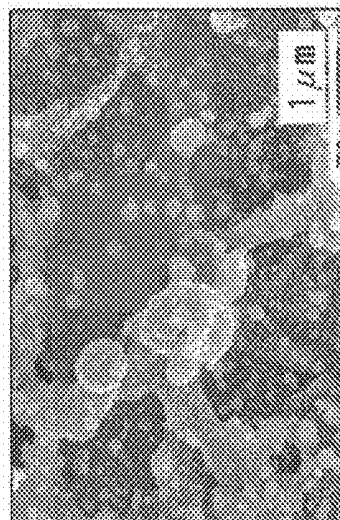


FIG. 17C

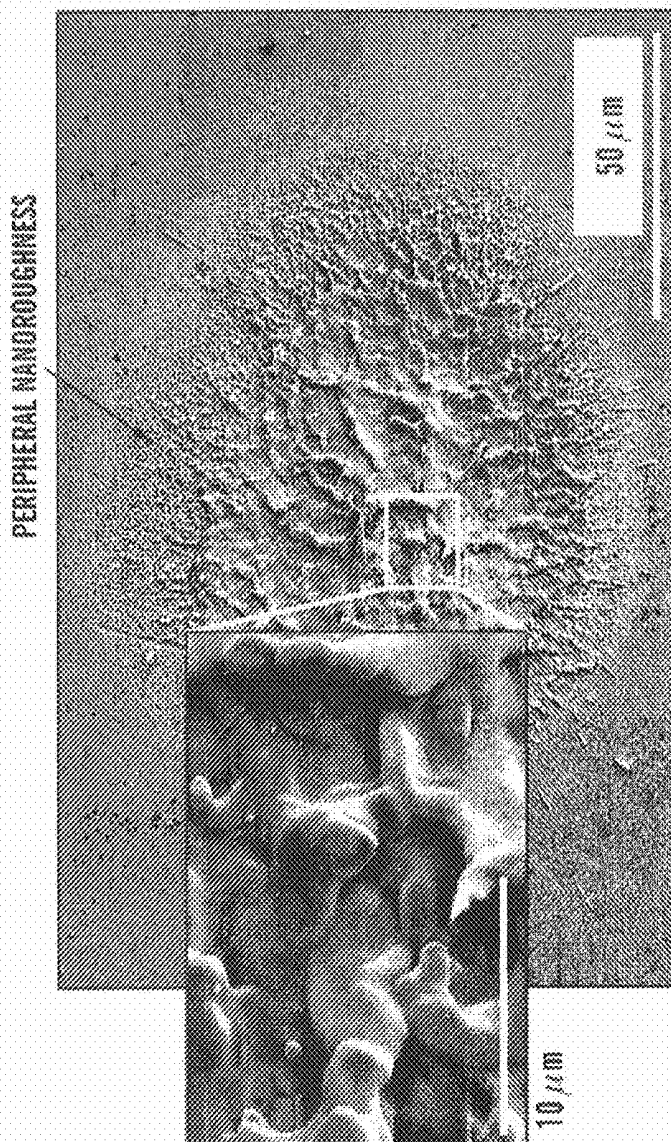


FIG. 18

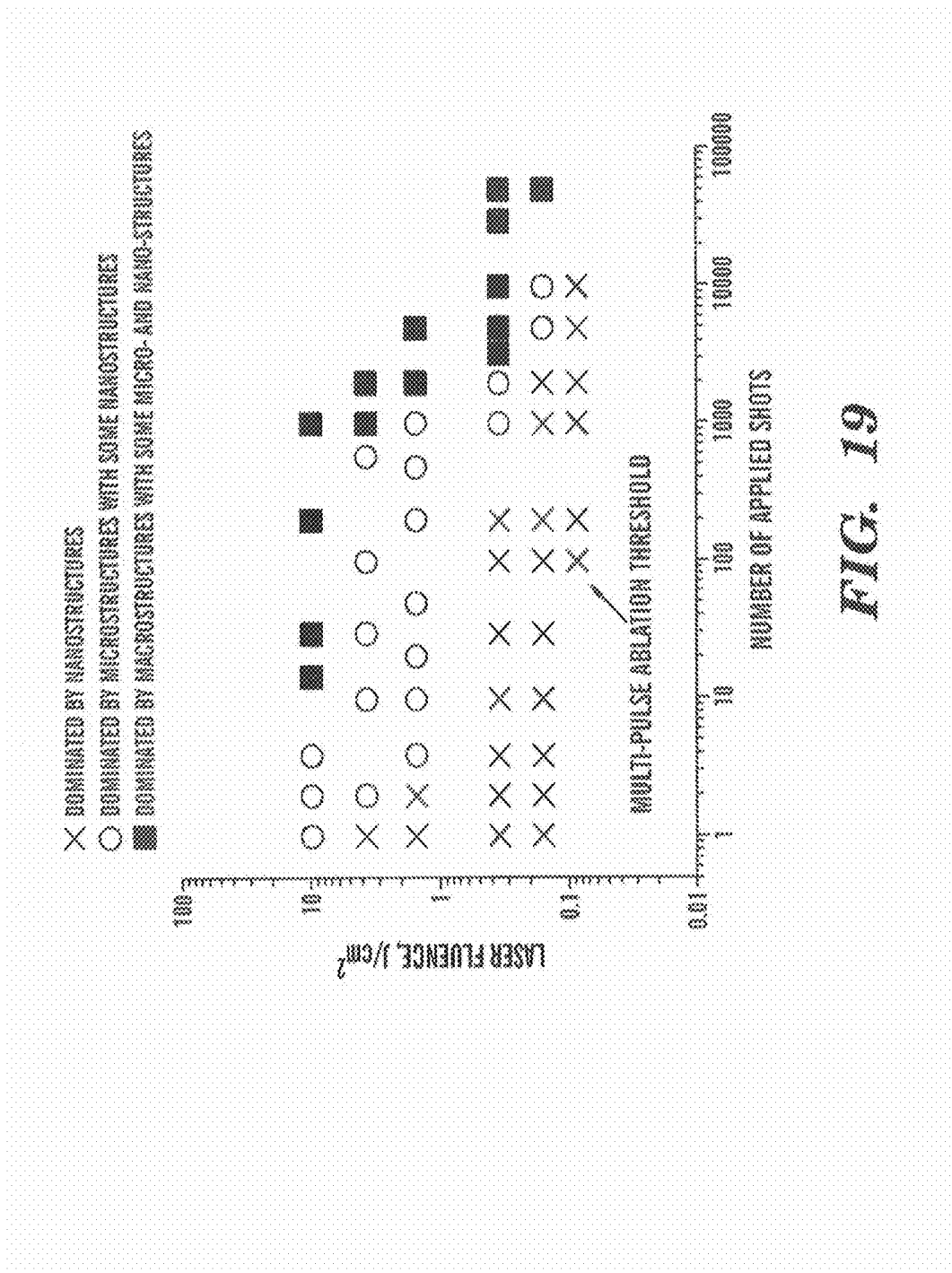


FIG. 19

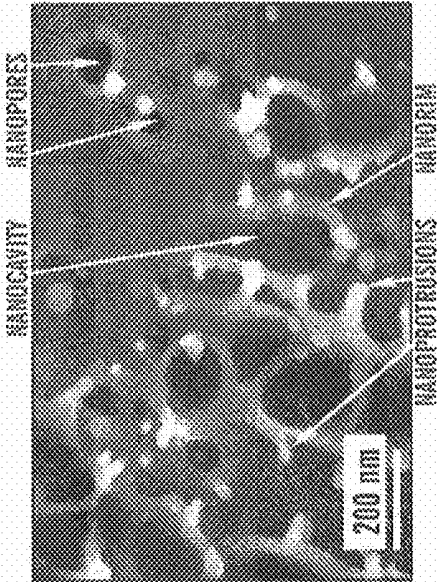


FIG. 20B



FIG. 20A

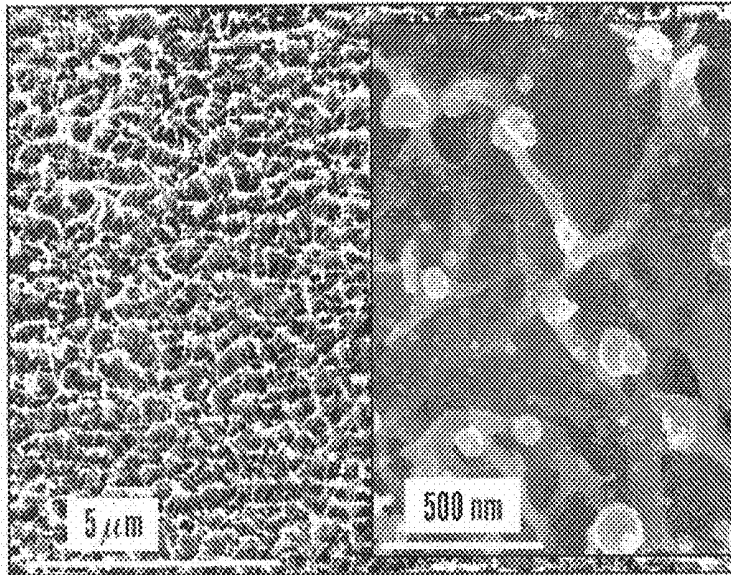


FIG. 21A

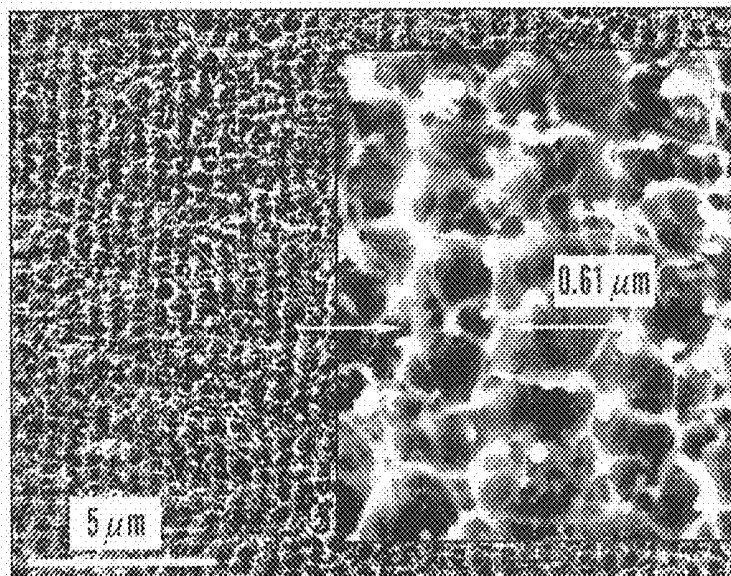


FIG. 21B

FIG. 22B

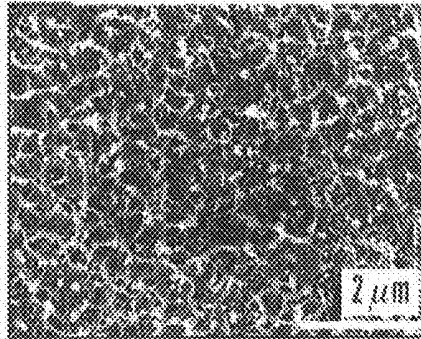


FIG. 22A

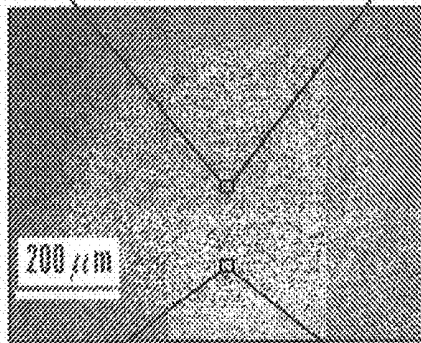


FIG. 22C

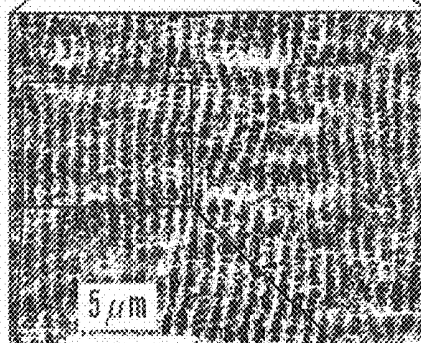
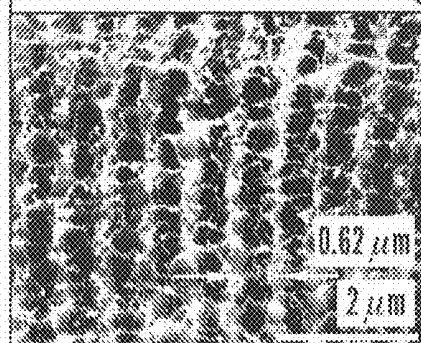


FIG. 22D



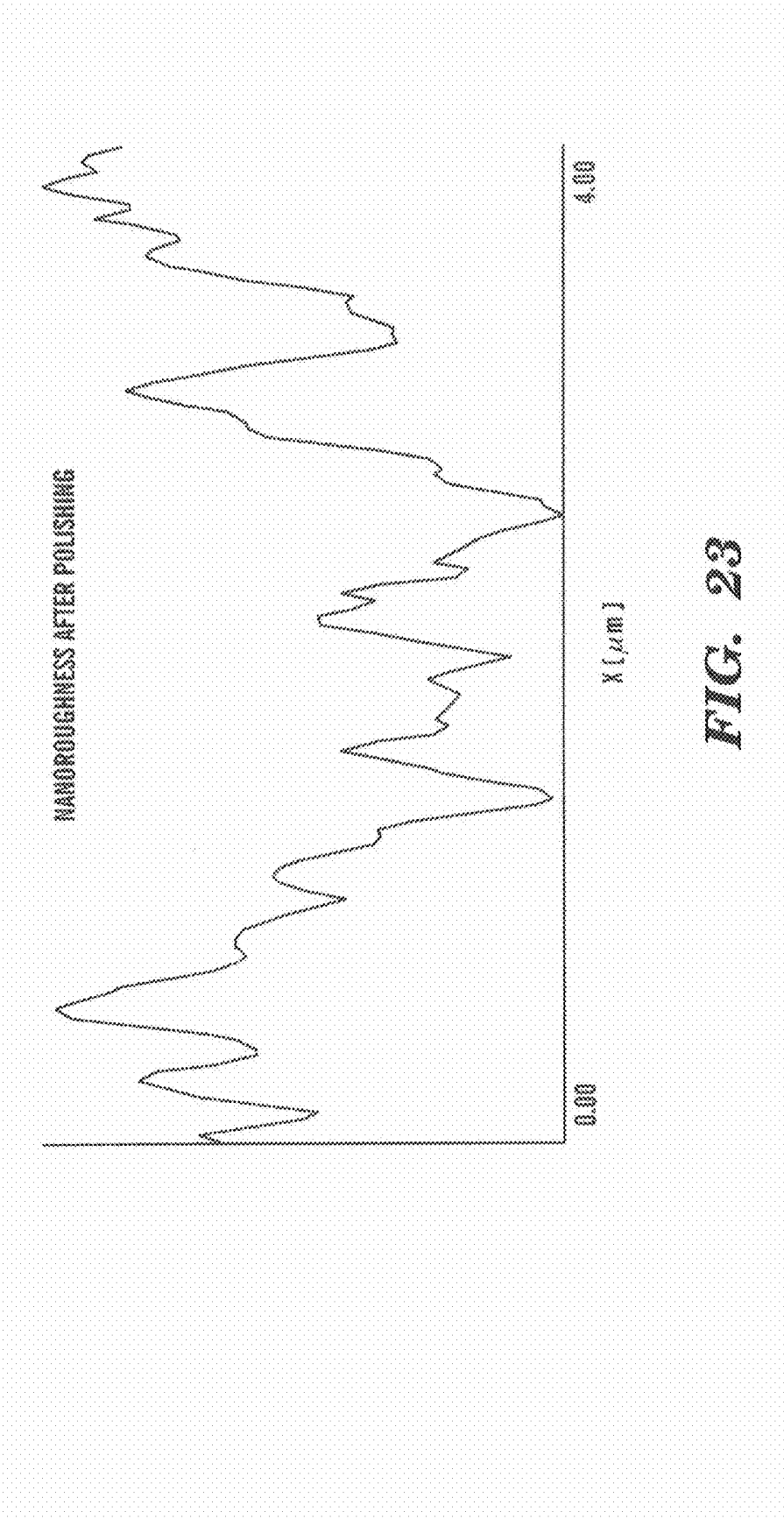


FIG. 23

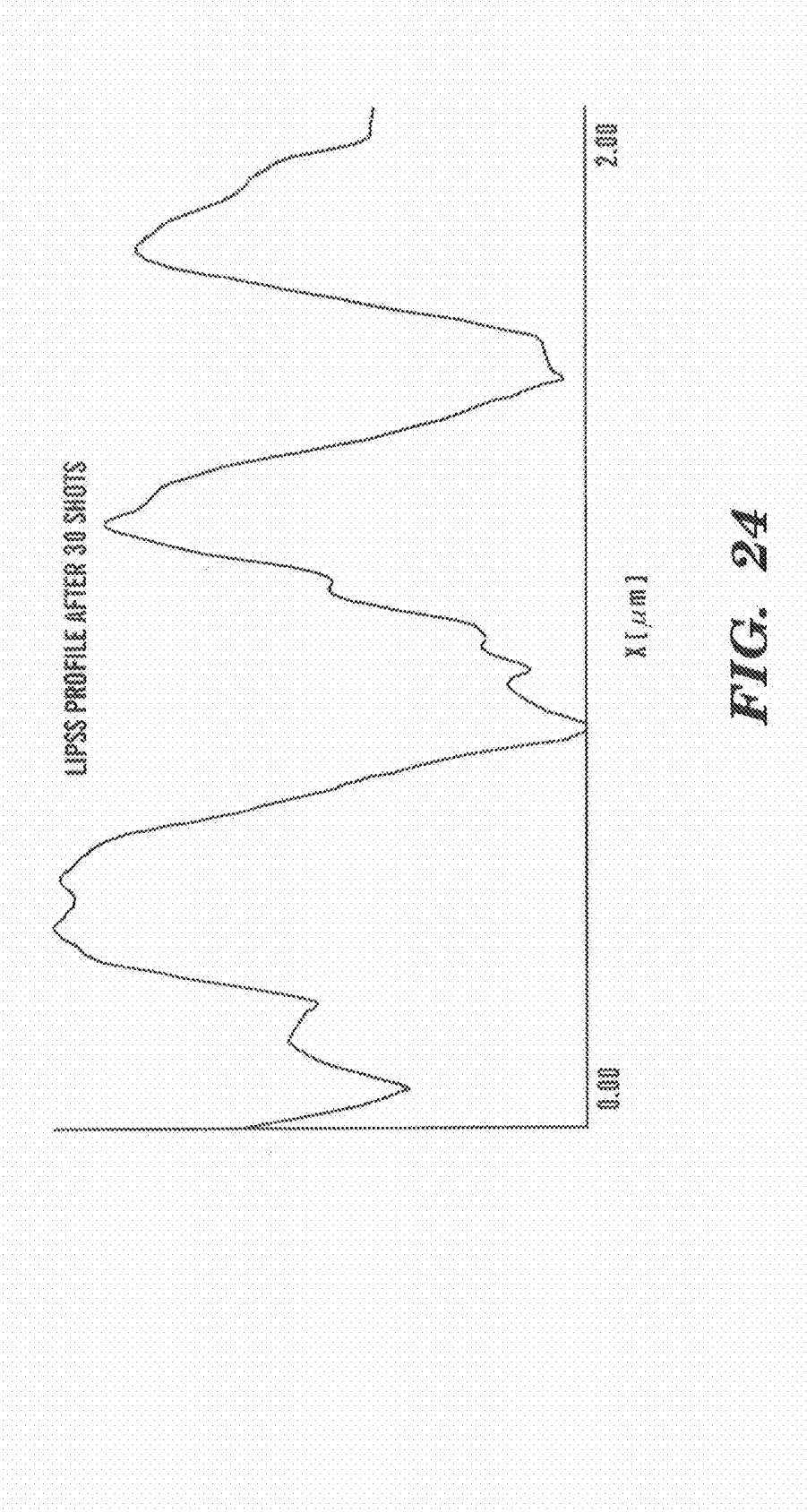


FIG. 24

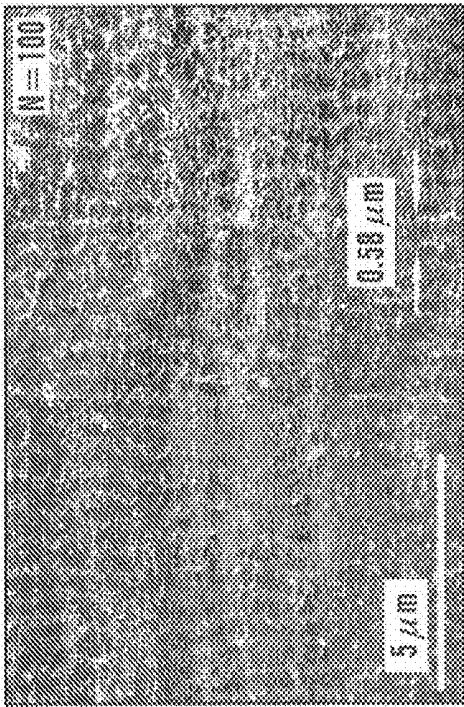


FIG. 25

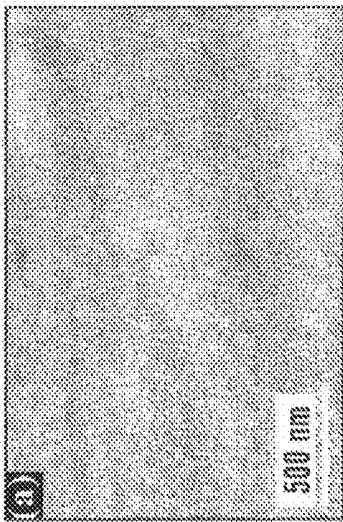


FIG. 26A

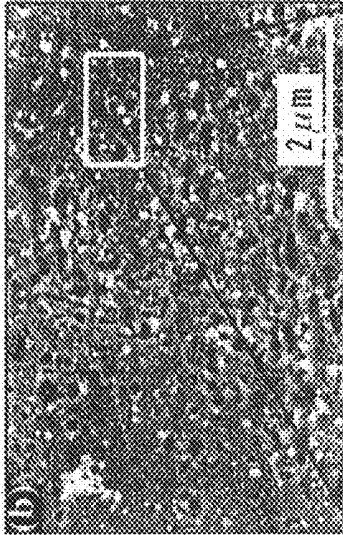


FIG. 26B

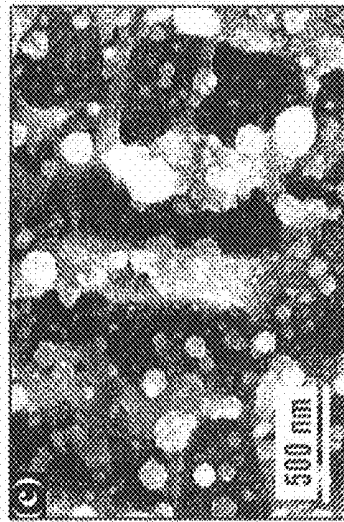


FIG. 26C

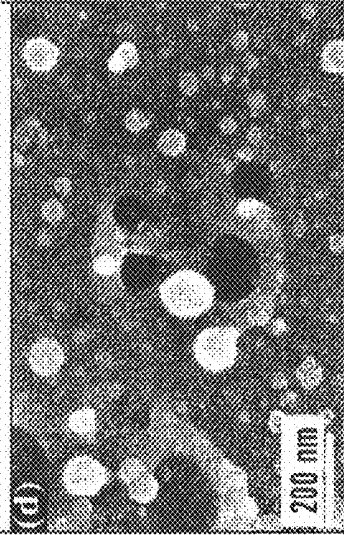


FIG. 26D

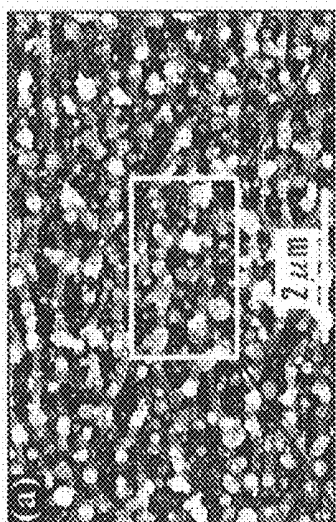


FIG. 27A

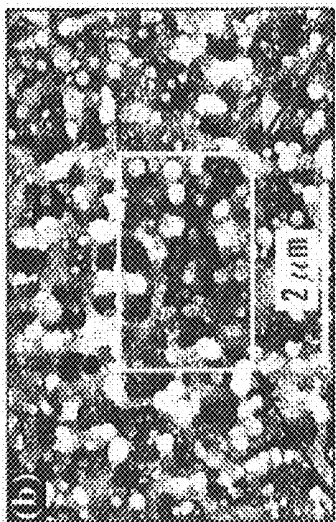


FIG. 27B

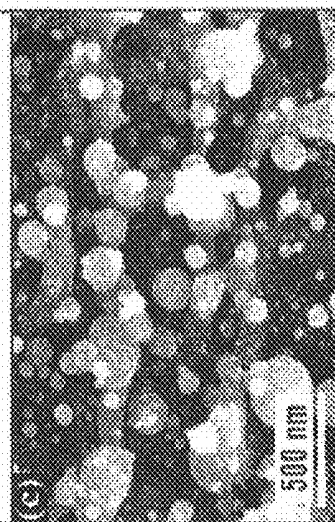


FIG. 27C

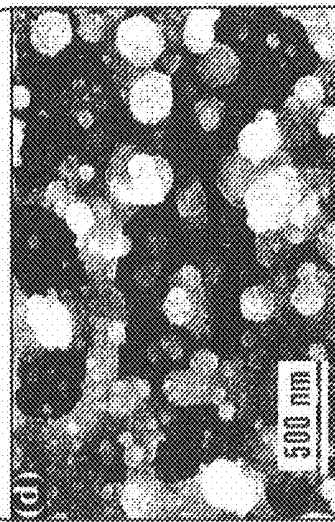


FIG. 27D

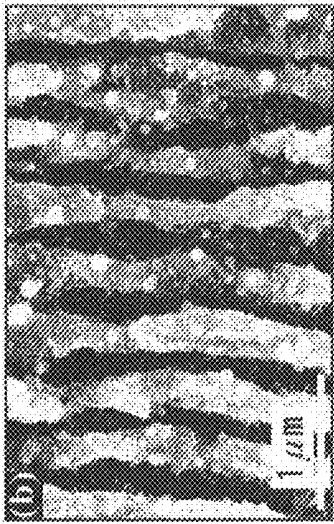


FIG. 28B

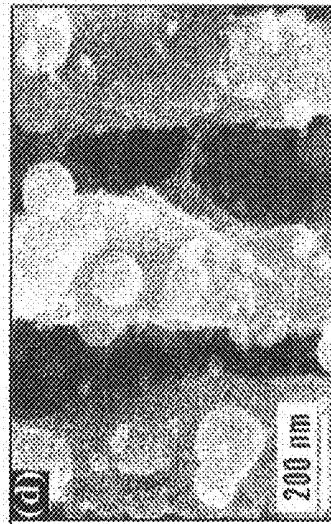


FIG. 28D

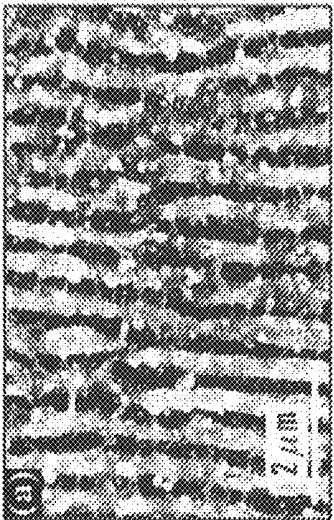


FIG. 28A

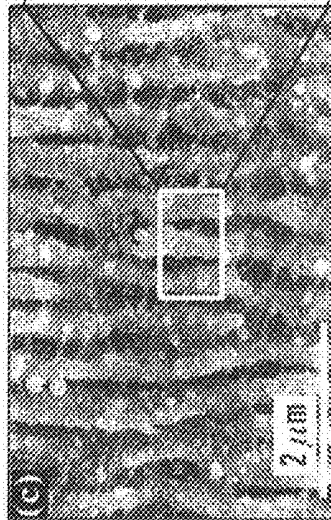


FIG. 28C

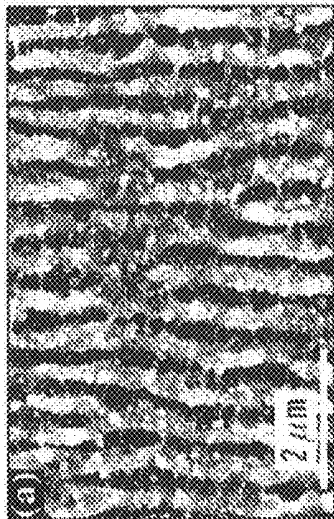


FIG. 29A

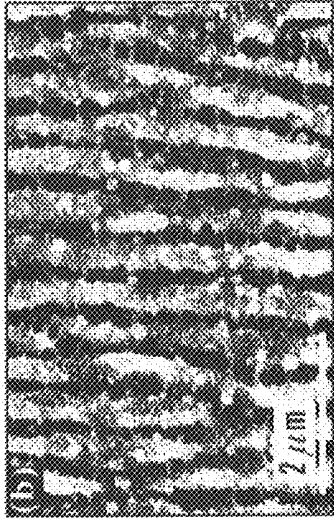


FIG. 29B

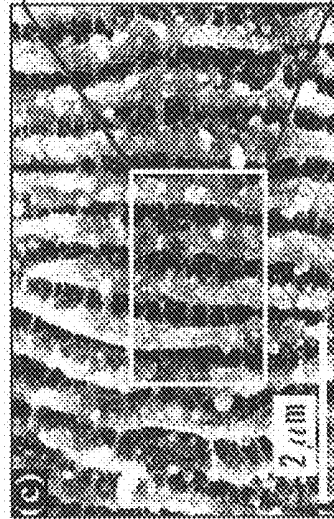


FIG. 29C



FIG. 29D

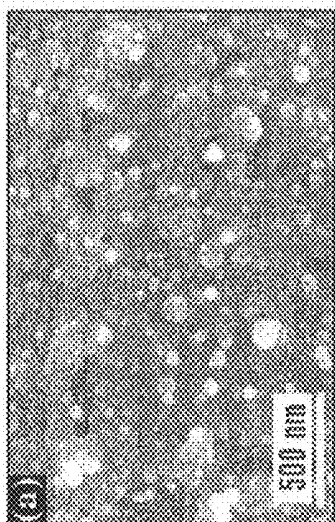


FIG. 30A

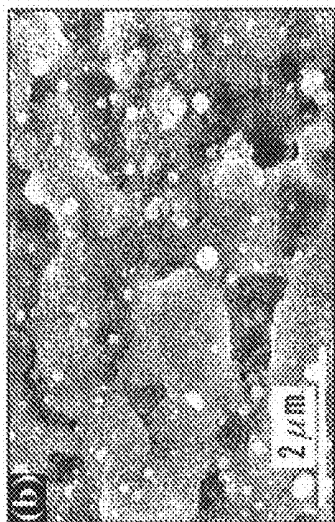


FIG. 30B

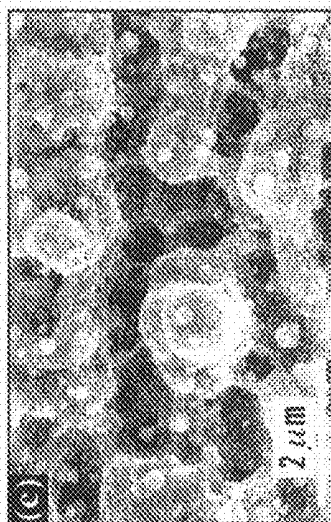


FIG. 30C



FIG. 30D

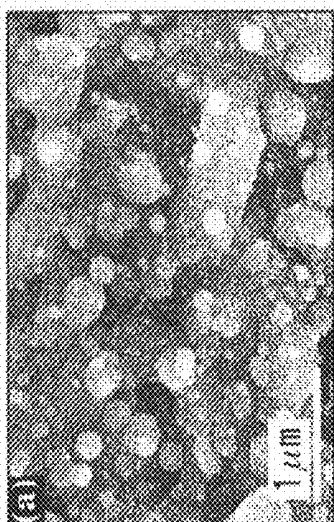


FIG. 31A

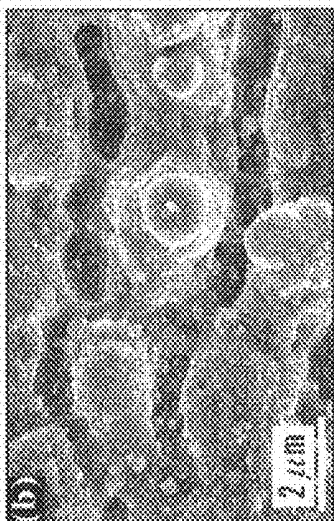


FIG. 31B

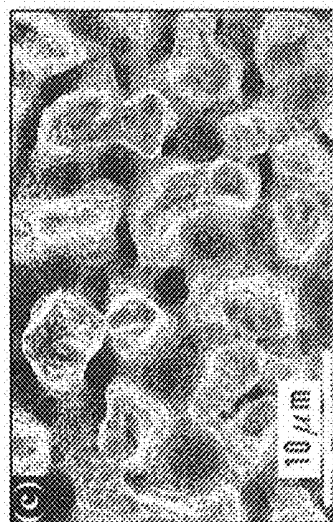


FIG. 31C

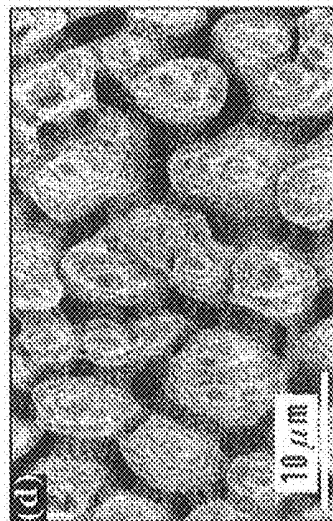


FIG. 31D

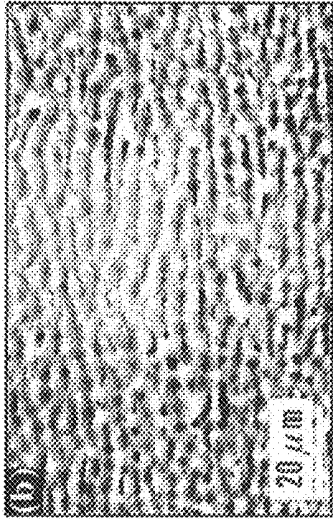


FIG. 32B

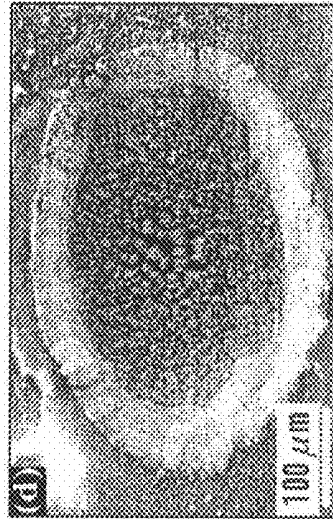


FIG. 32D

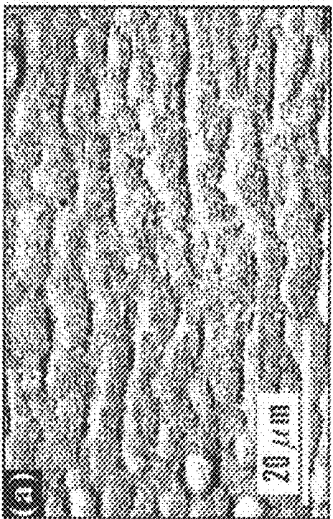


FIG. 32A

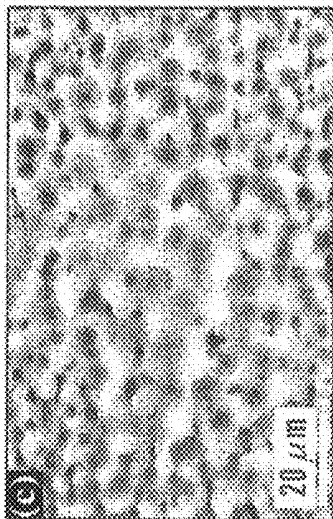


FIG. 32C

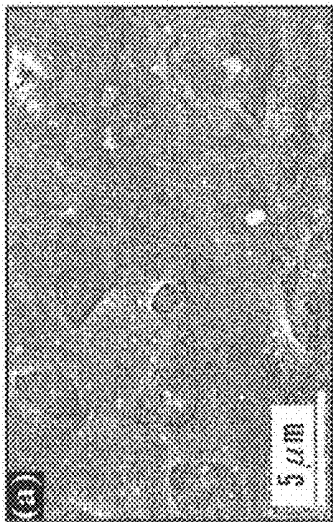


FIG. 33A

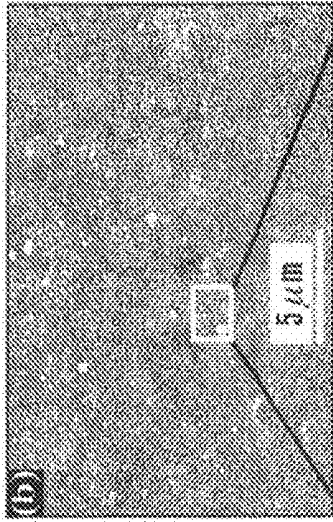


FIG. 33B

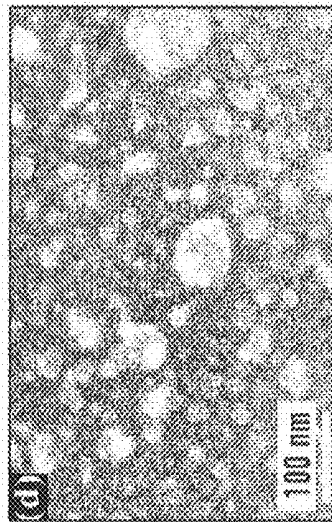


FIG. 33D



FIG. 33C

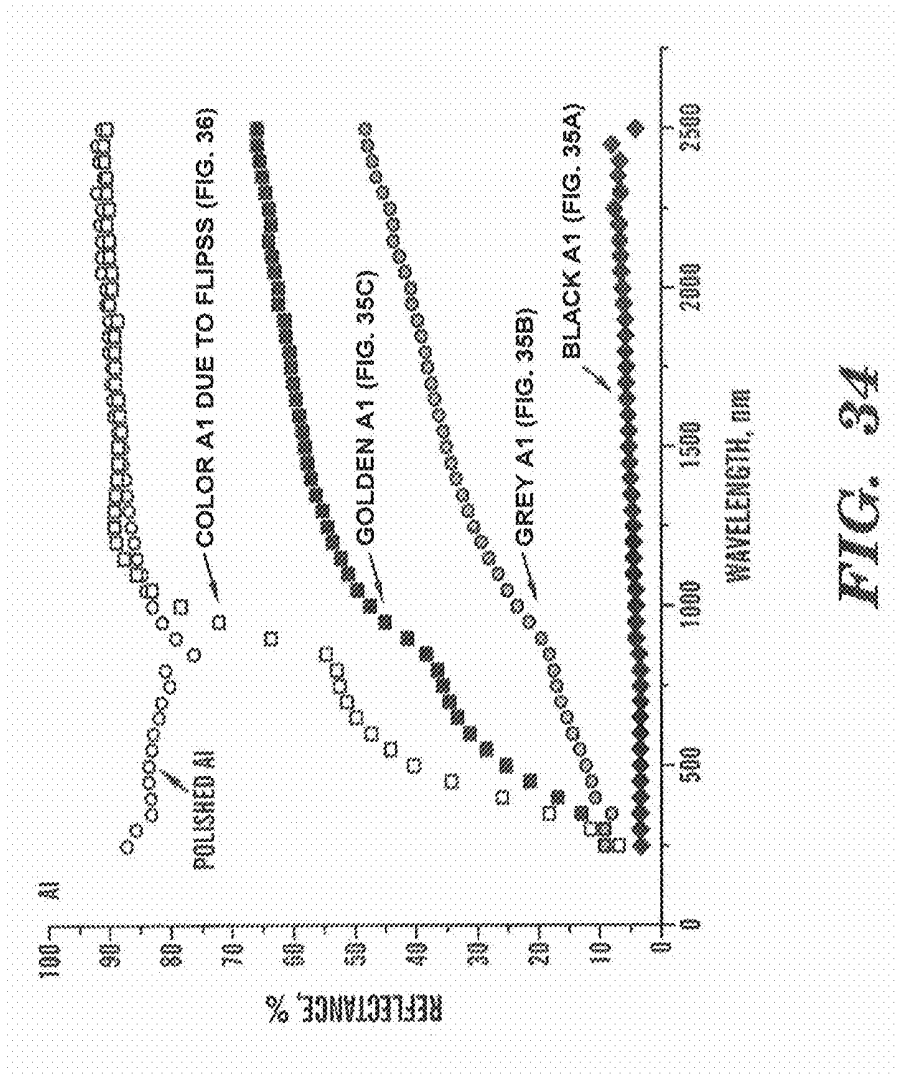


FIG. 34

FIG. 35A

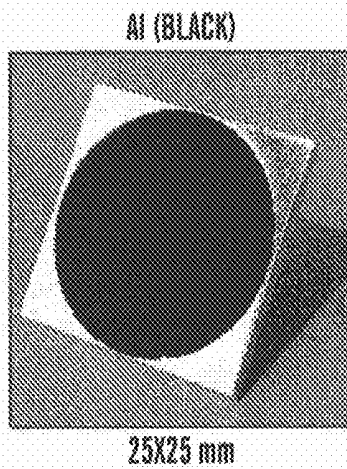


FIG. 35B

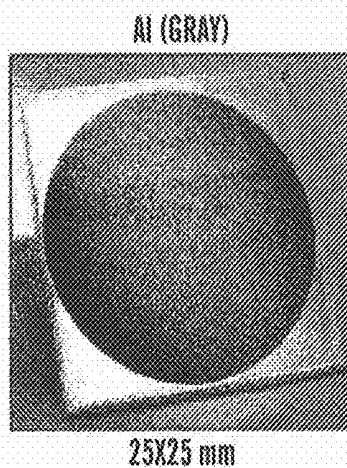


FIG. 35C

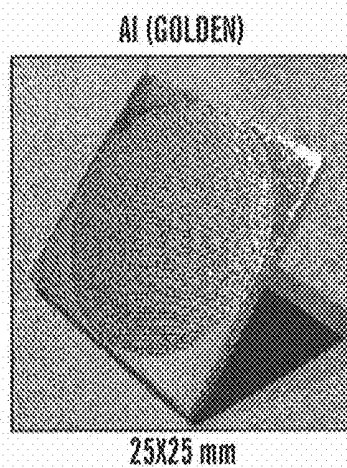
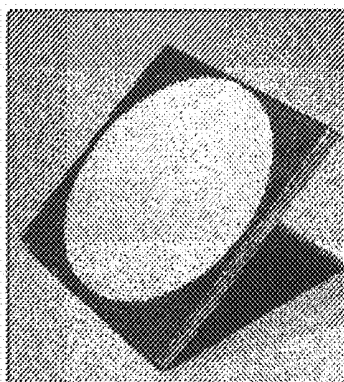


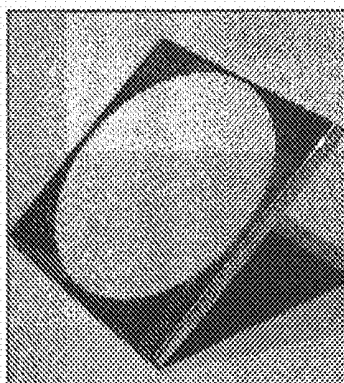
FIG. 36A



Al (FLIPSS)

25X25 mm

FIG. 36B



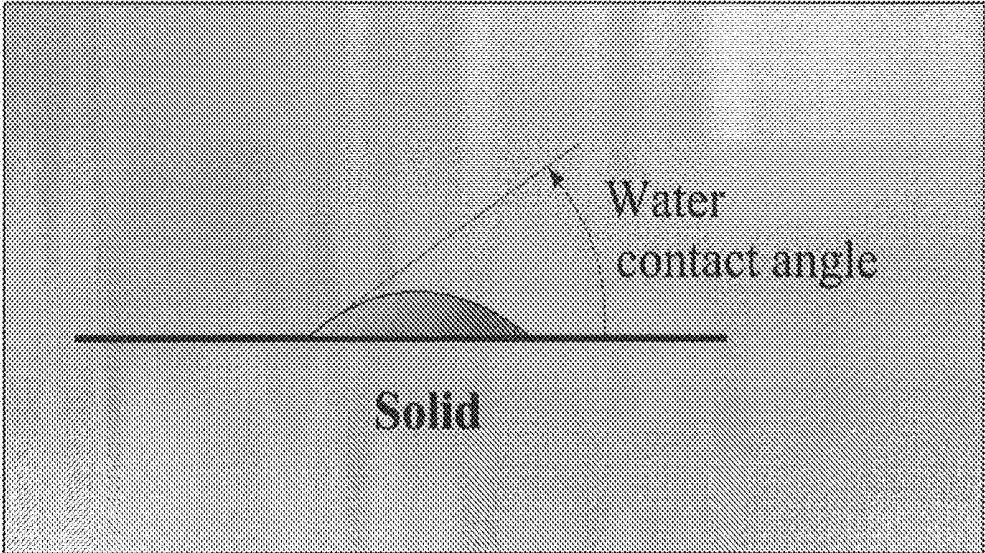


FIG. 37

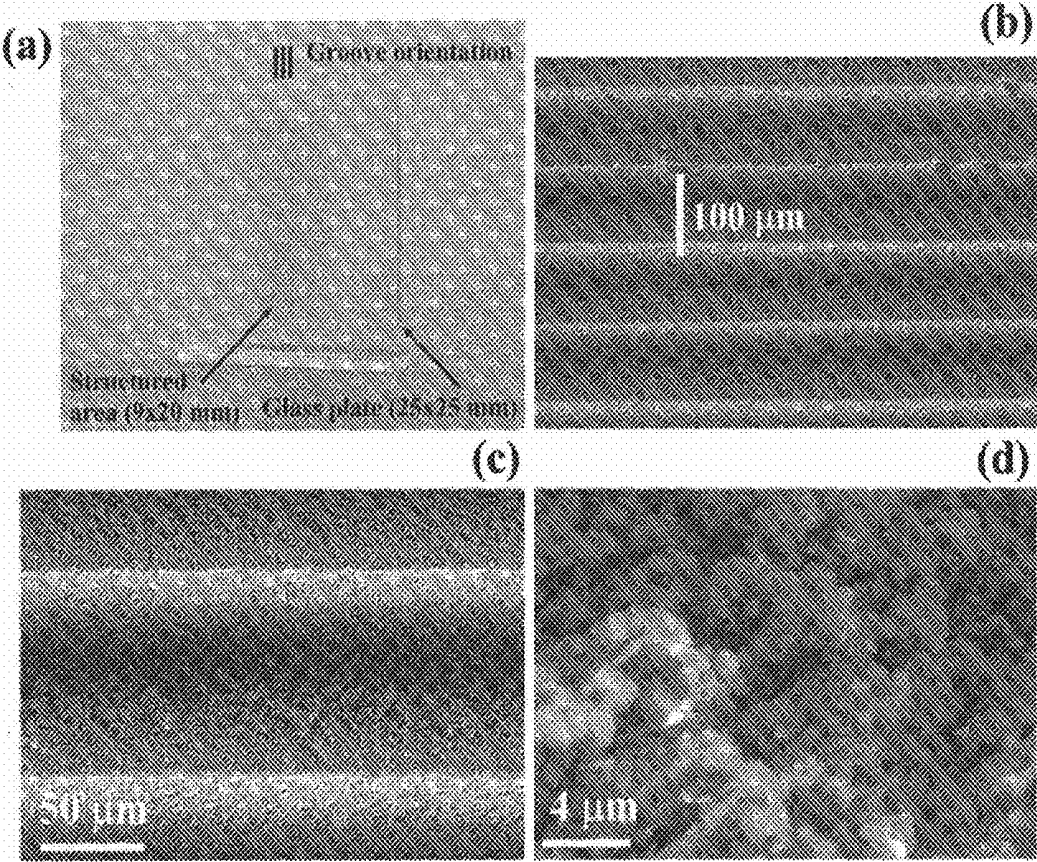


FIG. 38

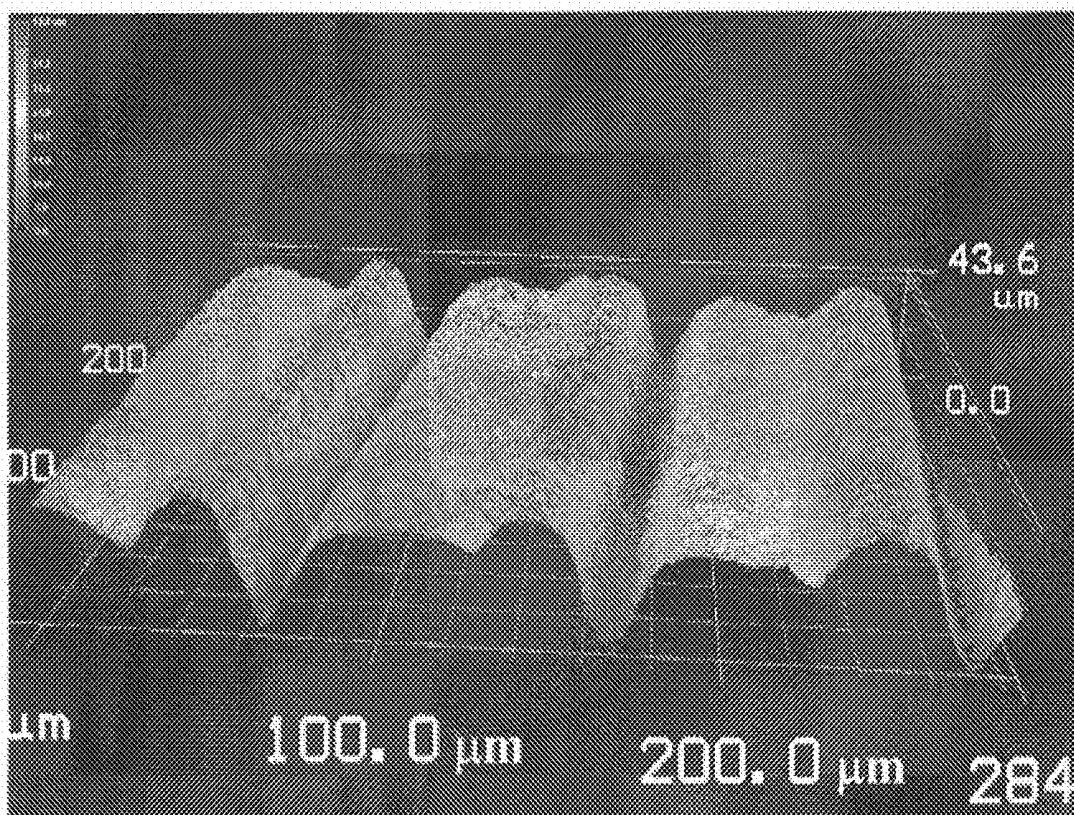


FIG. 39

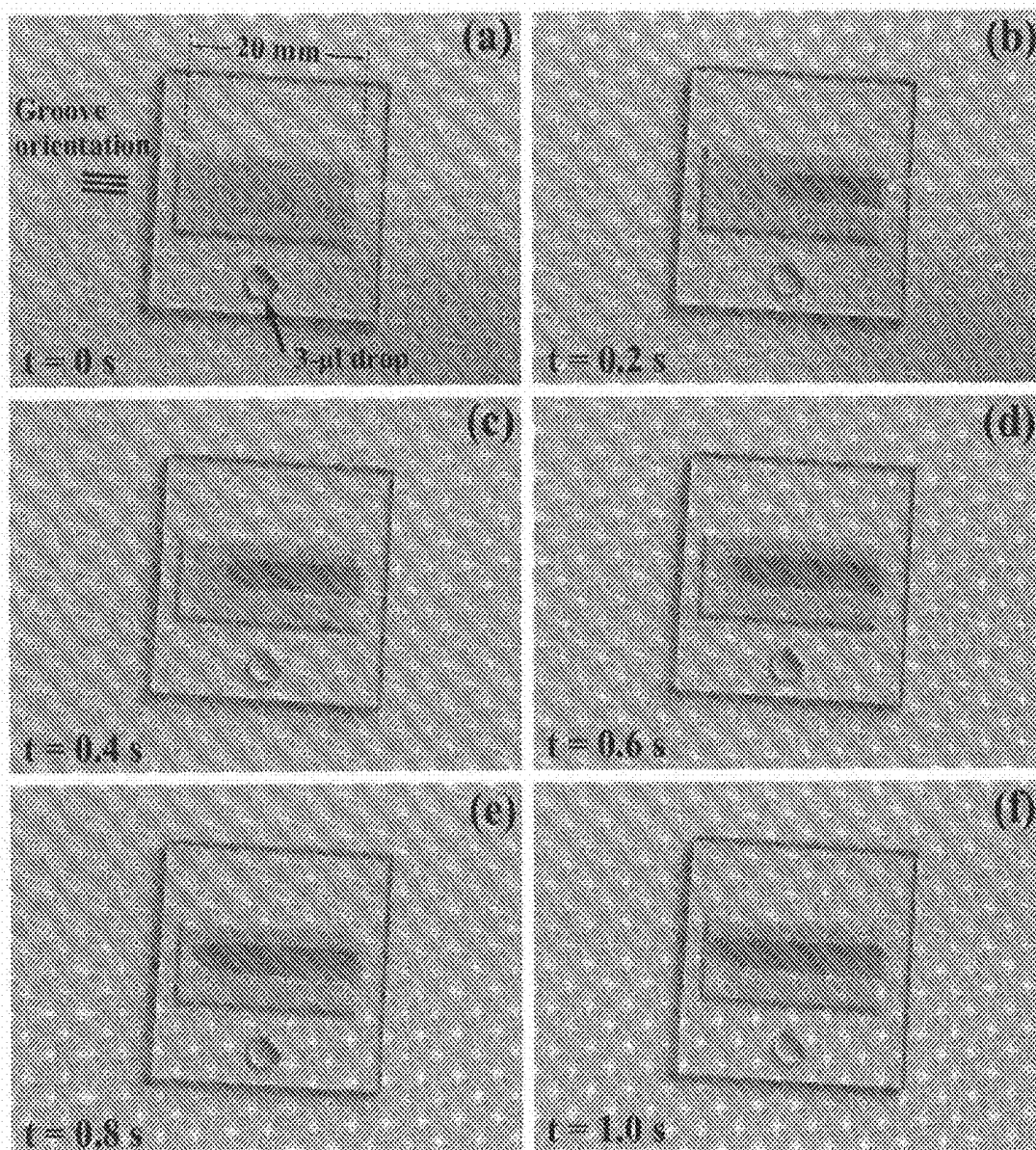


FIG. 40

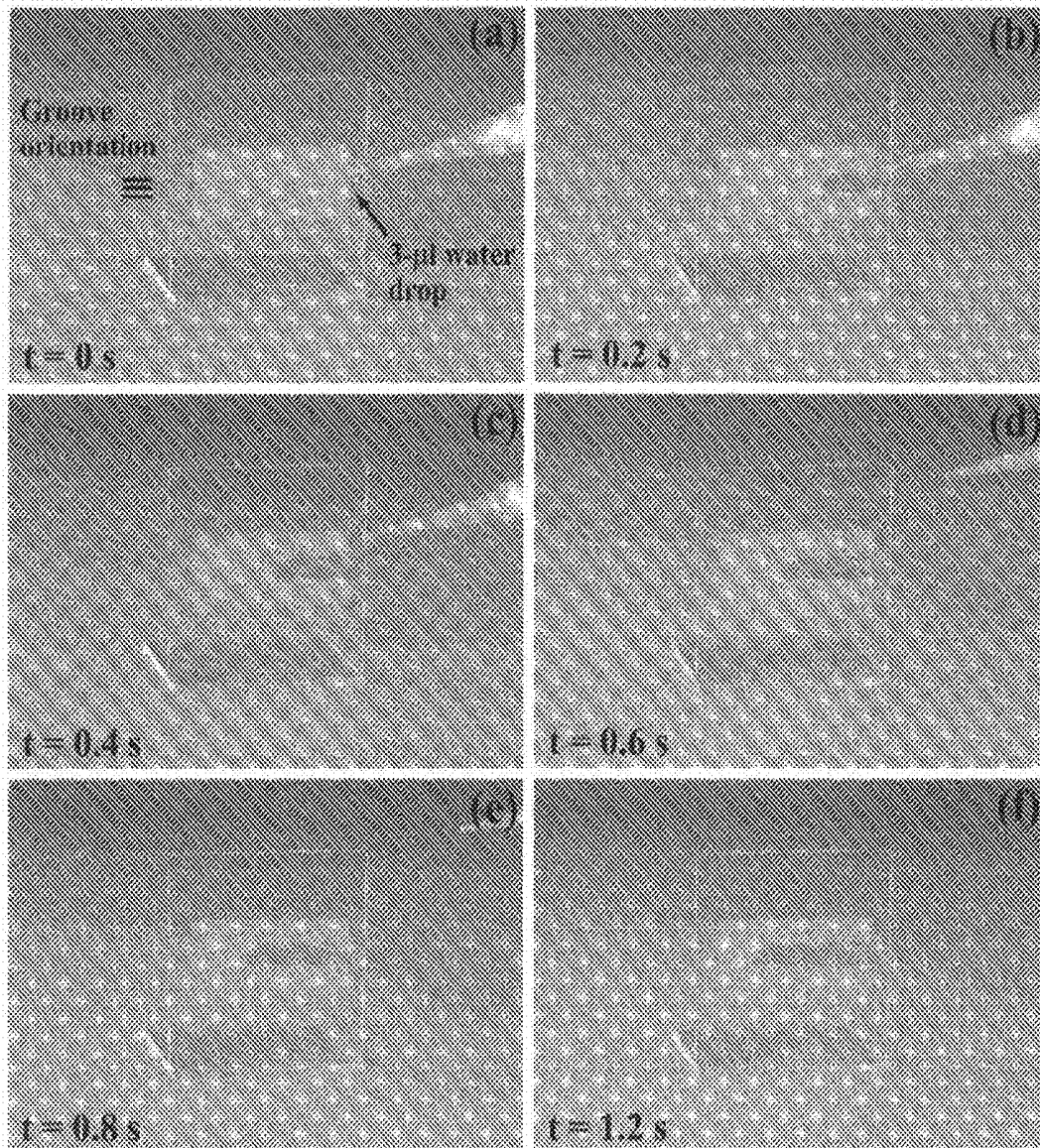


FIG. 41

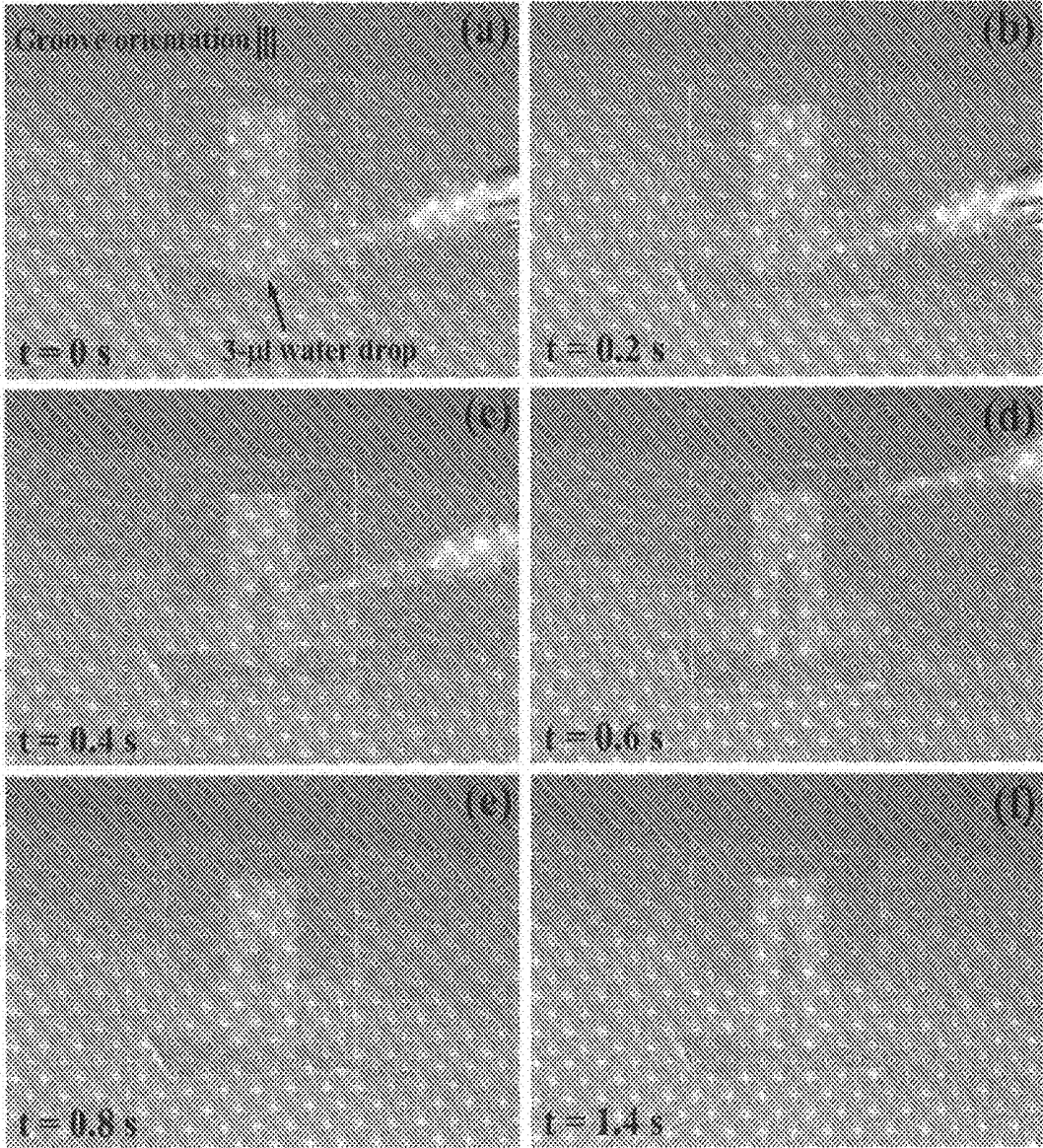


FIG. 42

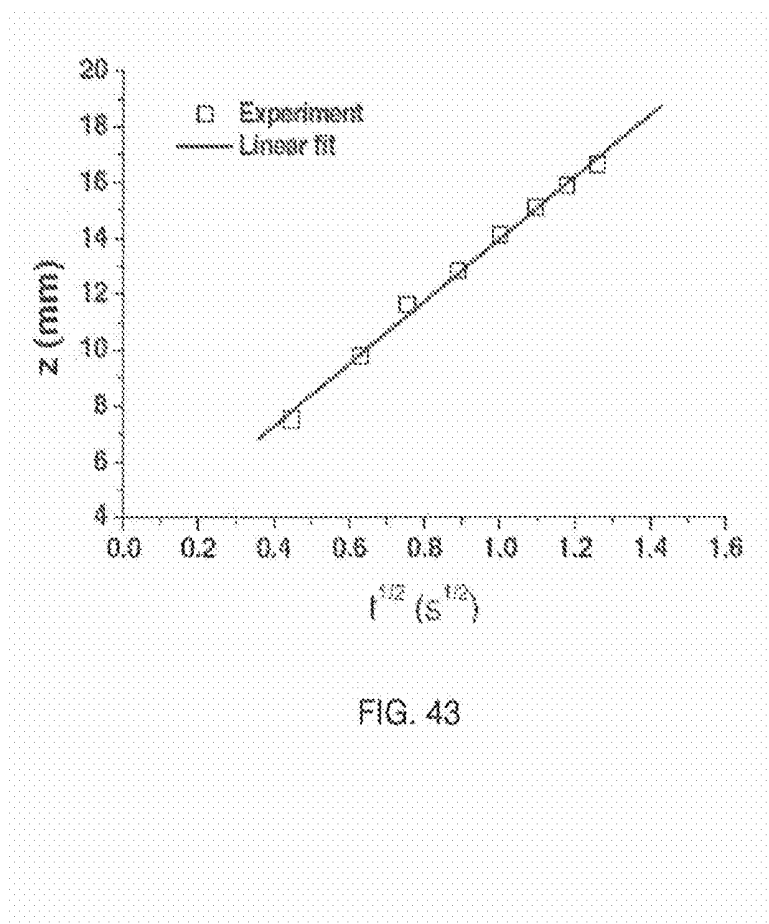


Figure 1. Vorobyev and Guo

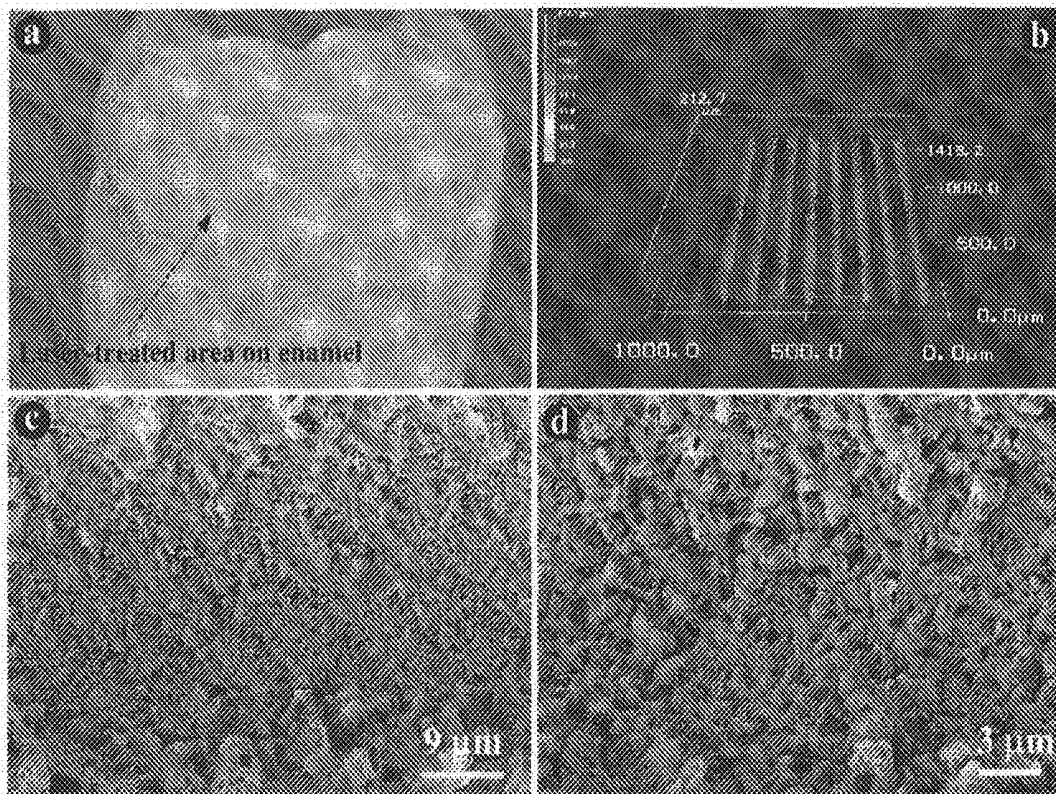


FIG. 44

Figure 2, Vorobyev and Guo

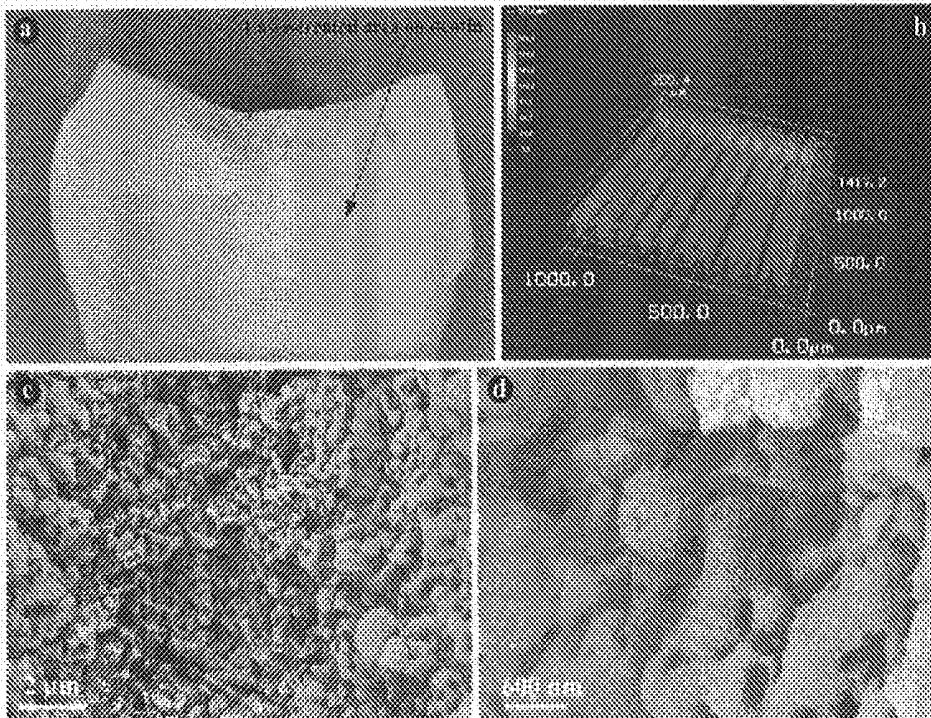


FIG. 45

Figure 3. Vorobyev and Guo

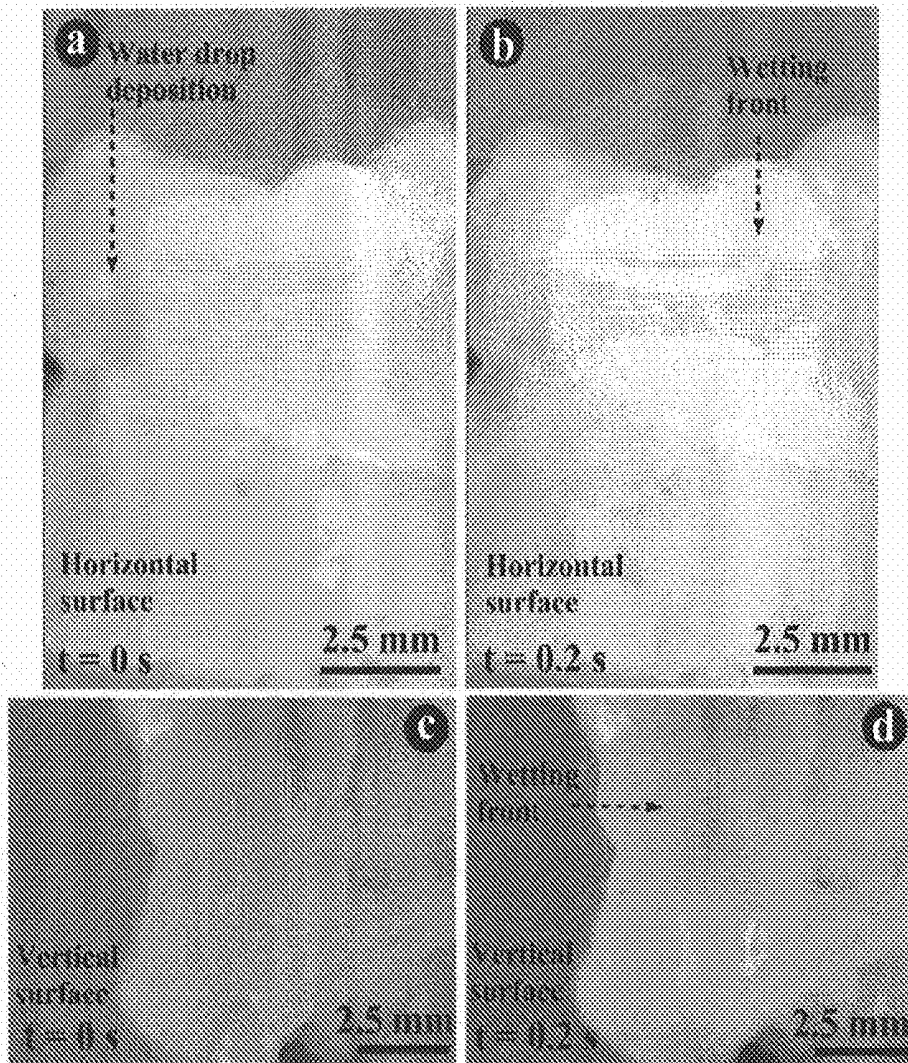


FIG. 46

Figure 4. Vorobyev and Guo

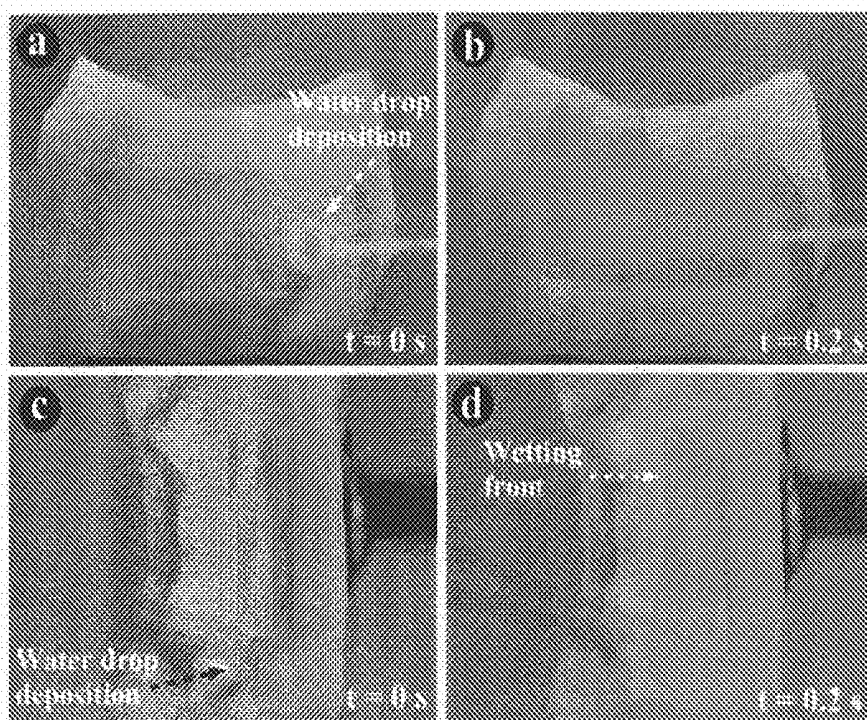


FIG. 47

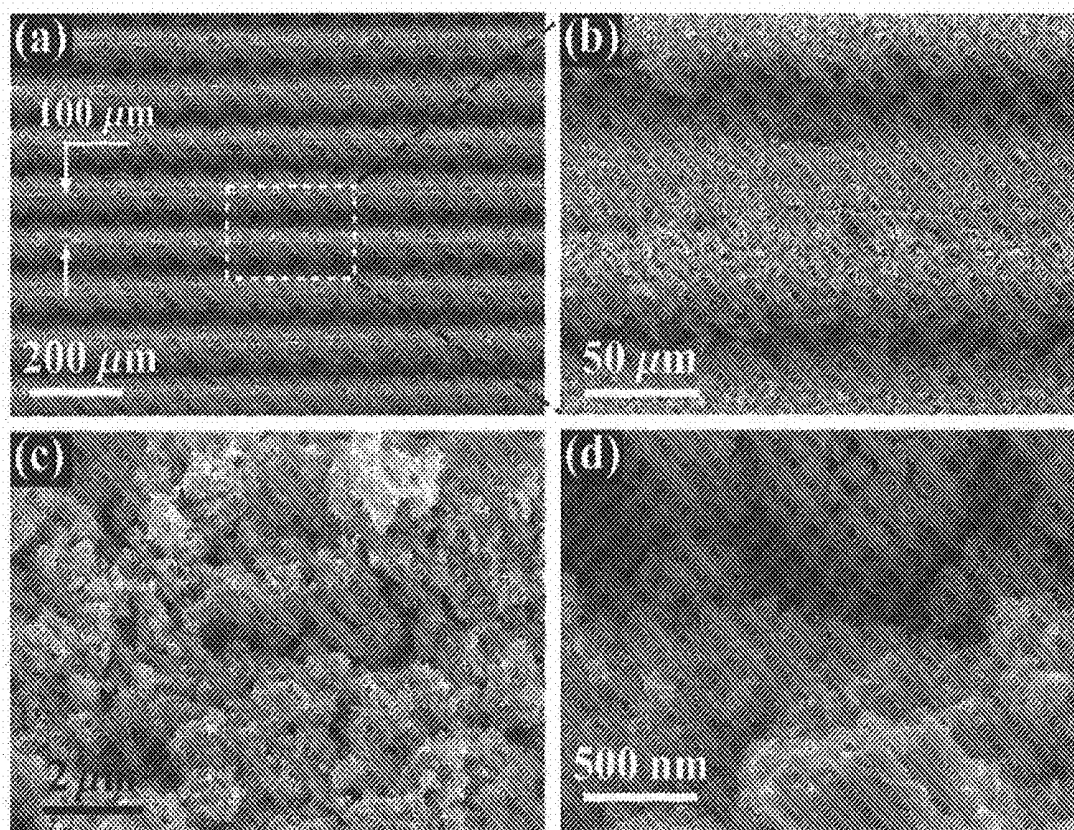


FIG. 48

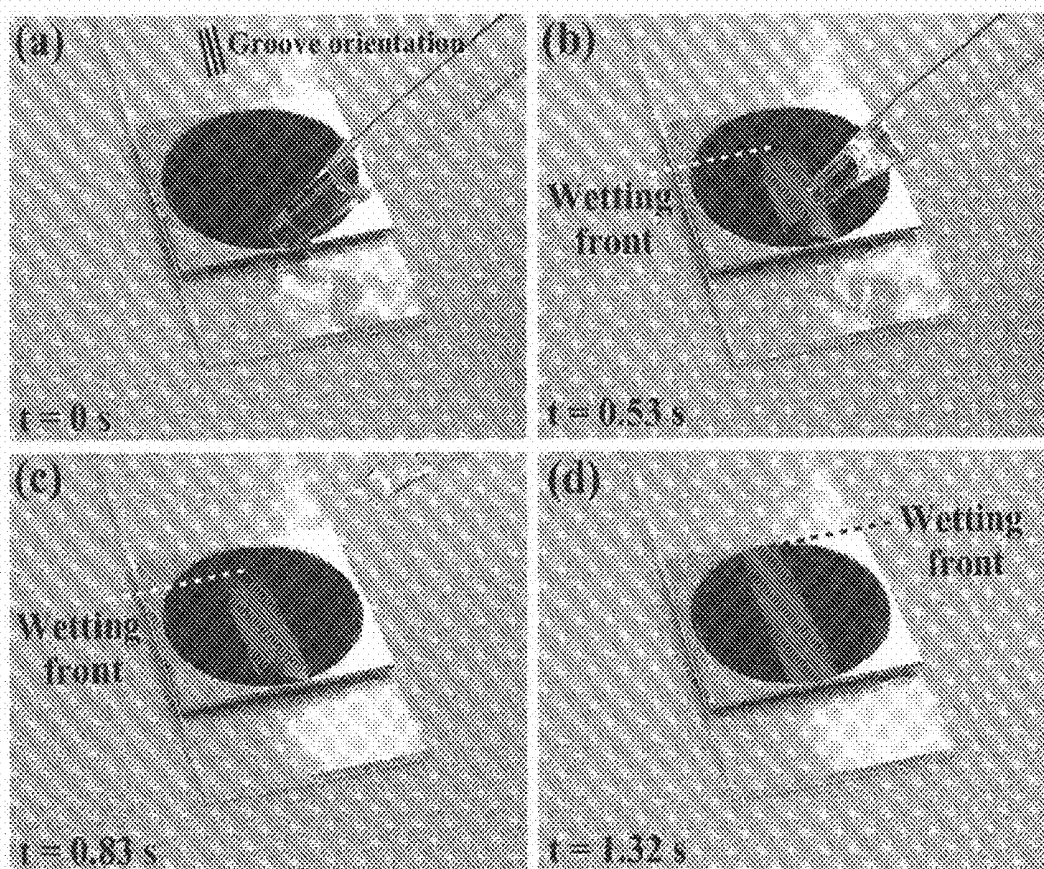


FIG. 49

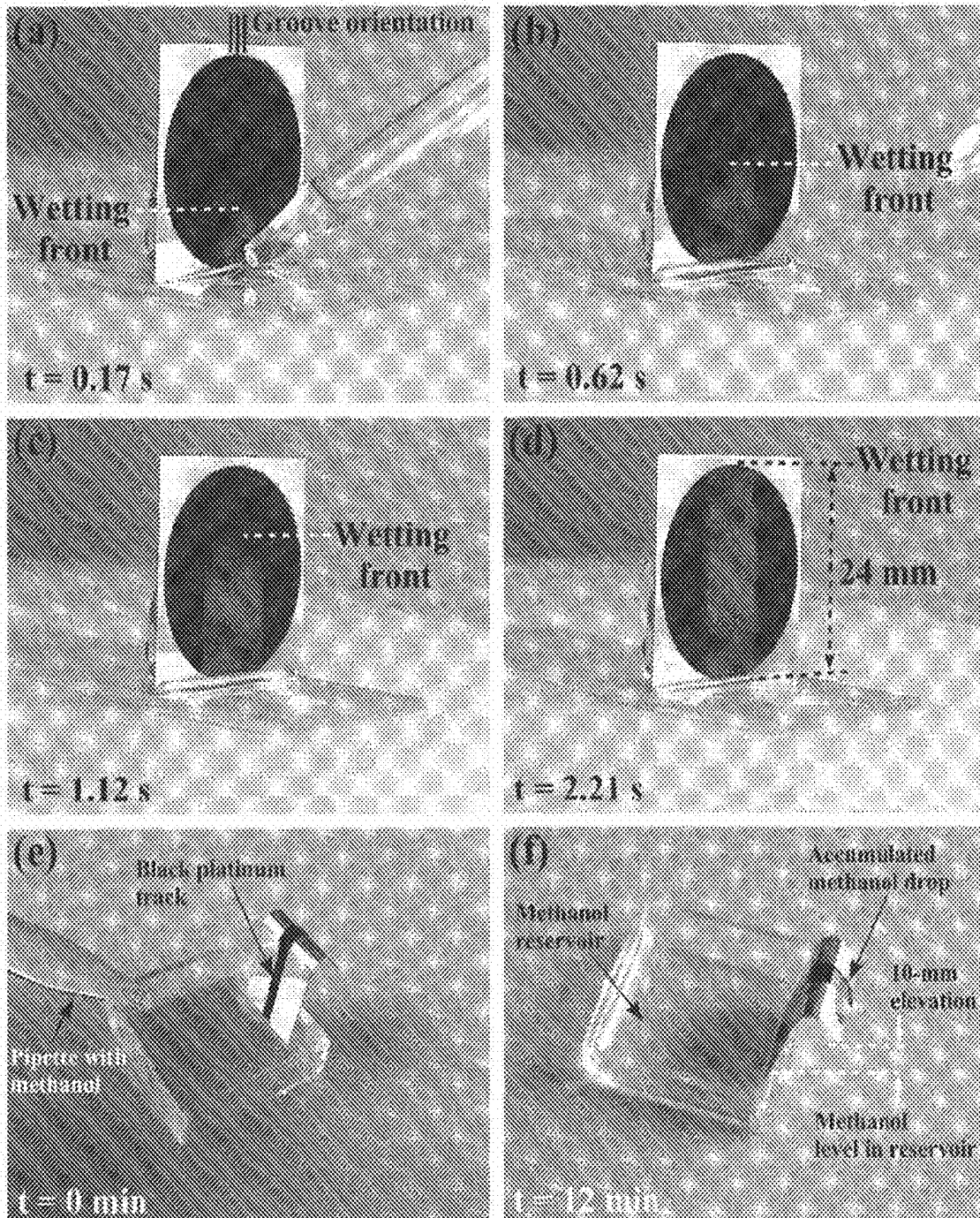


FIG. 50

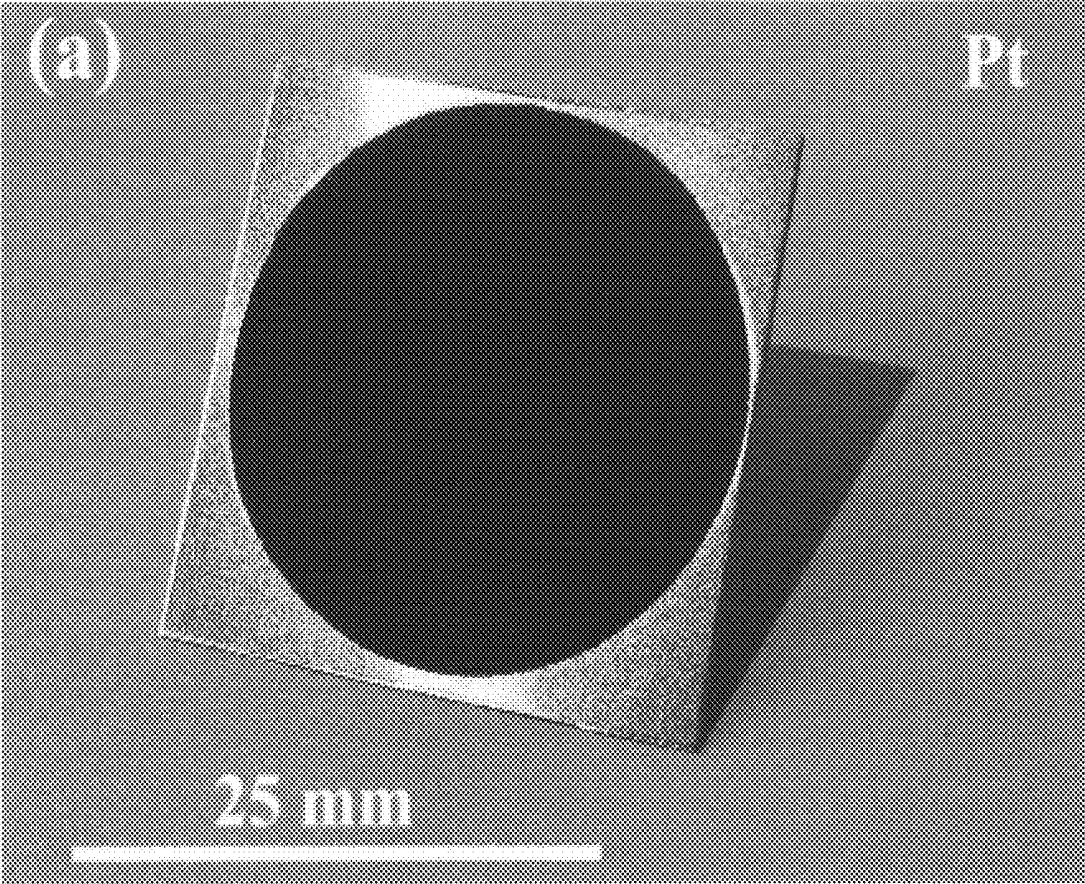


FIG. 51A

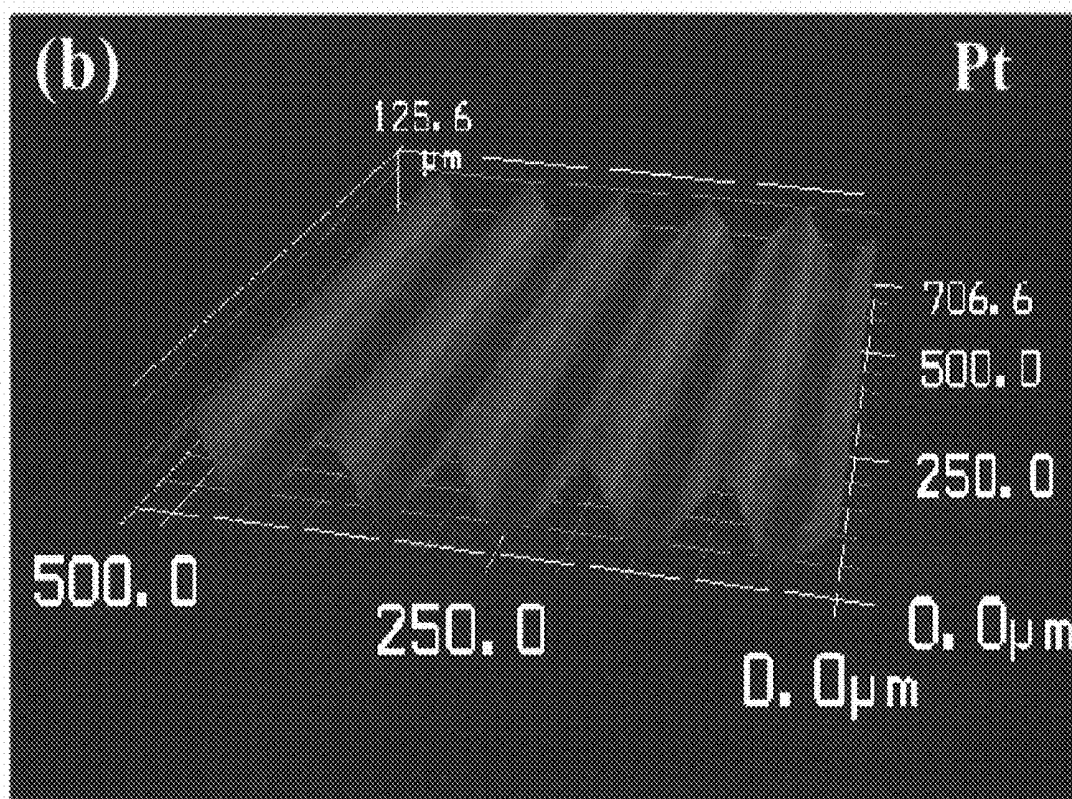


FIG. 51B

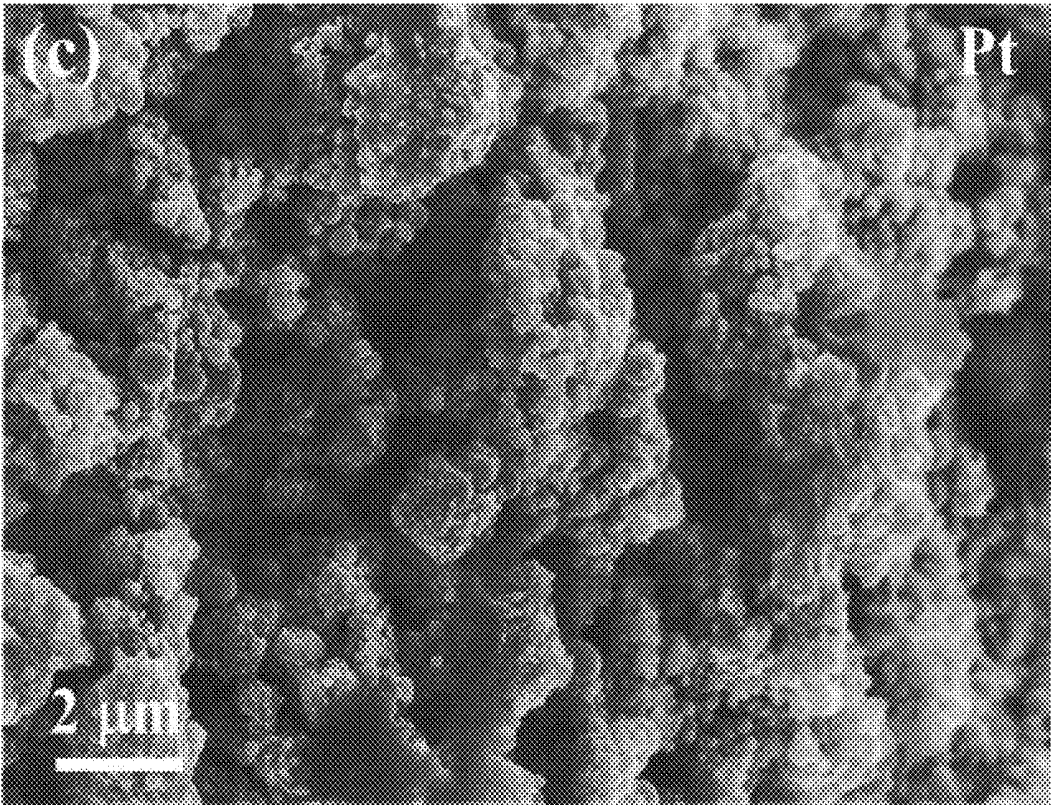


FIG. 51C

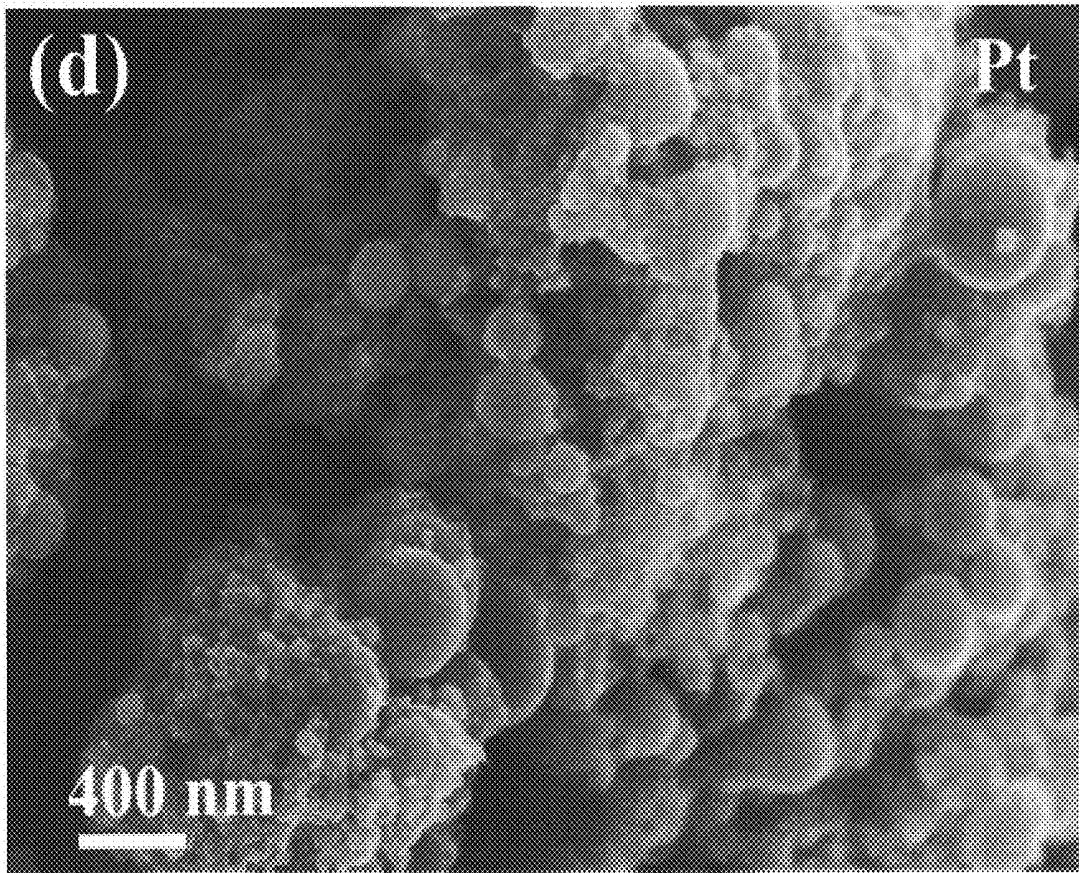


FIG. 51D

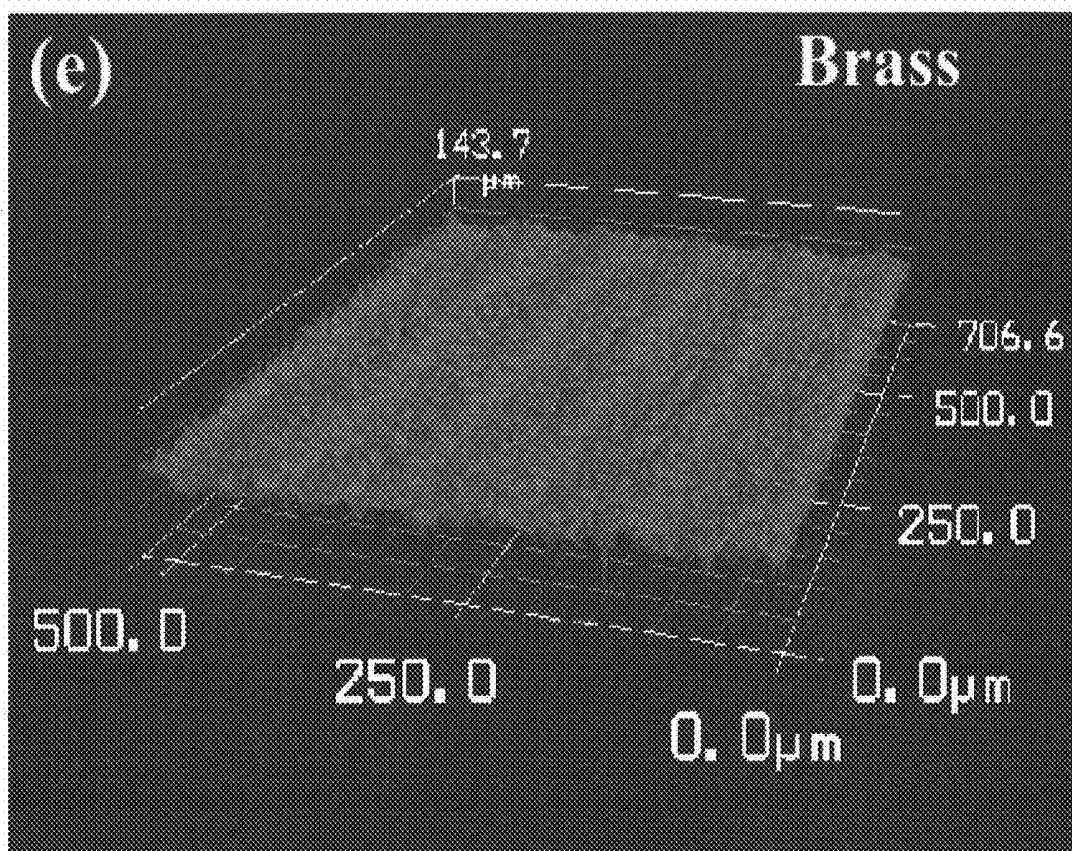


FIG. 51E

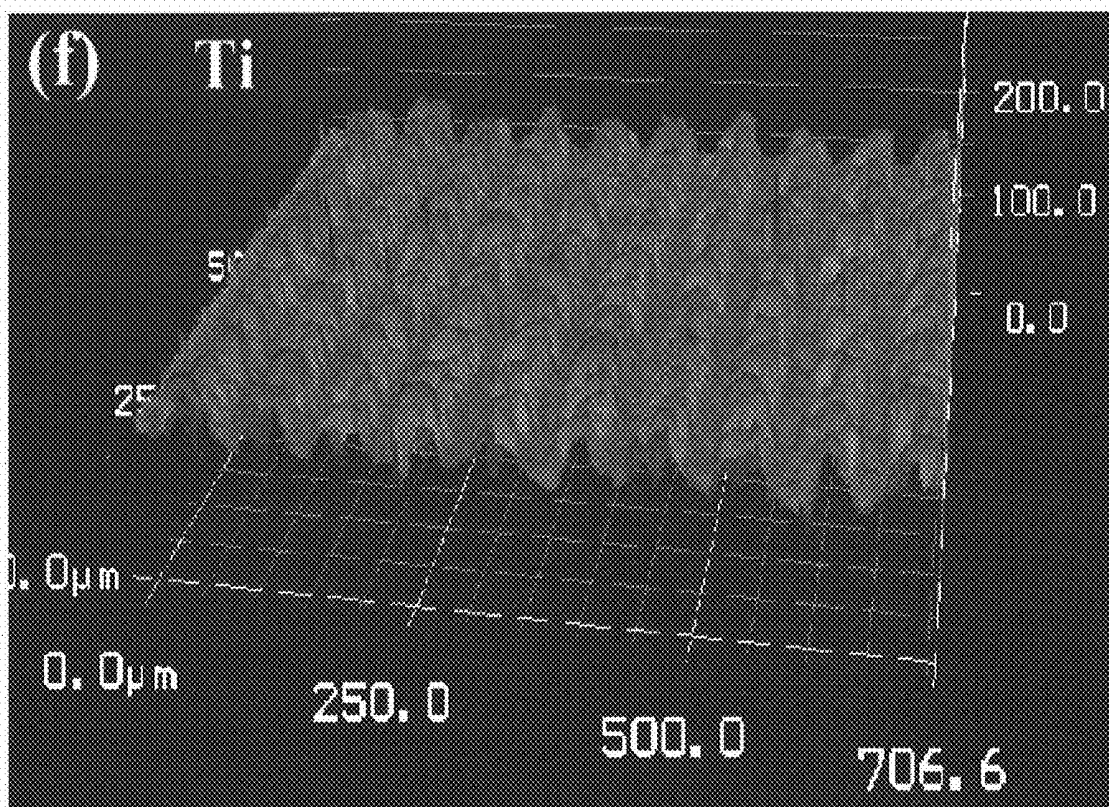


FIG. 51F

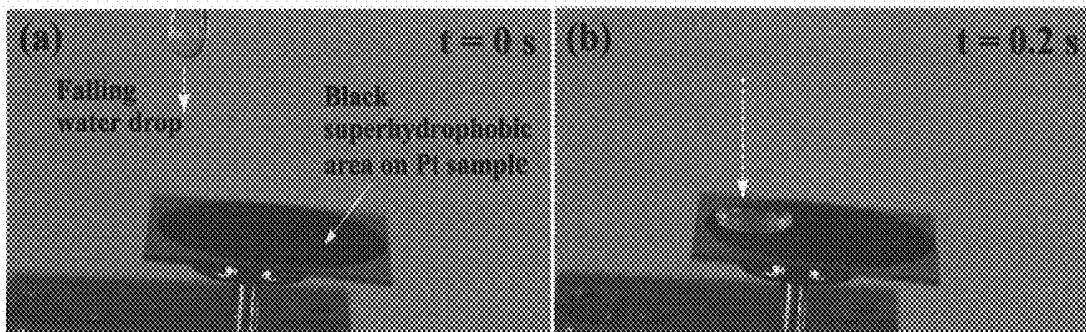


FIG. 52A

FIG. 52B

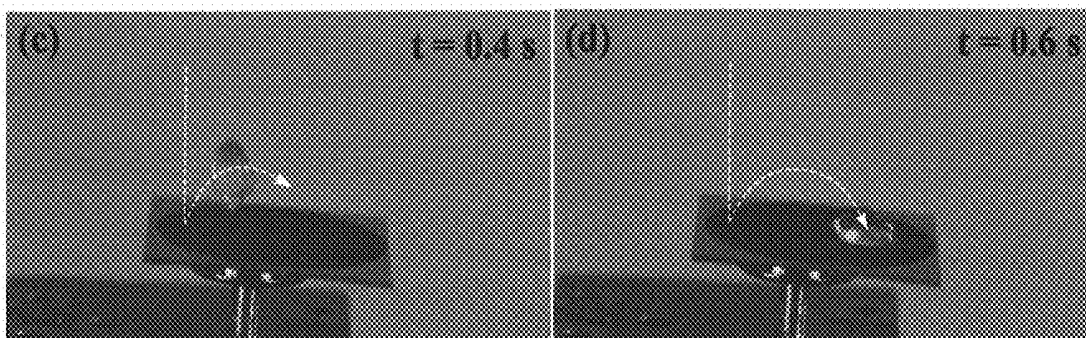


FIG. 52C

FIG. 52D

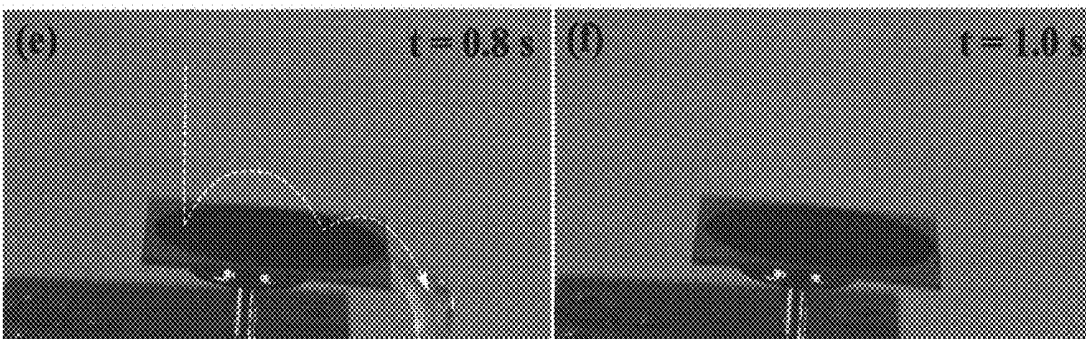


FIG. 52E

FIG. 52F

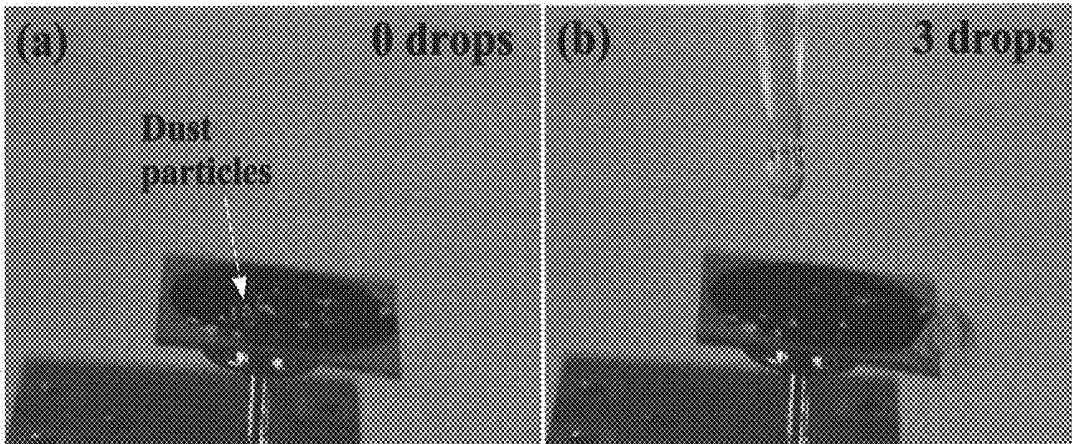


FIG. 53A

FIG. 53B

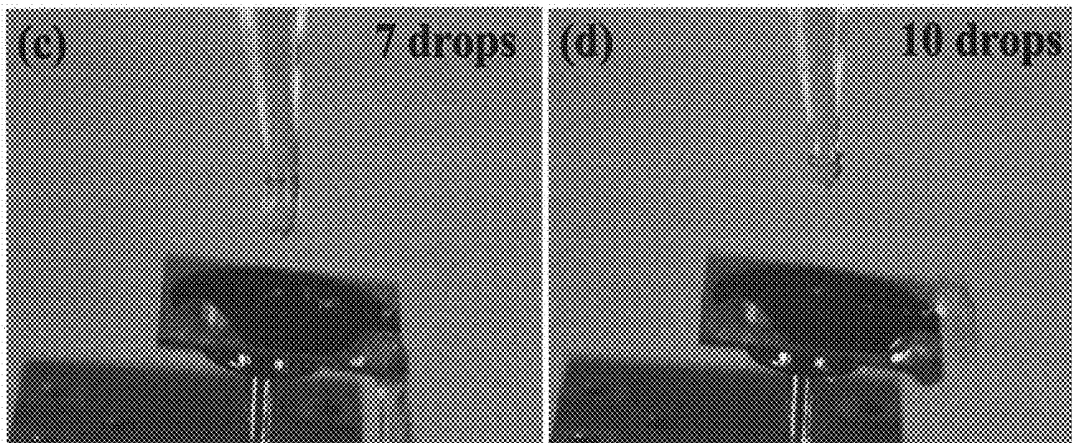


FIG. 53C

FIG. 53D

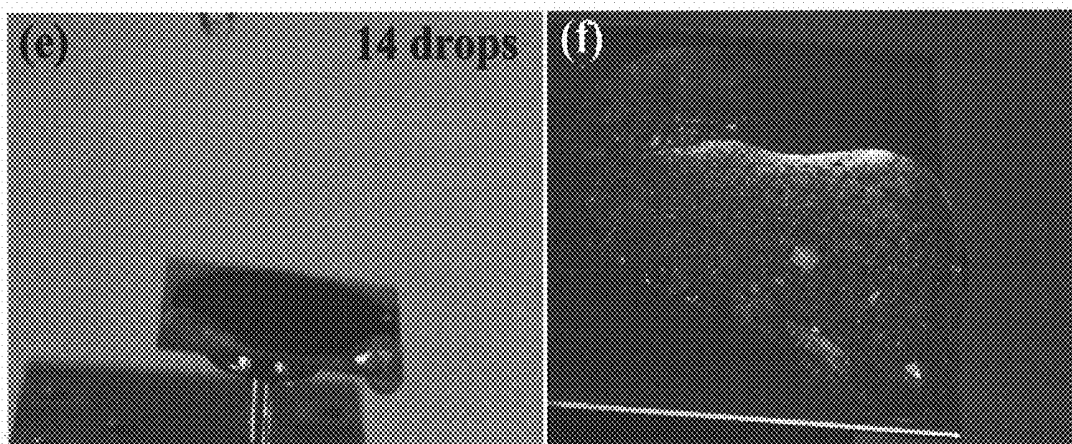


FIG. 53E

FIG. 53F

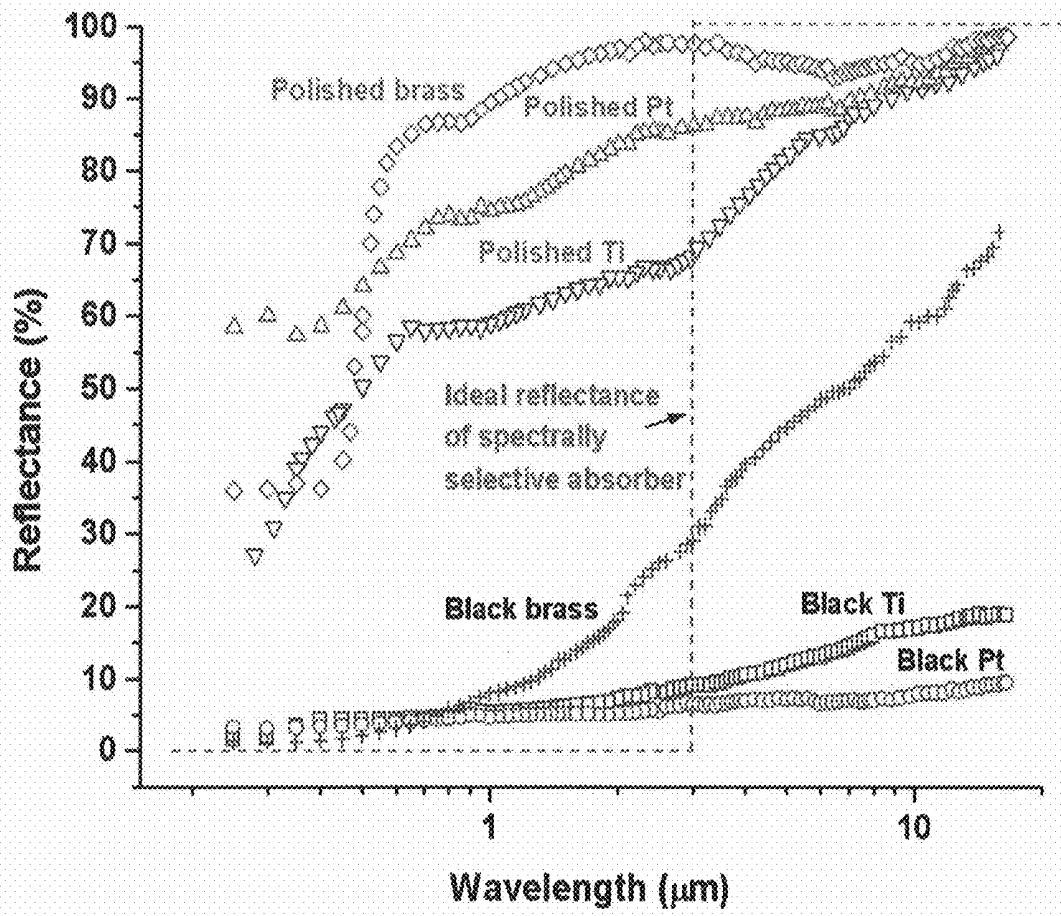


FIG. 54

SUPER-HYDROPHOBIC SURFACES AND METHODS FOR PRODUCING SUPER-HYDROPHOBIC SURFACES

RELATED APPLICATION DATA

[0001] This patent application is a continuation of, and claims priority to U.S. application Ser. No. 14/593,465 filed on Jan. 9, 2015, which itself is a continuation-in-part of, and claims priority to, U.S. application Ser. No. 13/604,951 filed on Sep. 6, 2012, which itself is a continuation-in-part of, and claims priority to, U.S. application Ser. No. 12/188,258 filed on Aug. 8, 2008, which itself is a continuation-in-part of, and claims priority to U.S. application Ser. No. 11/862,449 filed on Sep. 27, 2007, which further claim priority to U.S. Provisional Application Ser. No. 60/847,916 filed Sep. 29, 2006, the subject matters of which are herein incorporated by reference in their entireties.

FEDERALLY SPONSORED RESEARCH

[0002] This invention was made with government support under grant number CTS042506 awarded by the National Science Foundation. The government has certain rights in the invention.

BACKGROUND

1. Field of the Invention

[0003] Embodiments of the invention generally pertain to the field of materials processing and associates processed materials. More particularly, embodiments of the invention are directed to methods for processing materials using femtosecond duration laser pulses, applications of such methods, and materials and/or material properties resulting from such methods. Even more particularly, embodiments of the invention are directed to methods for altering the surface structure of metal materials using femtosecond duration laser pulses, applications of such methods, and materials and/or material properties resulting from such methods, including blackened and colored metals.

2. Description of Related Art

[0004] Although materials may be shaped or otherwise altered in a large variety of ways including milling, machining, grinding, etc., in recent years, laser-based alteration of materials has become a common method for a variety of materials processing applications. For example, laser alteration of materials by high energy laser pulses has been used to both create precise hole patterns in metals or metal films as well as for more subtle material alterations such as texturing of metals or metal films by the intense heating/melting/vaporization effects of such high energy laser beams.

[0005] Reported methods of laser alteration of materials involves the use of 'short-duration' (i.e., nanosecond (ns) and picosecond (ps)) laser pulses. See, for example, U.S. Pat. Nos. 5,635,089 and 4,972,061. U.S. Pat. No. 6,979,798 describes the use of laser pulses of preferably less than 130 femtoseconds (fs) to specifically burn metal links on integrated circuits. Thus the use of ultra-short (ns) duration laser pulses for laser processing of materials may achieve results that are different than those from longer duration (i.e., 'short') laser pulses. The duration of a nanosecond laser pulse is long enough for the pulse to interact with the

material as it is ejected from the surface. Ultra-short duration, femtosecond (fs) laser pulses, by comparison, are not long enough in duration to interact with the material ejected from the surface of the irradiated substance, since the pulse ends long before the hydrodynamic expansion of the ejected material. Another difference between different laser pulse timescales is that the laser-supported combustion and detonation waves that are commonly generated in a nanosecond duration laser pulse do not occur in an ultra-short fs laser pulse, again offering up the possibility of materials processing effects and resulting material parameters that may be difficult or impossible to obtain with longer duration laser irradiation.

[0006] In light of the above observations, advantageous benefits may be obtained from the use of ultra-short, femtosecond pulses in the processing of certain materials and the altered materials or material characteristics resulting from processing with one or more fs laser pulses. Certain advantageous benefits may also be realized by the ability to controllably modify optical properties of a metal.

SUMMARY

[0007] Embodiments of the invention are directed to methods for processing materials using femtosecond duration (i.e., 1-999 fs) laser pulses, applications of such methods, and altered materials and/or material properties resulting from such methods. Some embodiments of the invention are directed to methods for altering the surface structure of metal and other materials by application of one or more femtosecond duration laser pulses, applications of such methods, and altered materials and/or material properties resulting from such methods. According to non-limiting aspects, methods for uniformly coloring, non-uniformly coloring, and blackening a metal or other material, increasing a material's absorptance (up to nearly 100%), increasing a material's surface area, as well as altered materials exhibiting these characteristics are disclosed.

[0008] In one non-limiting example, there is a metal or metal alloy including at least one surface region including a plurality of micro-scale structure shapes and a plurality of nano-scale structure shapes, wherein the at least one surface region is super-hydrophobic, wherein the at least one surface portion has a spectral reflectance of less than 60% for at least some wavelengths of electromagnetic radiation in the range of 0.1 μm to 500 μm .

[0009] The at least one surface portion may have a spectral reflectance of less than 40% for electromagnetic radiation having wavelengths of 0.1 μm to 2 μm . The at least one surface portion may have a spectral reflectance of less than 5% for electromagnetic radiation having wavelengths of 0.1 μm to 2 μm . The at least one surface portion may have a spectral reflectance of less than 30% for at least some wavelengths of electromagnetic radiation in the range of 0.3 μm to 3 μm and the at least on surface portion has a spectral reflectance of greater than 50% for at least some wavelengths of electromagnetic radiation in the range of 3 μm to 50 μm .

[0010] The micro-scale structures may be at least one of a plurality of micro-grooves, a plurality of micro-protrusions, a plurality of micro-cones, a plurality of micro-columns, and a plurality of micro-cavities. The micro-scale structures may be a plurality of micro-grooves that are parallel. A spacing of the parallel micro-grooves may be approximately 0.1-500 μm . A spacing of the parallel micro-grooves may be approxi-

mately 100 μm . A depth of the parallel micro-grooves may be approximately 1-150 μm . A depth of the parallel micro-grooves may be approximately 1-50 μm . A depth of the parallel micro-grooves may be approximately 50-100 μm .

[0011] At least some of the plurality of nano-scale structures may be nano-scale structures extending into the micro-scale structures and nano-scale structures extending out from the micro-scale structures. At least some of the nano-scale structures extending out from the micro-scale structures may be nano-scale spherical structures. At least some of the nano-scale spherical structures may have diameters in the range of 5-25 nm. At least some of the nano-scale structures extending into the micro-scale structures may be nano-scale cavities.

[0012] The surface portion further may include a hydrophobic coating on top of the plurality of micro-scale and nano-scale structures.

[0013] In another non-limiting example, a metal or metal alloy includes at least one surface portion including hierarchical nano-structures and micro-structures, wherein the at least one surface portion has a water contact angle of 135° or greater, wherein the at least one surface portion has a spectral reflectance of less than 20% for at least some wavelengths of electromagnetic radiation in the range of 0.1 μm to 10 μm .

[0014] The at least one surface portion may have a water contact angle of 150° or greater, wherein the at least one surface portion has a spectral reflectance of less than 10% for at least some wavelengths of electromagnetic radiation in the range of 0.1 μm to 10 μm .

[0015] In another non-limiting example, a method for treating a metal or metal alloy to modify optical and hydrophobic properties of the metal or metal alloy includes: exposing a surface region of the metal or metal alloy to one or more femtosecond duration laser pulses sufficient to alter a surface structure of the metal or metal alloy to form a plurality of nano-scale structure shapes on the surface region and a plurality of micro-scale structure shapes on the surface region; wherein the surface region has a pre-laser treatment surface profile, the metal or metal alloy having a first electromagnetic absorption for the pre-laser treatment surface profile and the surface region having a first hydrophobicity for the pre-laser treatment surface profile; wherein the formed micro-scale and nano-scale structure shapes increase the absorption of at least some electromagnetic wavelengths of the metal or metal alloy so that the metal or metal alloy has a second electromagnetic absorption greater than the first electromagnetic absorption; wherein the formed micro-scale and nano-scale structure shapes increase the hydrophobicity of the surface region so that the surface region has a second hydrophobicity greater than the first hydrophobicity.

[0016] The formed plurality of microscale structure shapes on the surface region may include a plurality of microscale grooves extending into the pre-laser treatment surface profile. At least some of the formed plurality of microscale grooves may have a spacing in the range of 50 μm to 150 μm . The formed plurality of nanoscale structure shapes comprise a plurality of nanoscale cavities and nanoscale protrusions covering at least portions of the microscale structure shapes. At least some of the formed nanoscale protrusions may be nanospheres.

[0017] Forming the plurality of microscale and nanoscale structure shapes on the surface region may increase the

hydrophobicity of the surface region so that the surface region becomes super-hydrophobic. Forming the plurality of microscale and nanoscale structure shapes on the surface region may increase the metal or metal alloy's absorption of substantially all visible light wavelengths to give the metal or metal alloy a black or grey appearance. Forming the plurality of microscale and nanoscale structure shapes on the surface region may increase the metal or metal alloy's absorption of visible light wavelengths such that a spectral reflectance of the visible light wavelengths of the metal or metal alloy is below 5% after exposure to the femtosecond duration laser pulses. Forming the plurality of microscale and nanoscale structure shapes on the surface region may increase the metal or metal alloy's absorption of at least some electro-magnetic wavelengths in the range of 0.25-3 μm , wherein, after exposure to the femtosecond duration laser pulses, spectral reflectance for the metal or metal alloy of at least some electro-magnetic wavelengths in the range of 0.25-3 μm is lower than spectral reflectance for the metal or metal alloy of at least some electro-magnetic wavelengths in the range of 3-50 μm .

[0018] Forming the plurality of microscale structure shapes may include forming a plurality of microscale grooves having a periodic spacing in the range of 50 μm to 100 μm and having depths in the range of 5 μm to 20 μm .

[0019] In another non-limiting example, a metal or metal alloy includes at least one surface region including a plurality of microscale structure shapes and a plurality of nanoscale structure shapes, wherein the at least one surface region is super-hydrophobic, wherein the at least one surface portion has a spectral reflectance of less than 10% for at least some visible wavelengths of electromagnetic radiation.

[0020] At least some of the nanoscale structure shapes may cover at least some of the microscale structure shapes. At least some of the nanoscale structure shapes may include spherically shaped nanoscale structure shapes. The microscale structure shapes may be a plurality of microscale grooves.

[0021] The at least one surface portion may have an average spectral reflectance for wavelengths of electromagnetic radiation in the range of 0.2 μm to 3 μm that is lower than an average spectral reflectance for wavelengths of electromagnetic radiation in the range of 3 μm to 50 μm .

[0022] The at least one surface region may have a water contact angle of 150° or greater.

[0023] In another non-limiting example, a light sensor configured to convert light into electric current includes at least one metal or metal alloy surface region including a plurality of microscale structure shapes and a plurality of nanoscale structure shapes, wherein the at least one surface region is super-hydrophobic, wherein the at least one surface portion has a spectral reflectance of less than 10% for at least some visible wavelengths of electromagnetic radiation.

[0024] In another non-limiting example, a photovoltaic cell configured to convert light into electricity includes at least one metal or metal alloy surface region including a plurality of microscale structure shapes and a plurality of nanoscale structure shapes, wherein the at least one surface region is super-hydrophobic, wherein the at least one surface portion has a spectral reflectance of less than 10% for at least some visible wavelengths of electromagnetic radiation.

BRIEF DESCRIPTION OF THE DRAWINGS

[0025] The patent or application file contains at least one drawing executed in color. Copies of this patent or patent application publication with color drawing(s) will be provided by the Office upon request and payment of the necessary fee.

[0026] FIG. 1 is a graph that plots the absorptance of a gold (Au) surface against number of fs laser pulses of varying fluence from a Ti:sapphire laser having a central wavelength of 0.8 μm and a pulse duration of 60 fs, and further shows four regimes for absorptance change: AB, BC, CD, and DE, according to an illustrative embodiment of the invention;

[0027] FIGS. 2A, 2B are scanning electron micrograph (SEM) images of a gold surface (a) before irradiation and (b) after one shot from the laser described in the legend to FIG. 1, showing nanoscale roughness (2B) corresponding to the region AB in FIG. 1, according to an illustrative embodiment of the invention;

[0028] FIGS. 3A, 3B are SEM images of nanoscale surface structural features produced on a gold surface (region BC of FIG. 1) from the laser described in the legend to FIG. 1: (a) nanobranches after two shot ablation; (b) spherical nanoparticles after five shot ablation, according to an illustrative embodiment of the invention;

[0029] FIGS. 4A, 4B are SEM images showing nanostructure-covered, laser induced periodic surface structures (NC-LIPSS) in an irradiated area of a sample after 20,000 shots at a fluence of $F=0.17 \text{ J/cm}^2$ (region CD in FIG. 1) from the laser described in the legend to FIG. 1: (a) SEM micrograph showing the period of the NC-LIPSS; (b) nanobranches and supported spherical nanoparticles in the NC-LIPSS, according to an illustrative embodiment of the invention;

[0030] FIGS. 5A, 5B are SEM images showing (a) NC-LIPSS on the periphery of the irradiated area and gold-black deposit outside the irradiated area after 10,000 shots at a fluence of $F=1.1 \text{ J/cm}^2$ (region DE in FIG. 1) from the laser described in the legend to FIG. 1; (b) gold-black deposit after 20,000 shots at $F=0.17 \text{ J/cm}^2$ (region CD in FIG. 1) consisting of spherical aggregates with a mean diameter that decreases as the distance from the crater increases, according to an illustrative embodiment of the invention;

[0031] FIG. 6 is an SEM image of spherical nanoparticles in a spherical aggregate of the gold-black deposit shown in FIG. 5;

[0032] FIGS. 7A, 7B are SEM images of (A) a crater produced by 5,000 shots at $F=0.17 \text{ J/cm}^2$; and (B) a crater produced by 5,000 shots at $F=1.1 \text{ J/cm}^2$, according to an illustrative embodiment of the invention;

[0033] FIG. 8 is a graph of the residual energy coefficients of aluminum (Al) versus laser fluence following ablation with a single 55 ns pulse from a Nd:YAG laser at various ambient gas conditions, presented for illustrative effect;

[0034] FIG. 9 is a graph of the residual energy coefficients for aluminum versus laser fluence following ablation with a single 45 ns pulse of a ruby laser at various ambient gas conditions, presented for illustrative effect;

[0035] FIGS. 10A, 10B are open-shutter photographs of plasmas produced by 55 ns Nd:YAG laser pulses in 1 atm air and in vacuum at (A) $F=4.7 \text{ J/cm}^2$ and (B) $F=19.5 \text{ J/cm}^2$, where the laser beam is normally incident on the sample from the left (the white dashed lines indicate the front surface of the sample), according to an illustrative embodiment of the invention;

[0036] FIG. 11A is a graph of estimates of surface temperatures of Al samples for a Nd:YAG laser pulse at F_{abl} approximately equal to $F_{pl}=1.4 \text{ J/cm}^2$ in 1 atm. air (solid line) and at F_{abl} approximately equal to $F_{pl}=2.7 \text{ J/cm}^2$ in vacuum at a base pressure of 0.01 torr (dotted line); FIG. 11B is a graph of estimated surface temperatures of Al samples for a ruby laser pulse at F_{abl} approximately equal to $F_{pl}=1.1 \text{ J/cm}^2$ in 1 atm. air (solid line) and at F_{abl} approximately equal to $F_{pl}=2.1 \text{ J/cm}^2$ in vacuum at a base pressure of 0.01 torr (dotted line), according to an illustrative embodiment of the invention;

[0037] FIG. 12 is a graph of the residual energy coefficients of Al in air at various pressures versus laser fluence following single pulse fs laser ablation using a Ti:sapphire laser producing 60 fs pulses with a central wavelength of about 0.8 μm at a base vacuum pressure of about 0.01 torr, according to an illustrative embodiment of the invention;

[0038] FIG. 13A is a SEM image of a mechanically polished Al surface before laser irradiation; FIG. 13B is a SEM image of a typical surface modification of the Al after 1 shot at $F<F_{abl}=0.053 \text{ J/cm}^2$ in 1 atm. air using the fs laser described in the legend to FIG. 12, according to an illustrative embodiment of the invention;

[0039] FIG. 14 is a SEM images of the Al surface after 1 shot at $F=F_{pl}=0.086 \text{ J/cm}^2$ in 1 atm. air using the fs laser described in the legend to FIG. 12, showing the number and size of spherical nanoparticles on the surface being greater than those at $F=F_{abl}$ (i.e., than in FIG. 13(B)), according to an illustrative embodiment of the invention;

[0040] FIG. 15 shows open shutter photographs of plasma produced by a single fs laser pulse at $F=1.16 \text{ J/cm}^2$ in vacuum (pressure of about 0.01 torr) using the laser described in the legend to FIG. 12, where the laser beam is normally incident on the target from the left (the white dashed line indicates the front surface of the sample), according to an illustrative embodiment of the invention;

[0041] FIGS. 16(A-D) are SEM images of nanoscale structures in the center of the irradiated spot on a copper sample following ablation at $F=0.35 \text{ J/cm}^2$ using a Ti:sapphire laser with a central wavelength of 0.8 μm and a pulse duration of 65 fs: (A) sample surface before irradiation; (B) a different area of the copper surface after one shot ablation showing random fine nanostructures in the form of nanoprotusions, nanocavities, and nanorims; (C) after two shot ablation; (D) after 1,000 shot ablation, according to an illustrative embodiment of the invention;

[0042] FIGS. 17(A-D) show SEM images of the central part of the irradiated spot on copper following ablation at $F=1.52 \text{ J/cm}^2$ using the laser described in the legend to FIG. 16: (A) surface after one shot exhibiting random nanostructures in the form of nanoprotusions and nanocavities; (B) surface after two shot ablation showing random nanostructures in the form of spherical nanoprotusions and nanocavities; (C) surface after 10 shots showing both nano- and microstructures; (D) surface after 1,000 shots showing predominantly microstructures, according to an illustrative embodiment of the invention;

[0043] FIG. 18 shows a SEM image of copper following two shot ablation at $F=9.6 \text{ J/cm}^2$ using the laser described in the legend to FIG. 16, showing only microstructures in the central area and nanostructures on the periphery of the ablated spot; the insert shows microstructural details in the central area;

[0044] FIG. 19 shows a summary graphic of the different types of structural features observed under a SEM on a copper surface as a function of laser fluence and number of shots, derived using the fs duration laser pulses obtained from the laser described in the legend to FIG. 16, according to an illustrative embodiment of the invention;

[0045] FIG. 20A shows an image of a copper sample surface before irradiation; FIG. 20B shows an image of nascent nanostructures formed on copper by ablation at $F=0.35 \text{ J/cm}^2$ with a single laser pulse using the laser described in the legend to FIG. 16, according to an illustrative embodiment of the invention;

[0046] FIGS. 21A, 21B are SEM images showing the evolution of nanostructure-covered, laser induced periodic surface structures (NC-LIPSS) in the central area of the irradiated spot on a platinum (Pt) sample at $F=0.16 \text{ J/cm}^2$ delivered from a Ti:sapphire laser system that generates 65 fs pulses with a central wavelength of $0.8 \mu\text{m}$: (A) initial random nanoroughness formed after 10 shots (the inset shows a detailed view of the nanoroughness); (B) nanostructure-covered LIPSS after 30 shots (the inset shows a detailed view);

[0047] FIGS. 22(A-D) show SEM images illustrating the formation of NC-LIPSS in the peripheral area of the irradiated spot on Pt at $F=0.16 \text{ J/cm}^2$ with 100 shots using the laser described in the legend to FIG. 21: (A) general view of ablated spot; (B) the magnified details show that LIPSS disappears in the central area; (C) nanostructure-covered LIPSS with a period of $0.62 \mu\text{m}$ in the peripheral area; (D) further magnified detail of (C), according to an illustrative embodiment of the invention;

[0048] FIG. 23 is a graph showing Atomic Force Microscopy (AFM) measurements of the surface profile following mechanical polishing and 10 laser shots using the laser described in the legend to FIG. 21, according to an illustrative embodiment of the invention;

[0049] FIG. 24 is a graph showing a NC-LIPSS profile measured with AFM following 30 laser shots using the laser described in the legend to FIG. 21, according to an illustrative embodiment of the invention;

[0050] FIG. 25 is a SEM image showing nanostructure-covered LIPSS with a period of $0.58 \mu\text{m}$ in the central area of the irradiated spot on Au after 100 shots at a fluence of $F=0.16 \text{ J/cm}^2$ using the laser described in the legend to FIG. 21, according to an illustrative embodiment of the invention;

[0051] FIGS. 26(A-D) are SEM images of nanoroughness on a titanium (Ti) sample following fs laser treatment at near damage threshold fluence of $F=0.067 \text{ J/cm}^2$ using a Ti:sapphire laser system that generates 65 fs pulses with a central wavelength of $0.8 \mu\text{m}$: (A) sample surface before irradiation; (B) nanoroughness after two shot laser treatment; (C) after 10 shot treatment; (D) a magnified view of a section in (B) showing fine surface nanostructures in the forms of nanopores and nanoprotusions typically of spherical shape, according to an illustrative embodiment of the invention;

[0052] FIGS. 27(A-D) show SEM images illustrating the nanotopography of Ti following femtosecond laser treatment at $F=0.084 \text{ J/cm}^2$ using the laser described in the legend to FIG. 26: (A) nanoroughness after one shot; (B) nanoroughness after two shots; (C) a magnified view of a section in (A) showing fine details of surface nanoroughness; (D) magnified view of a section in (B) showing fine details of surface nanoroughness;

[0053] FIGS. 28(A-D) show SEM images illustrating fs laser produced periodic surface patterns on Ti following laser treatment at $F=0.067 \text{ J/cm}^2$ using the laser described in the legend to FIG. 26: (A) periodic surface pattern after 40 shots; (B) periodic surface pattern after 100 shots; (C) periodic surface pattern after 400 shots; (D) a magnified view of a section in (C) showing fine details of the periodic pattern covered with nanostructural features, according to an illustrative embodiment of the invention;

[0054] FIGS. 29(A-D) show SEM images illustrating fs laser produced periodic surface patterns on Ti following laser treatment at $F=0.084 \text{ J/cm}^2$ using the laser described in the legend to FIG. 26: (A) periodic surface pattern after 20 shots; (B) periodic surface pattern after 400 shots; (C) periodic surface pattern after 800 shots; (D) a magnified view of a section in (C) showing fine details of the periodic pattern covered with nanostructural features, according to an illustrative embodiment of the invention;

[0055] FIGS. 30(A-D) show SEM images illustrating the surface nano- and microtopography of Ti following fs laser treatment at $F=0.16 \text{ J/cm}^2$ using the laser described in the legend to FIG. 26: (a) nanoroughness after one shot; (b) nano- and microroughness after 20 shots; (c) typical microroughness covered with nanostructures after 40 shot treatment; (d) typical columnar microstructure after 200 shot treatment, according to an illustrative embodiment of the invention;

[0056] FIGS. 31(A-D) show SEM images illustrating the surface topography of Ti following fs laser treatment at $F=0.35 \text{ J/cm}^2$ using the laser described in the legend to FIG. 26: (a) nano and microroughness after one shot laser treatment; (b) typical random microroughness covered with nanostructures after 40 shot treatment; (c) typical columnar microstructures after 100 shot treatment; (d) typical columnar microstructures after 200 shot treatment, according to an illustrative embodiment of the invention;

[0057] FIGS. 32(A-D) show SEM images illustrating the surface topography of Ti following fs laser treatment at $F=0.48 \text{ J/cm}^2$ using the laser described in the legend to FIG. 26: (a) microroughness covered with nanoroughness after 40 shots; (b) typical microstructures following 70 shot treatment; (c) typical microstructures following 100 shot treatment; (d) a crater with a diameter of about $350 \mu\text{m}$ after a 1,500 shot treatment, according to an illustrative embodiment of the invention;

[0058] FIGS. 33(A-D) show SEM images illustrating the surface topography of Ti following fs laser treatment at $F=2.9 \text{ J/cm}^2$ using the laser described in the legend to FIG. 26: (a) smooth surface with microinhomogeneities after a one shot laser treatment; (b) smooth surface with some nanostructures after two shots; (c) a magnified view of a section in (b) showing surface nanostructures; (d) nanotopography of a smooth surface following 4 shot treatment with observable spherical nanostructures as small as about 10 nm, according to an illustrative embodiment of the invention;

[0059] FIG. 34 shows a plot of % reflectance versus wavelength in nm for polished Al (open circles); "black" Al (black diamonds; see also FIG. 35(A)); grayed Al (gray circles; see also FIG. 35(B)); "golden" Al (gray squares; see also FIG. 35(C)); and, Al colored by NC-LIPSS (open squares; see also FIG. 36), according to an illustrative embodiment of the invention;

[0060] FIGS. 35(A-C) show photographs of metals processed to have different optical properties: (A) black Al; (B) grayed Al with two gray shades; (C) golden Al, according to an illustrative embodiment of the invention;

[0061] FIGS. 36A, 36B show photographs of Al colored by NC-LIPSS, where the color of the samples depend upon the viewing angle due to a grating effect, according to an illustrative embodiment of the invention;

[0062] FIG. 37 is a schematic diagram that illustrates the so-called contact angle of a water/liquid drop deposited on the horizontal surface of a solid;

[0063] FIG. 38: (a) Photograph of an altered glass sample; (b-d) SEM images of microgrooves (b), and finer micro- and nanostructural features on the microgrooves [(c) and (d)], according to exemplary aspects of the invention;

[0064] FIG. 39 shows a 3D optical image of the surface microgrooves of the altered material shown in FIG. 38, according to an illustrative aspect of the invention;

[0065] FIGS. 40 (a-f) show the spreading dynamics of water on a horizontally positioned glass sample, according to an illustrative aspect of the invention;

[0066] FIGS. 41(a-f) show the spreading dynamics of water on a vertically positioned glass sample with grooves oriented parallel to the table, according to an illustrative aspect of the invention;

[0067] FIGS. 42 (a-f) show the dynamics of water running uphill on a vertically standing glass sample with grooves oriented perpendicular to the table, according to an illustrative aspect of the invention;

[0068] FIG. 43 shows a plot of uphill distance traveled by water front vs. $t^{1/2}$, according to an illustrative aspect of the invention;

[0069] FIG. 44: (a) Photograph of a tooth with a laser-treated area on the enamel surface; (b) 3-D optical image of the laser-produced microgrooves; (c) and (d) SEM images showing fine micro- and nano-roughness on the surface of the grooves, according to an illustrative aspect of the invention;

[0070] FIG. 45: (a) Photograph of a tooth with a laser-treated area on the enamel surface; (b) 3-D optical image of the laser-produced microgrooves; (c) and (d) SEM images showing fine micro- and nano-roughness on the surface of the grooves, according to an illustrative aspect of the invention;

[0071] FIG. 46: (a) and (b) Water spreading dynamics on the laser-treated enamel surface positioned horizontally; (c) and (d) Water spreading dynamics on the laser-treated enamel surface positioned vertically, according to an illustrative aspect of the invention;

[0072] FIG. 47: (a) and (b) Water spreading dynamics on the laser-treated dentin surface positioned horizontally; (c) and (d) Water spreading dynamics on the laser-treated dentin surface positioned vertically, according to an illustrative aspect of the invention;

[0073] FIG. 48: SEM images showing typical structural features of treated platinum surfaces; (a) and (b) Structure of parallel grooves; (c) and (d) Micro- and nanostructural features, according to an illustrative aspect of the invention;

[0074] FIG. 49: (a-d) Spreading dynamics of methanol on a horizontal platinum sample, according to an illustrative aspect of the invention; and

[0075] FIG. 50: Photographs showing methanol running uphill on a vertically standing platinum sample; (a-d) Dynamics of methanol running uphill; (e-f) Pictures show-

ing transportation and accumulation of methanol to an elevated point 10 mm above the reservoir surface, according to an illustrative aspect of the invention.

[0076] FIG. 51(a) is a photograph of an example of superhydrophobic black platinum.

[0077] FIG. 51(b) is a laser microscopy image showing micro-structure on the platinum surface of FIG. 51(a).

[0078] FIGS. 51(c) and (d) are SEM images showing the detailed hierarchical structures on the platinum surface of FIG. 51(a).

[0079] FIGS. 51(e) and (f) are laser microscopy images showing surface structures on examples of brass and titanium.

[0080] FIGS. 52(a) through (f) are video clips showing a water droplet bouncing off a superhydrophobic black platinum surface, which has a tilt angle of 8° .

[0081] FIGS. 53(a) through (e) are video clips showing a superhydrophobic platinum surface that is self cleaned by water droplets. The surface has a tilt angle of 8° .

[0082] FIG. 53(f) shows an untreated platinum surface that has accumulated a puddle of water with floating dust.

[0083] FIG. 54 shows the spectral reflectance of the examples of black brass, black platinum, and black titanium of FIG. 51, shown as a function of wavelength. Spectral reflectance of three mechanically polished metals without laser treatment is also shown for comparison. The dashed line shows the spectral reflectance of an ideal solar absorber.

DETAILED DESCRIPTION OF NON-LIMITING, EXEMPLARY EMBODIMENTS OF THE INVENTION

[0084] Embodiments of the present invention are generally directed to laser-based materials processing using one or more femtosecond duration (i.e., 1-999.99 fs) laser pulses, and to the altered materials obtained by such materials processing. As used herein, the term ‘materials processing’ and ‘surface treatment’ refer to altering the surface structure or restructuring the surface of the material being processed by creating various nanostructures that may or may not be created in combination with additional micro- and macro-structures. Non-limiting examples of nanostructured surfaces in accordance with embodiments and aspects of the invention are shown in the figures and will be described in detail below.

[0085] Material alterations obtained in accord with embodiments of the present invention may be defined by a variety of experimental methods for analyzing the alterations obtained (synonymously “the materials processing outcome(s)"); for example, by electron micrographic analysis, by spectroscopic analysis (e.g., absorption of light or other electromagnetic energy by the altered surface), and via other techniques recognized in the art. Material alterations may also be additionally and/or separately defined in terms of theoretical modeling of alterations and the mechanisms by which alterations are generated, e.g., by post-ablation redeposition of material, by the formation of nanostructure-covered, laser induced periodic surface structures (NC-LIPSS), and others described herein and known in the art.

[0086] In this regard, the term “ablation” is used to refer to material alterations generally, rather than to any specific process of material alteration. Specifically, “ablation” is defined as occurring by experimental observation, i.e., by the onset of surface damage or alteration to the material being processed, where the surface damage or alteration is

typically observed by eye or by SEM analysis (see, e.g., Example 2). Thus the term “ablation” is generic, and is not used to refer to a specific physical process of material alteration, for example, the specific physical process of vaporization or other form of removal of material from a surface, etc.

[0087] The structural material alterations described herein below may be defined more precisely as, e.g., “nanostructures,” “nanoscale structure,” “nanoscale roughness,” or “nanoroughness” obtained by femtosecond laser pulse nanostructuring of the material. Other alterations that may or may not occur in the presence of nanostructuring include, without limitation, “microstructures,” “microscale structure,” “microscale roughness,” or “microroughness” obtained by microstructuring effects obtained by femtosecond laser pulse nanostructuring of the material, and “macrostructures,” “macroscale structure,” “macroscale roughness,” or “macroroughness” such as craters or other features obtained by macrostructuring effects obtained by femtosecond laser pulse nanostructuring of the material.

[0088] With further regard to nanostructures, terms including but not limited to “nanobranches,” “nanoparticles,” “nanoprotrusions,” “nanocavities,” “nanorims,” “nanopores,” nanospheres” are used to describe nanoscale dimension alterations having the visual appearances under SEM analysis of branches, particles, protrusions, cavities, spheres, channels, etc. With regard to microstructures, for example, “columnar microstructures” is used to refer to microstructures that appear visually under SEM analysis as columns (see, e.g., FIGS. 30 and 31; FIGS. 3, 6, and 26 show illustrative examples of these different micro- and nanostructures).

[0089] Further with regard to the above terms, SEM analysis may be used to establish quantitative as well as qualitative definitions for macro-, micro-, and nanostructures, and these definitions may be used to define the materials obtained by the materials processing methods according to embodiments and aspects of the invention.

[0090] In some non-limiting aspects of the invention, it may be desirable to create essentially a single kind of materials structuring, while in other non-limiting aspects it may be advantageous to create ‘mixed’ structuring. In this context the word “dominated” is used herein to refer to a situation where one type of structuring is prevalent, i.e., where one type of structuring occurs across, e.g. about 80% or more of the surface area of the surface produced by the specified materials processing regime. In general, however, when the surface is “dominated” by nanostructures, for example, it will be understood that other percentage values are explicitly contemplated; i.e., 70, 71, 72, 73, 74, 75 . . . 97, 98, 99% (i.e., counting by 1% intervals) of the surface area is of the structure specified.

[0091] Although the above visually-based terms are used herein to classify nanostructuring, microstructuring, and macrostructuring effects according to embodiments of the invention, other methods can be used to categorize these structures. For example, because the absorbance of a material is a function of the intrinsic absorbance, A_{INTR} , and the surface roughness, A_{SR} , alterations to a material that manifest as alterations in surface roughness may be described by absorbance changes rather than, or in addition to, descriptions of macro-, micro-, or nanostructural changes based on changes in the visual appearance. Thus Example 1 below shows in detail how different femtosecond pulse duration

laser processing regimes alter absorbance, and how these alterations in absorbance correlate with macro-, micro- and nanostructural changes in the surface of the material.

[0092] Further with regard to absorbance, as discussed in Example 1 and particularly shown in FIG. 1, the materials processing regimes of the embodiments of the invention are capable of producing alterations to materials resulting in extremely high absorptivity; e.g., absorptivity for gold of close to 100%. Such high absorptivity may have particular utility in, e.g., heat absorption applications (e.g., heat exchange and heat absorption for hot water heating from solar energy, etc.). However, as FIG. 1 shows, other absorbance values may also be obtained. Thus the present invention is directed to producing materials having absorbance values from 0.01, 0.02, 0.03, 0.04, 0.05, . . . , 1.0 (counting by 0.01), where the resulting absorbance of the material is significantly greater than before processing.

[0093] The absorbance values determined in Example 1 are measured calorimetrically; however, absorbance may also be measured by other means, and specifically by methods that allow absorbance to be determined as a function of the wavelength of the light impinging on the sample. Reflectivity may also be measured in addition to, or in substitution for, absorbance, especially in situations where it is desirable to produce a material with favorably altered reflectivity. Reflectivity may be measured by any standard method used for such determinations; examples of reflectivity measurements are provided in, for example, U.S. Pat. No. 4,972,061, the contents of which are incorporated herein by reference in their entirety.

[0094] Thus in a non-limiting, exemplary aspect, materials processing methods and resulting altered or treated materials are directed to the field of jewelry. The surface of virtually any metal or metal alloy such as, but not limited to, gold, platinum, silver, stainless steel, various precious metals, decorative metals, and others may be decorated, initialed, patterned, colored, blackened, or otherwise marked via femtosecond laser surface structuring so as to have, for example, altered reflectivity ranging from the reflectivity of the unmarked metal down to essentially 0% reflectivity, depending upon the desired application. In various non-limiting aspects, reflectivity may vary with wavelength (producing different colors) and/or viewing angle.

[0095] According to the various embodiments described herein, the materials to be altered by femtosecond laser surface structuring include most generally all metals and alloys thereof, including, but not limited to, gold, aluminum, copper, platinum, titanium, tungsten, stainless steel, and others. The alteration of semiconductor materials and dielectrics are contemplated. Also contemplated are ceramic, glass, and plastic materials.

[0096] According to non-limiting aspects, metal materials are intended to include metal films (e.g., thin metal layers coated on glass, silicon or other additional underlying layer) and bulk metals. Bulk metals refer to non-thin films of more than a few hundred nm, particularly more than 1 μm , and more particularly to more than 10 μm in thickness. Thus “bulk metals” refers to metals with the characteristics just recited, whereas “thin films” refers to metals of less than a few hundred nm, including the thin films described in the Examples below.

[0097] Further with regard to the materials of the present invention, as shown in the Examples and in, e.g., FIGS. 13-14, there is evidence that various of the alterations of the

materials obtained by the embodied materials processing methods occur preferentially on surface defects of the materials being irradiated by the femtosecond laser pulse(s). Thus in some aspects, highly polished materials will be used (pre-processing) in order to reduce the preferential formation of material alterations at material defects; in other situations, it may be advantageous to leave the material unpolished, to roughen the material, or even to introduce inhomogeneities or other “defects” into the material in order to facilitate certain alterations.

[0098] Pulse duration is a function of the laser system used. In various non-limiting embodiments, the laser system is a Ti:sapphire laser system generating 65 fs duration pulses at a central wavelength of 0.8 μm ; however, other laser systems generating different fs pulse durations are also contemplated. See, e.g., U.S. Pat. No. 6,979,798 and U.S. Publication No. 2006/0207976 A1, the contents of which are incorporated herein by reference in their entirety, for non-limiting descriptions of other such fs duration laser systems, e.g., a Yb-doped fiber laser such as the FPCA uJewel (available from IMRA America, Ann Arbor Mich.). Other such fs duration lasers may include, e.g., dye lasers, Cr:LiSAF lasers, KrF lasers, and others known in the art.

[0099] In addition to laser pulse duration, a number of other laser parameters may be varied in various aspects of the present invention in order to obtain the desired materials processing effects, including but not limited to: the polarization of the laser beam (typically horizontally polarized); the diameter of the spot of laser irradiation on the surface of the material sample (typically between 100 and 1200 μm); the wavelength of the laser beam; the energy density, F (fluence), of the laser beam; the number of laser pulses (shots) applied to the material sample; time delay between laser pulses; the extent of overlap between multiple laser pulses (shots) applied to the particular region of the material being processed; whether the shots are applied in vacuum or under higher pressure conditions, and others.

[0100] According to various non-limiting exemplary embodiments, the fs laser has a central wavelength (λ) of 0.8 μm . However, other wavelengths in the IR, visible, ultraviolet, infrared, THz frequency, etc., may be advantageously used.

[0101] With regard to laser fluence on the surface of the material to be processed, as will be discussed below, contemplated fluences will be sufficient to alter the surface structure of the metal as described herein and will be generally below about 25 J/cm^2 at the material surface; i.e., below about 25, 24, 23, 22, 21, 20, 19, 18, 17, 16, 15, 14, 13, 12, 11, 10, 9, 8, 7, 6, 5, 4, 3, 2, or 1 J/cm^2 . The exact choice of fluence varies, however, depending upon the desired materials processing effects. Thus for example, the summary graphic of FIG. 19 shows that different materials properties may be obtained for fs laser irradiation using different combinations of laser fluence and number of laser pulses.

[0102] Further with regard to fluence, in an exemplary embodiment the choice of fluence is expressed by reference to the threshold laser fluence (synonymously, the “ablation threshold” or F_{abl}) required for visible material surface damage under SEM. Thus as described in the Examples, materials processing effects can be calibrated to the ablation threshold, e.g., the fluence specified to obtain a particular effect may be given both in absolute terms of J/cm^2 or, alternatively, may be given as a percentage of the ablation

threshold, i.e., as 1, 2, 3, 4, 5, . . . , 100, 101, 102, 103, 104, 105, . . . 10,000% (counting by ones) of F_{abl} .

[0103] With regard to laser pulses, embodiments of the present invention may use single- and multi-pulse exposures of materials to obtain desired materials processing effects. Laser “pulse” or synonymously, “shot”, refers to a single laser pulse applied to the sample material using for example an electromechanical shutter to select a single pulse. Multi-pulse or multi-shot situations involve more than a single shot, e.g., 2, 3, 4, 5, 6, 7, 8, 9, 10, etc. (counting by ones) up to thousands, tens-of-thousands, or hundreds-of-thousands of shots. The exact number of pulses or shots chosen will depend upon the desired materials processing outcome, as shown in for example in the summary graphic of FIG. 19 and as discussed below.

[0104] The extent of overlap between shots in a multi-shot situation may be varied in order to obtain desired effects, e.g., by specifying that at least $x\%$ of the area of an additional shot or shots overlap with the first or previous shot, where x can be 1 to 100% counting by ones (i.e., 1, 2, 3, 4, 5, . . . , 100%). Such variations may be particularly important when, for example, the portion of the material in the center of the irradiation by the laser pulse or pulses undergoes different alterations as a result of the centrality of the beam than portions of the material at the periphery of the pulse or pulses (see, e.g., FIGS. 18 and 22).

[0105] As a result of shot overlap or other controllable parameters, a variable percentage of a surface may be altered to have the desired structure or structures. For example, a precise scanning pattern of a laser beam across the surface of the material may be used to ensure that a variable percentage of the surface is altered to possess the desired nanostructure(s), microstructure(s), macrostructure(s), or combinations thereof. Contemplated percentages of a surface to be modified range from 1 to 100% counting by ones (i.e., 1, 2, 3, 4, 5, . . . , 100%). As shown in FIG. 18, precise patterns of laser irradiation application, either at one fluence alone or in a combination of fluences (e.g., high fluence/low fluence) may influence the type of structuring of the material obtained. FIG. 18, for example, shows that a two shot high fluence regime at $F=9.6 \text{ J}/\text{cm}^2$ on copper will produce a mixed materials processing result of a microstructured central area surrounded by a nanostructured periphery.

[0106] In addition to specifying the percentage of the surface to be modified, the materials processing effects may also be expressed in terms of a total area modified, e.g., 0.1, 0.2, 0.3, 0.4, 0.5, . . . 10,000 cm^2 (counting by 0.1 cm^2 units). In this regard, it is advantageous that the embodied materials processing methods produce sufficiently large amounts of altered materials, where these amounts may be specified in terms of the total surface area of the material that has been altered.

[0107] The exact surface area or range of surface areas required for any particular application of the present invention will depend upon the application; aesthetic applications such as jewelry, for example, will require relatively small amounts of altered material. In contrast, larger surface areas of altered materials may be required for other applications, e.g., formation of heat absorptive surfaces, or for applications for, e.g., catalysis or materials implantation into the human body for, e.g., dental implants or other situations where nanostructuring is advantageous for cellular growth and penetration into the implant material.

[0108] According to non-limiting aspects of the invention, advantageous nanostructured materials processing effects may be obtained under ambient air/pressure conditions. Thus the pressure conditions under which materials processing occurs affect both the threshold laser fluence (synonymously, the “ablation threshold” or $F_{p,r}$) required for visible material surface damage under SEM and the plasma ignition threshold ($F_{p,r}$) as assayed by the onset of bright violet radiation from the laser-irradiated spot as measured either by a photomultiplier or an open-shutter camera (see, e.g., FIG. 12). Therefore, various embodiments of the present invention are directed to materials processing at: low-pressure conditions (e.g., below 5 torr), where, for example, related materials processing to produce “gold-black” is done; vacuum conditions (i.e., below 0.1 torr); between 5 torr and 760 torr (1 atm), i.e., 5, 6, 7, 8, 9, 10, . . . 760 torr (counting by ones); and, at atmospheric pressure, where the Examples provided below show desirable materials processing effects can occur, contrary to prior teachings that materials processing must be performed at low pressure.

[0109] Additionally, Example 2 below discusses the effects of ambient air versus a highly reactive gas (oxygen) versus an inert gas (helium) on materials processing using ns duration pulses, and concludes that these effects are dependent upon gas pressure, rather than the type of gas environment used. While these effects are expected to be applicable to fs duration pulses as well, non-limiting aspects of the present invention nevertheless contemplate the use of purified gases in addition to ambient air for use with the materials processing regimes. Inert gases may have particularly desirable effects, thus such gases or other purified gas or mixtures of gases may be used in aspects of the present invention.

Exemplary Method Embodiments

[0110] Embodiments of the invention use pulsed laser beams of femtosecond (fs) duration to obtain nanostructuring of material surfaces with or without microstructuring and/or macrostructuring effects. The specific conditions for generating a particular structure (macro-, micro-, or nano-) or combination of structures is a function of a number of variables including laser pulse duration, laser energy density or fluence (in J/cm^2), time delay between laser pulses, and the number of pulses or “shots” of the laser beam delivered to a particular region of the material to be altered.

[0111] As shown in the Examples below, both on theoretical and experimental grounds, fs pulses produce different materials processing effects than do ps and ns duration pulses. It is also observed that the materials processing effects obtained with fs laser pulses are not a priori uniform; rather, they depend in part upon the specific pulse parameters such as the energy density or fluence of the laser beam and the number of pulses of the laser beam applied to the sample. However, various combinations of beam fluence and shot number may advantageously produce more uniform materials processing results.

[0112] Example 1 below will describe the effects of beam fluence and shot number on a gold sample. The results are categorized into four discrete regions of effect, AB, BC, CD, and DE as shown in FIG. 1, which shows a graph of the absorbance of a gold (Au) surface against number of pulses of varying fluence from a Ti:sapphire laser (central wavelength of 0.8 μm ; pulse duration of 60 fs). The different absorbance values of the laser beam irradiated gold in

various of these regions can be correlated with differences in the materials alterations achieved; i.e., region AB is associated with nanoscale roughness (see also FIG. 2); region BC is associated with nanoscale roughness including nano-branches (see FIG. 3(a)) and spherical nanoparticles (see FIG. 3(b)) and also contains microscale structures such as micropores, circular microgrooves, and central microchannels; and, region CD contains macroscale structures such as craters, periodic structures, and other surface deformations (see, e.g., FIG. 7).

[0113] As Example 3 will show, the regions defined in Example 1 and shown in FIG. 1 are applicable not just to a gold material sample but are also observed to be very consistent across different materials. Thus Example 3 is specifically directed to an analysis of the effects of fluence and shot number of a fs laser beam on copper, with the SEM results for various experiments shown in FIGS. 16-18 and 20. FIG. 19 is a summary graphic that shows that there are essentially three regions defined by the data of Example 3: a region dominated by nanostructures (the X region in the figure); a region dominated by microstructures with some nanostructures (the open circle region in the figure); and, a region dominated by macrostructures with some micro- and nanostructures (the solid squares in the figure). These three regions correspond to regions AB, BC, and CD (or possibly CD/DE), respectively, of FIG. 1 and demonstrate that although there would be no a priori ability to predict the existence of these regions, once the regions have been defined, the structures formed for each region are relatively predictable.

[0114] Further confirmation of the general applicability of the three regions of FIG. 19 to other materials including, but not limited to, other metals, semiconductors, and dielectrics is provided by the data of Example 5, where titanium metal was exposed to a varying number of fs duration laser pulses of varying fluence. Specifically, Example 5 will show that nanostructures are present with low laser fluences (see, e.g., FIGS. 26-29) as expected, and that for higher fluences of, e.g., 0.16 or 0.35 J/cm^2 and a sufficient number of laser shots (e.g., 20-200; see FIGS. 30 and 31), microstructuring occurs as predicted by the data of FIG. 19. Finally, again as predicted by the data of FIG. 19, for 1,500 shots at a fluence of 0.48 J/cm^2 , macrostructures are formed as predicted (see, e.g., FIG. 32(d)).

Exemplary Applications

[0115] The apparatus and method embodiments described herein may have utility in a variety of applications including, but not limited to: aesthetic or marking applications such as the application of patterning or coloring to the surface of jewelry; medical applications, e.g., for implantable medical devices, where the novel properties of the laser altered surface of such a device may aid in, for example, integration of cells of a subject into the implant; catalysis, where the properties of the altered materials and particularly the increased surface area of the materials resulting from, e.g., nanostructuring, may improve the ability of the material to catalyze chemical reactions; heat transfer situations, where alterations resulting in increased absorptivity may improve, e.g., the efficiency of solar cells and heat sinks; sensor sensitivity, where the unique alterations to materials described herein may be used in both a sensor’s absorbing element to increase the amount of electromagnetic radiation absorbed and also in the shielding around the sensor or

sensors to protect them from various forms of stray electromagnetic radiation, thereby helping to improve their signal-to-noise ratios; and, stealth technologies or other technologies where the absorption of electromagnetic energy such as ultraviolet, visible, infrared, terahertz radiation, etc., may cloak, conceal, or otherwise obscure the object coated or shielded with the altered material having the desired absorptive properties.

Exemplary Aesthetic or Marking Applications

[0116] A non-limiting aspect of the invention is directed to methods for materials processing that produce altered materials for aesthetic or marking applications, for example jewelry or other applications where the nano-, macro-, or micro-structuring of a material's surface may produce desired effects.

[0117] The data of Example 1 will show that fs-based laser processing may be used to increase the absorptivity of a material, which can be observed visually as darkening or blackening of the surface region of the material so altered. Accordingly, an embodiment the invention is directed to a method of obtaining the desired markings. A related embodiment is directed to the materials obtained by such processing methods.

Exemplary Biomedical Applications

[0118] A non-limiting aspect the invention is directed to is a method for materials processing that produce materials advantageously suitable for biomedical applications, particularly medical applications where a metal or metal-clad device is to be implanted into a subject, and alterations to the metal or metal cladding may act to improve the biocompatibility of the metal or metal cladding.

[0119] In this aspect, suitable materials may include metals, ceramics, composites, and others, that are nanostructured and/or possibly microstructured and then introduced or implanted into a biological milieu such as in bone, in tissue, etc., where biocompatibility is important for successful introduction or implantation. The materials contemplated include any as are known for introduction or implantation into the body, and include, but are not limited to, metals such as titanium, gold, silver, etc., alloys of these metals, composites, etc. The "biological milieu" may include bone, tissue, etc., of a whole organism, or of an isolated component of an organism, e.g., of an isolated organ, teeth, bones, etc. Organisms contemplated include animals, and particularly mammals, including humans.

[0120] Example 5 below will discuss alterations to titanium metal using a fs laser method described herein to alter the surface topography of titanium for better biocompatibility, i.e., to provide a surface containing, e.g., pits, pillars, steps, etc., or other structural features that serve as anchors or other attachment, scaffolding, or stimuli for protein and/or cellular integration.

[0121] "Biocompatibility" as used herein refers generally to alterations in the surface of a material that increase the ability of that material to integrate into the body, e.g., increase structural integration such as by invasion or interpenetration of the material by cells of the body or proteins or other biological material. Biocompatibility also refers to alterations that increase integration by decreasing rejection of the material by the body, as would occur if the material

fails to integrate, i.e., so that the body recognizes the material as non-integrated and thus acts to encapsulate or otherwise reject it.

[0122] Biocompatibility may be assayed in a variety of ways. For implants, for example, biocompatibility may be determined by assaying the mechanical strength or stability of the integration of the implant into the body. Thus for example, in osseointegration of dental implants, biocompatibility may be assayed by determining the force required to displace or separate out the implant from the surrounding bone. Biocompatibility may also be determined by directly observing (e.g., by SEM) the extent to which proteins, cells, or other biological materials are able to invade or integrate into the metal or other material altered by the materials processing methods of the present invention. As another non-limiting example of an assay for biocompatibility, methods for measuring cell death or proliferation may be used to determine the extent to which the altered surface topography of the material processed by the laser methods of the present invention results in the activation of cells to proliferate, or the active suppression of cell death mechanisms that would otherwise occur if the cells failed to find themselves in a suitable proliferative environment.

Exemplary Catalysis Applications

[0123] A non-limiting aspect is directed to a method for fs laser pulse materials processing that can produce materials with desirable catalytic properties; i.e., materials that contain nanostructural and macro- and/or micro-structured alterations that increase catalytic surface area.

[0124] Such alterations may be assayed by SEM or other analyses that allow for the determination of the porosity or other increased surface area aspects of the materials altered. Alternatively, catalytic activity may be measured directly by determining the rate at which a reaction is catalyzed by an unaltered material (e.g., platinum) versus the rate of the reaction using an altered material.

Exemplary Modifications of the Optical Properties of Materials

[0125] An aspect of the invention is directed to a method for altering the optical properties of materials, including, but not limited to, metals such as are provided in Example 6 below. Thus as shown in Example 6, the materials processing methods of the present invention may be used to obtain, e.g., metals which appear to the human observer to have various shades of gray (where "gray" may alternatively be defined as a material having relatively uniform reflectance across the entire visible wavelength), including multiple shades of gray in one metal piece. These materials processing methods may additionally be used to obtain what appear to the human observer to be colored materials (where "colored" may alternatively be defined as a material having preferential reflectance in some regions of the visible spectrum and not in others), e.g., colored metals such as are also described in Example 6, and 'black' metal. Although these methods are applied to metals in Example 6, the present invention explicitly contemplates the application of these methods for certain non-metal materials as well.

Example 1

[0126] Experiments in support of embodiments of the invention have demonstrated that a significant amount of

residual thermal energy is deposited in metal samples following multi-shot femtosecond laser ablation. Traditionally, it was commonly believed that one of the most important advantages of femtosecond laser ablation is that the energy deposited by ultrashort laser pulses does not have enough time to move into the bulk sample; therefore, the residual thermal energy remaining in the bulk sample should be negligible. In contrast to this, a significant enhancement in laser light absorption was observed recently by the inventors following ablation. To understand the physical mechanisms of laser energy absorption, the change in absorptance of gold due to structural modifications following multi-shot femtosecond laser ablation was directly measured. The measured data indicates that there is a significant absorption enhancement due to nanostructuring in addition to the known mechanisms of absorption increase via micro- and macro-structuring. Moreover, nanostructuring alone may enhance the absorptance by a factor of about three. The physical mechanism of the total enhanced absorption is due to a combined effect of nano-, micro-, and macro-structural surface modifications induced by femtosecond laser ablation. At a sufficiently high fluence and with a large number of applied pulses, the absorptance of gold surface may reach an absorptance value of nearly 100%.

[0127] The absorptance A of a pure metal with a clean surface consists of two components $A=A_{INTR}+A_{SR}$, where A_{INTR} is the intrinsic absorptance and A_{SR} is the contribution due to surface roughness. For an optically smooth metal surface, A_{SR} is about 1-2% of A_{INTR} , but the role of A_{SR} enhances as the surface roughness increases. For multi-pulse ablation, only the first femtosecond laser pulse interacts with an undamaged surface, since the laser-induced surface structural modification develops long after the ultrashort pulse. In this case, A is governed by A_{INTR} , which can be a function of laser fluence due to laser-induced change in the dielectric constant of the material. All of the subsequent laser pulses interact with a structurally modified surface and their absorption is determined by both A_{INTR} and A_{SR} . The absorption of a single femtosecond laser pulse by an undamaged metal surface is dominated by A_{INTR} . However, the coupling of laser energy to a metal in multi-pulse femtosecond laser ablation has not yet been investigated, where A_{SR} may have a significant value due to surface structural modification.

[0128] The instant non-limiting example discusses the effect of surface structural modifications on the absorptance of gold in multi-pulse femtosecond laser ablation when an originally plane and smooth surface transforms into a blind hole. This effect is investigated as a function of the number of applied ablation pulses at various fluences. A reported calorimetry technique allows a direct measurement of laser energy absorbed by the sample. Our data indicate that femtosecond laser-induced surface modification enhances the sample absorptance, which can reach a value close to 100% at a sufficiently high fluence with a large enough number of applied pulses. Scanning electron microscope (SEM) studies show that there is absorption enhancement due to nanostructuring, which, alone was seen to enhance the absorptance by a factor of about three.

[0129] Experimentally, an amplified Ti:sapphire laser system was used to generate 60-fs pulses of about 1.5 mJ/pulse at 1 kHz repetition rate at a central wavelength of 800 nm. The laser beam was focused onto a mechanically polished sample surface with a 40-cm-focal-length lens at normal

incidence. An electromechanical shutter was used to select the number of pulses, N , applied to the sample. The absorptance of the ablated spot was studied. After ablation of the sample with a chosen number of pulses, we reduced the laser fluence to a level below the ablation threshold. Subsequently, we irradiated the ablated spot again using a train of low-fluence laser pulses that would not induce any further surface modification. A certain amount of energy from this low-fluence pulse train, E_A , is absorbed in the skin layer of the sample, dissipates via heat conduction in the sample, and causes a bulk temperature rise ΔT . We measured this temperature rise with a thermocouple battery that allows E_A to be determined calorimetrically as $E_A=C\Delta T$, where C is the known heat capacity of the sample. To measure energy E_T incident upon the sample, a certain fraction of incident pulse train energy was split off by a beam splitter and measured with a joulemeter. Having measured E_T and E_A , the absorptance of the ablated spot could be found as $A=E_A/E_T$. Laser-induced surface modifications were then studied using a SEM and an optical microscope.

[0130] The optical properties of surface modifications were studied following multi-pulse ablation at single-pulse laser fluences of $F=1.1, 0.35, 0.17,$ and 0.078 J/cm^2 in air. The ablation threshold F_{abl} for a pristine surface was found to be $F_{abl}=0.067$ and 0.048 J/cm^2 for single-pulse and 500-pulse train irradiation, respectively. The numbers of pulses required to perforate a 1 mm-thick sample at the center of the irradiated spot were determined to be 16,100, 25,000, and 77,000 pulses at $F=1.1, 0.35,$ and 0.17 J/cm^2 , respectively. This corresponds to average ablation rates of 63, 40, and 13 nm/pulse, indicating that a single laser pulse produces a nanoscale modification in depth. Plots of absorptance versus the number of ablation shots, N , at different F are shown in FIG. 1. For an undamaged surface, the absorptance remains a constant value of 0.12 when measured at $F=0.0043 \text{ J/cm}^2$, which is an order of magnitude below F_{abl} . The absorptance of a structurally modified surface is significantly greater than that of the undamaged surface and shows dependence on the number of applied ablation pulses, N .

[0131] The $A(N)$ curves for the ablated surface can be characterized into distinct regions marked with A, B, C, D, and E on $A(N)$ in the case of $F=0.17 \text{ J/cm}^2$ in FIG. 1. The first of these four regions is region AB, where the absorptance initially increases from 0.12 (undamaged surface) to a value in the range of 0.25-0.33. Typically, this region covers the first 1-10 shots. For example, this initial enhancement of absorptance can be produced by four pulses at $F=0.17 \text{ J/cm}^2$ or by one pulse at $F=0.35$ and 1.1 J/cm^2 . Optical microscopy showed that the irradiated spot was entirely covered with surface modification following ablation by only one pulse when $F\geq 0.35 \text{ J/cm}^2$, but four pulses at $F=0.17 \text{ J/cm}^2$. Therefore, the enhancement of A with N at $F=0.17 \text{ J/cm}^2$ appears due to both the surface modification and an increase in size of the modified area from point A to B.

[0132] In the second region, BC, the absorptance undergoes a slight decrease as N increases. Typically, this region covers approximately the next 100-300 pulses. Both regions AB and BC extend to a larger number of pulses when the surface is modified at F only slightly above F_{abl} , as seen from the curve at $F=0.078 \text{ J/cm}^2$ in FIG. 1.

[0133] The third region, CD, is characterized by a further enhancement of absorptance with the increase of N . This region extends to N on the order of 10,000 pulses.

[0134] The fourth region, DE, was where absorptance reached a maximum value that did not change with further increase of N.

[0135] Reference is now made to the SEM pictures of surface morphology shown in FIGS. 2-6. In regions AB, BC, and CD, where absorptance exhibits dependence on N, the following surface modifications were observed: For region AB, a characteristic modification is nanoscale roughness (FIG. 2). In region BC, two major features were observed. First, nanoscale roughness develops further in the form of nanobranches (FIG. 3 (a)) and spherical nanoparticles (FIG. 3 (b)). Secondly, microscale structures begin to develop in the forms of micropores, circular microgrooves, and central micro-channels. In region CD, features resembling a crater with a deep central micro-channel, periodic structures with orientation in the direction perpendicular to the laser light polarization and with a period roughly equal to the laser wavelength (FIG. 4(a)), and a visible black halo around the crater were observed. All these laser-induced surface modifications can affect the absorptance in various ways. For example, surface roughness can enhance the absorption of light both by multiple reflections in micro-cavities and by variation in the angle of incidence (angular dependence of Fresnel absorption). Nanoscale structural features can affect absorptance since the optical properties of a nanostructured material can be quite different from the bulk. Laser-induced periodic surface structures (LIPSS) may enhance absorption of laser energy via generation of surface electromagnetic waves. In accordance with non-limiting aspects of the instant invention, the observed LIPSS, referred to herein as nano-structure-covered laser-induced periodic surface structures (NC-LIPSS) having non-conventional, finer nanoscale structural features, are shown in FIG. 4 (b).

[0136] The absorption of laser energy in femtosecond laser ablation may also be altered through re-deposition of ablated material. Examination of the black halo produced around the crater shows that its elemental composition as determined by energy dispersive X-ray analysis is identical to that for a pristine surface; i.e., the black halo is a layer of the ablated and re-deposited gold. SEM images in FIGS. 5 and 6 demonstrate that the black halo has a structure of spherical nanoparticle aggregates that is typically seen in gold-black films and, which, have been known for their high absorptance in the infrared. Therefore, the gold-black halo can enhance the absorption of low-intensity wings of the incident Gaussian beam and contribute to residual heating of the sample. Since re-deposition of ablated material occurs both outside and within the ablated spot, the re-deposition of the nanoparticles produced by ablation can also enhance the absorption of light in the ablated area. For example, an enhanced absorption of light by a semiconductor coated with Au nanoparticles has recently been reported. Therefore, in femtosecond laser ablation, the enhanced absorption can occur due to surface nano-, micro-, macro-structures and re-deposition of nanoparticles depending on ablation conditions. The combined effect of these surface modifications can lead to virtually 100% absorption of laser light in multi-pulse ablation with a sufficiently large number of pulses at high fluence as shown in FIG. 1. Almost all of incident laser energy is retained in the sample as residual thermal energy. This suggests that the energy carried away by the ablated material is small in Au, and the enhanced absorptance appears to be the dominant factor in the

enhanced residual thermal energy deposition in multi-pulse femtosecond laser ablation at large numbers of applied pulses.

[0137] Since different surface modifications are superimposed on each other, it is difficult to completely isolate and determine each individual contribution to the enhanced absorptance. Therefore, we provide the following estimations on the contributions of nano-, micro-, and macro-structures induced by femtosecond laser ablation. Since surface nano-structures are the dominant feature in region AB and part of region BC for $N < 50-100$, and the absorptance increases from 0.12 to 0.25-0.33 over these regions (see FIG. 1), nano-structures alone are believed to account for the additional absorptance increase of about 0.1-0.2. The contribution of two microscale structures, LIPSS and random roughness, is estimated as follows. To estimate the contribution of LIPSS, we ablated a sample using p-polarized light and measured the low-fluence absorptance $A(N)$ of the ablated spot with both p- and s-polarizations. The curves $A(N)$ of different polarizations were identical, indicating that the grating effects of microscale LIPSS on the absorption of laser light by gold is negligible. To estimate the contribution of microscale random roughness, we abraded a mechanically polished sample surface with sandpaper to produce a rms roughness of 3 μm , which is estimated to be comparable to the laser-induced roughness for $100 < N < 1000$. The absorptance of this abraded surface was then measured to be about 0.24 as opposed to 0.12 for a mechanically polished surface. This indirectly shows that the random micro-roughness accounts for the additional absorptance increase of about 0.12. Macro-structures come into play in two major forms, deep central channel and concentric ring grooves, when the number of pulses is between about 500-1000 and laser fluence is higher than 0.17 J/cm^2 . Two SEM pictures showing typical macro-structure craters are presented in FIG. 7. The macro-scale crater formation starts in region CD and, therefore, we believe the progressive increase of macro-structure size largely accounts for the absorptance increase from 0.4 to about 1.0. However, nano- and micro-structures also develop further in regions CD and DE and may also contribute to absorptance increase to some extent.

[0138] Besides the physical mechanisms of enhanced absorption, we also make the following observations about femtosecond laser-matter interactions: First, laser-induced nanostructures alone can enhance the absorptance of Au by a factor of about three following only 1-3 pulses. This result suggests a new direction for future study of optical properties of nanostructures imprinted on a metal surface. Secondly, we produced a new type of microscale periodic structure with much finer nanoscale structures (NC-LIPSS) following ablation with a large number of applied pulses. Thirdly, re-deposition of laser-induced nanoparticles is seen outside of the ablated spot leading to the formation of a nanostructured material known as gold black. Finally, we identified potential new applications of femtosecond laser ablation for modifying optical properties of metals and producing technologically valuable surface coatings such as, but not limited to, gold-black films.

Example 2

[0139] In this Example, a comparative study of residual thermal effects in aluminum following fs laser ablation was performed. At laser fluences above the ablation threshold

where plasmas are produced and at a sufficiently high ambient gas pressure, an enhanced coupling of pulsed laser energy into the sample occurs. Furthermore, in contrast to the conventional understanding that residual thermal energy is negligible in fs-laser ablation, up to 70% of the incident pulse energy can be retained in the sample following single-pulse fs-laser ablation in 1-atm air. The major factors influencing thermal energy coupling to the sample are the laser fluence and ambient gas pressure. Residual thermal energy deposition decreases with reducing ambient gas pressure.

[0140] Laser ablation using femtosecond (fs) laser pulses has numerous applications in the field of materials processing and machining and, nanotechnology. Comparative studies have demonstrated that femtosecond laser ablation has advantages over nanosecond ablation in aspects of higher precision, reduced heat-affected zone, and smaller amount of debris around the ablated spot. Following laser ablation, a fraction of absorbed laser energy is retained in the heat-affected zone, dissipates into the bulk of the sample and remains inside as residual thermal energy that induces the bulk temperature of the sample to rise. This is sometimes referred to as the thermal load and is often undesirable in laser micro- and nano-machining.

[0141] The coupling of thermal energy into metals has been previously studied for microsecond and nanosecond laser ablation. An enhanced residual thermal energy coupling to metals has been observed when laser fluence is above a certain threshold value. It has been suggested that, in addition to the direct absorption of laser light, energy transfer from laser-produced plasma can contribute to residual heating. However, mechanisms responsible for thermal coupling are still not fully understood.

[0142] We have observed an enhanced residual heating of metals following multi-pulse femtosecond laser ablation, where laser-induced surface modification has been found to play a role in enhanced residual heating but, where this alone could not fully account for the observed amount of deposited thermal energy. To exclude the effect of surface modification on residual thermal response, we investigated single-pulse fs ablation. We also studied the residual thermal response of aluminum (Al) following ns-laser ablation to compare with the results for fs-laser ablation. We used a calorimetric technique to study effects of laser pulse duration, ambient gas pressure, and laser wavelength on residual heating of Al. To characterize the residual thermal response, we defined a so-called residual energy coefficient (REC) $K=E_R/E_I$, where E_R is the residual thermal energy remaining in the sample following ablation and E_I is the incident laser pulse energy. By definition, REC is equal to absorptance of the sample material when laser fluence is below the ablation threshold. Enhanced residual heating occurred following both single-pulse ns- and single-pulse fs-laser ablation in ambient gas at a sufficiently high pressure. The major factors governing the residual heating are laser fluence and ambient gas pressure. There is a fundamental difference between multi-pulse versus single-pulse ablation because multi-pulse ablation may induce absorptance change due to accumulated surface modifications from multiple laser shots. This accumulated effect does not occur in single-pulse ablation.

[0143] Both ns and fs duration pulse effects were examined. The following three laser systems were used: 1) a ruby laser producing 45-ns pulses (FWHM) at wavelength $\lambda=0.69 \mu\text{m}$ with pulse energy of 0.6 J; 2) a Nd:YAG laser

generating 55-ns pulses at $\lambda=1.06 \mu\text{m}$ with pulse energy of 1.4 J; and, 3) a Ti:sapphire laser producing 60-fs pulses at $\lambda=0.8 \mu\text{m}$ with pulse energy of 1.5 mJ. Using each laser system, the laser beam was focused onto an Al sample at normal incidence. A fraction of the incident pulse energy E_I was split off using a beamsplitter and measured with a joulemeter to allow E_I to be determined.

[0144] The residual energy E_R that remains in the sample following ablation causes the bulk temperature of the sample to rise by ΔT . Using a thermocouple attached to the Al sample, ΔT was measured after thermal equilibrium was reached in the sample. Knowing the specific heat capacity c_p and the mass m of the sample, the residual energy can be obtained from $E_R=mc_p\Delta T$. The thermocouple response time (the time required for achieving a maximum thermocouple signal in our calorimeter) was about 2.5 sec. Using measured E_I and E_R , the residual thermal energy coefficient $K=E_R/E_I$ can be found as a function of single-pulse laser fluence $F=E_I/S$, where S is the laser beam area on the sample. The samples were mechanically polished. Measurements were performed in various ambient gases and at different pressures. The sample was translated with an X-Y stage so each subsequent laser pulse was incident on a fresh spot. Two parameters, the ablation threshold F_{abl} and the plasma ignition threshold F_{pi} , were determined at the onset of surface damage visible to eye with subsequent examination under a scanning electron microscope (SEM). F_{pi} was determined by observing the onset of bright violet radiation from the irradiated spot using either a photomultiplier (PMT) or an open-shutter camera, both properly filtered to cut off scattered laser light.

[0145] Although embodiments of the invention are directed to fs-duration laser pulses, this Example probes some of the effects of both fs- and ns-duration laser pulses. The dependence of REC on laser fluence F following single-pulse ns-laser ablation in various ambient gases under different pressures on Al are plotted in FIGS. 8 (or Nd:YAG laser) and 9 (or ruby laser). For the Nd:YAG laser, ablation and plasma ignition thresholds in 1-atm air are determined to be $F_{abl}=1.2\pm 0.3 \text{ J/cm}^2$ and $F_{pi}=1.4\pm 0.4 \text{ J/cm}^2$. For the ruby laser, these values are $F_{abl}=1.0\pm 0.2 \text{ J/cm}^2$ and $F_{pi}=1.1\pm 0.3 \text{ J/cm}^2$. Thus $F_{abl}\approx F_{pi}$ in these experiments. By definition, REC should be equal to the absorptance of the material when it is irradiated by low-fluence laser light that does not cause any surface modification. The measured value of REC ($K=0.25$) at $F<F_{abl}$ in FIG. 2 agrees with the reported value of absorptance for a mechanically polished Al sample at $\lambda=1.06 \mu\text{m}$ (D. E. Gray (Ed.): American Institute of Physics Handbook, 3rd edn. (McGraw-Hill, New York, 1972)), and this agreement shows the accuracy of our measurement technique. Data at 1-atm in FIGS. 8 and 9 show that REC enhances abruptly at a certain fluence threshold, F_{enh} , and reaches a maximum value of about 0.5-0.6 indicating that about 50-60% of the laser pulse energy can be retained in Al following nanosecond laser ablation. Our experiment also shows that $F_{enh}\approx F_{pi}$ within the experimental uncertainty for both Nd:YAG and ruby laser ablation.

[0146] Next, we studied the pressure effect on REC; representative curves are plotted in FIGS. 8 and 9. For Nd:YAG laser ablation, REC slightly decreases when air pressure, P , decreases from 1 atm to about 30 torr, but REC abruptly drops when pressure further reduces from 30 torr to about 0.6 torr. For $P<0.6$ torr, the onset of plasma is

accompanied with a drop of REC. This drop becomes more pronounced as the pressure is further reduced to 0.04 torr. At this pressure, REC eventually reaches a value of about 0.12 that is smaller than the absorptance of an undamaged surface by a factor of two. For $P < 0.04$ torr, REC virtually remains independent of the residual air pressure. This behavior shows that, in contrast to the observation in air, the onset of plasma in vacuum is accompanied by a drop of REC. In vacuum, both F_{abl} and F_{pl} are higher than those at 1-atm air pressure by approximately a factor of two. Dependence of REC on laser fluence is also studied in 1-atm oxygen and 1-atm helium, and these REC data are shown in FIGS. 8 and 9. The dependences show virtually the same behavior as those in air, indicating that REC does not essentially depend on the particular type of gas. The contribution of possible exothermic chemical reactions that may occur due to presence of chemically active gases such as oxygen is negligible.

[0147] In vacuum, the laser plasma mainly consists of ionized species of ejected material, while in a gas medium, plasma consists of ionized species of both ablated material and ambient gas. A characteristic feature of ambient gas plasma produced by ns pulses is that the plasma expands due to the generation of laser-supported absorption waves. FIG. 10 shows open-shutter photographs of plasmas produced by 55-ns Nd:YAG laser pulses for ablation of Al in both air and vacuum under the same experimental conditions. Distinction between plasmas can be clearly seen. The size of plasma in air is larger than that in vacuum. Therefore, the role of plasmas in residual heating of the sample in air may differ from that in vacuum.

[0148] The direct absorption of laser energy is a factor that may influence residual heating. According to the Drude model, when the temperature increases material absorptivity should also increase due to an enhanced collision frequency between free electrons and thermally vibrating lattice atoms. Therefore, one should expect an increase in REC with laser fluence due to this enhancement of material absorptivity. However, the fact that REC increases in air while it decreases in vacuum above a certain laser fluence indicates that the temperature-enhanced Drude absorption does not play an essential role in enhanced residual thermal response. This is also confirmed by our estimation of the laser-induced surface temperature using the following formula:

$$T_s(t) = \frac{A\sqrt{a}}{K\sqrt{\pi}} \int_0^t \frac{I(t-\theta)}{\sqrt{\theta}} d\theta + T_0$$

where A is the absorptance, a is the thermal diffusivity, I is the intensity of incident laser light, k is the thermal conductivity, t is the time, T_0 is the initial temperature, and θ is the integration variable. FIG. 11(a) shows the computed $T_s(t)$ induced by the Nd:YAG laser pulse at $F_{abl} \approx F_{pl} = 1.4 \text{ J/cm}^2$ in 1-atm air and at $F_{abl} \approx F_{pl} = 2.7 \text{ J/cm}^2$ in vacuum with $A=0.25$, $a=1.0 \times 10^{-4} \text{ m}^2/\text{s}$, $k=240 \text{ J s}^{-1} \text{ m}^{-1} \text{ }^\circ\text{C}^{-1}$, and $T_0=20^\circ \text{ C}$. One can see that the maximum surface temperature is about 500° C in air and 1000° C in vacuum. The estimated surface temperature in air is below both the melting (660° C) and boiling (2495° C) points of Al. The computed $T_s(t)$ for ruby laser at $F_{abl} \approx F_{pl} = 1.1 \text{ J/cm}^2$ in 1-atm air and at $F_{abl} \approx F_{pl} = 2.1 \text{ J/cm}^2$ in vacuum with $A=0.28$ are shown in FIG. 11(b). Similar to the results of Nd:YAG laser in FIG. 5(a), the estimated surface temperature for ruby laser irradiation in air

is also below both the melting and boiling points of Al. Thus when the enhanced thermal coupling occurs in 1-atm air, the estimated surface temperature induced by both Nd:YAG and ruby lasers is too low to induce a significant increase in absorptance.

[0149] The similar general behavior of REC for Nd:YAG ($\lambda=1.06 \text{ }\mu\text{m}$) and ruby ($\lambda=0.69 \text{ }\mu\text{m}$) lasers shows that laser wavelength is relatively unimportant in the visible and near infrared spectral region. Nevertheless, our experiment clearly demonstrates that REC of the aluminum sample depends mainly on laser fluence and ambient gas pressure following ns-laser ablation.

[0150] The dependence of REC on laser fluence for Al following fs-laser ablation in 1-atm air and in vacuum ($P=0.01$ torr) are plotted in FIG. 12. The residual thermal energy coupling is enhanced in air above a certain threshold value of laser fluence, while in vacuum it is reduced. The values of F_{abl} , F_{pl} , and F_{enh} in air are found to be 0.053 J/cm^2 , 0.086 J/cm^2 , and 0.5 J/cm^2 , respectively. These thresholds are well separated and the enhancement threshold is above the plasma threshold; i.e. $F_{enh} > F_{pl} > F_{abl}$, in contrast to the ns-laser ablation where $F_{enh} \approx F_{pl} \approx F_{abl}$. We note that our measured value of F_{pl} in 1-atm air agrees with reported values for Al thin film deposited on a silicon substrate. The values of F_{abl} and F_{pl} in vacuum are determined to be 0.058 J/cm^2 and 0.096 J/cm^2 , respectively (see FIG. 12). Contrary to conventional understanding that the residual thermal energy is negligible in an ablated sample following femto-second laser ablation, our data show that REC reaches a value of 0.7 indicating that, at the highest laser fluence achievable in our experiment ($F=4 \text{ J/cm}^2$), about 70% of the incident laser energy can be retained in the sample following single-pulse fs-laser ablation in 1-atm air.

[0151] FIG. 13(a) shows an SEM image of an undamaged surface that is mechanically polished. A view of the sample surface after irradiation in air at $F=F_{abl}$ is shown in FIG. 13(b). (FIG. 13(b) does not show the same spot on the sample as in FIG. 13(a)). FIG. 13(b) shows that surface defects are preferential spots for initial ablation with some sparsely distributed small spherical nanoparticles in the irradiated area. FIG. 14 shows a typical laser-induced surface morphology following ablation at $F=F_{pl}$ in 1-atm air. It is seen that surface modifications are still localized around surface defects, but both the number and the size of nanoparticles are greater than those at $F=F_{abl}$. Therefore, material ejection in fs-laser ablation appears to be initiated at surface defects. Open-shutter photographs of the femtosecond laser-induced plumes taken at $F=1.16 \text{ J/cm}^2$ (higher than F_{pl}) are shown in FIG. 15. The figure shows that the size of the plume in air is larger than that in vacuum ($P=0.01$ torr).

[0152] There are three basic distinctions between ns- and fs-laser ablation. First, fs-laser pulses do not interact with ejected material because hydrodynamic expansion of ablated material from the irradiated area occurs on a timescale much longer than femtosecond pulse duration. Secondly, laser-supported absorption waves that are commonly generated in ns-laser ablation in a gas medium do not exist in fs-laser ablation. Thirdly, a material irradiated with an intense fs-laser pulse can be heated to a solid-density plasma state.

Example 3

[0153] Unique properties of nanomaterials have been extensively studied in the past and various nanostructures

have found numerous applications in optics including enhanced x-ray emission and enhanced absorption in intense light-matter interaction, and optical biosensing, to name a few. Direct surface nanostructuring (i.e., not from ablated plume deposition) may be used in a number of technological applications, for example, manipulation of optical properties of solids, catalysts, dental implants, etc. We performed a detailed study of the morphology of surface nanomodifications produced on bulk metals using a femtosecond laser ablation technique embodied herein. The effects of laser fluence and number of applied pulses on the generated surface nanostructures were studied with a scanning electron microscope (SEM). According to an aspect, a set of optimal laser irradiation conditions for metal surface nanostructuring is disclosed.

[0154] In our experiment, we used an amplified Ti:sapphire laser system that consisted of a mode-locked oscillator and a two-stage amplifier including a regenerative amplifier and a two-pass power amplifier. The laser system produces 65-fs pulses with energy around 1 mJ/pulse at a 1 kHz repetition rate with a central wavelength $\lambda=800$ nm. To produce ablation, the laser beam is focused normally onto a bulk sample mounted vertically. To measure the incident pulse energy, a certain fraction of the incident light is split off by a beam splitter and measured with a pyroelectric joulemeter. The number of laser shots, N , applied to the sample is controlled using an electromechanical shutter. All experiments were performed in air under atmospheric pressure. The morphology of femtosecond laser-induced surface modifications was studied using a SEM. The studied samples were mechanically polished copper, gold, and platinum. The range of laser fluence used in the ablation was between 0.084 and 9.6 J/cm². The number of applied pulses was varied from 1 to 5×10^4 shots. The ablation threshold was determined as the minimum fluence to generate a surface damage seen under the SEM.

[0155] A SEM picture of a copper sample surface prior to laser irradiation is shown in FIG. 16(a). For reference, the ablation threshold for a copper sample was determined to be $F_{abl}=0.084$ J/cm² following a total of $N=100$ shots. The morphology of the irradiated surface was studied following ablation with laser fluence of $F=0.084, 0.16, 0.35, 1.52, 3.7,$ and 9.6 J/cm² and the number of applied pulses in the range of $1-5 \times 10^4$. A number of representative surface structures produced on the copper sample are shown in FIGS. 16-18. An analysis of the SEM data shows that the morphology of femtosecond laser-induced surface nanostructures depends both on laser fluence and the number of applied pulses. The effect of the total number of shots on nanostructuring at $F=0.35$ and 1.52 J/cm² is shown in FIGS. 16 and 17, respectively. FIG. 16(b) shows that nanostructures begin to occur on some random localized sites after one shot at $F=0.35$ J/cm². A few larger-size structural features are also observed in the central part of the ablated area, as seen in FIG. 16(b). These larger structures may be associated with surface defects and/or laser beam intensity inhomogeneities. FIG. 16(c) shows a nanoscale surface structure produced by two-shot ablation. The structure comprises both larger nanocavities and nanoprotusions with spherical tips of diameter up to about 75 nm. Therefore, the one additional shot transforms the sparsely distributed nanoscale features in FIG. 16(b) to the cellular-like structures in FIG. 16(c). The surface morphology after ablation with 1000 pulses is shown in FIG. 16(d). One can see that the mean size of nanopro-

trusions becomes larger while at the same time some nanocavities develop into microcavities. The evolution of the surface structures following ablation at $F=1.52$ J/cm² and various N is shown in FIG. 17(a-d). At this middle fluence, pure nanostructures are only generated by ablation with one or two laser shots (FIGS. 17(a) and 17(b)). As shown in FIG. 17(c), 10 shot ablation produces both random nano- and micro-structures. With further increasing N , the proportion of nanostructures decreases as can be seen in FIG. 17(d), where microscale structures become dominant. At the highest fluence used in our experiment, nanostructures are not present over most of the irradiated area and a dominant morphological feature is microroughness. However, nanostructuring can still be observed on the periphery of the ablated spot where the Gaussian beam intensity is low enough for nanostructural formation. An example of these surface structural modifications is shown in FIG. 18 for two-shot ablation at $F=9.6$ J/cm².

[0156] The effect of laser fluence on surface structuring can be seen from analyzing the surface modifications produced at various F and fixed N as shown for example in FIG. 16(c) ($F=0.35$ J/cm², $N=2$), FIG. 17(b) ($F=1.52$ J/cm², $N=2$) and FIG. 18 ($F=9.6$ J/cm², $N=2$). These images show that ablation with high laser fluence does not actually induce nanostructures and therefore there exist optimal laser ablation conditions for surface nanostructuring. In order to determine the optimal conditions for nanostructuring, we performed an SEM study of laser-induced surface modifications following ablation with a large variety of F and N . The obtained data are summarized in FIG. 19. One can see that the most favorable conditions for pure nanostructuring are ablation at low and medium values of laser fluence ($F < 1.5$ J/cm²). FIG. 19 also shows the range of laser irradiation parameters where femtosecond laser ablation produces different combinations of surface nano-, micro-, and macro-structures.

[0157] To determine the mechanism of nanostructuring, we performed a SEM study on the origin of nanoscale modifications. A representative example of nascent nanostructures following ablation with $F=0.35$ J/cm² and $N=1$ is shown in FIG. 20(b), where the characteristic types of initial nanostructures are labeled. For comparison, FIG. 20(a) shows an undamaged area of the sample using the same scale as in FIG. 20(b). It is seen in FIG. 20(b) that surface structuring is initiated on random, highly-localized nanoscale sites. The typical structures include circular nanopores with a diameter in the range of 40-100 nm, randomly-oriented nanoprotusions with a diameter in the range of 20-70 nm and a length of 20-80 nm, nanocavities of arbitrary form, and nanorims around nanocavities. Under these femtosecond laser processing conditions, nanoscale features down to a size of 20 nm are produced. One can see from FIG. 20(b) that a nanopore or nanocavity is always immediately accompanied by a nanorim or nanoprotusion, indicating a nanoscale material relocation to an adjacent site. These one-to-one nanoscale dips and protusions occur randomly over the laser spot, suggesting an initial non-uniform laser energy deposition. Possible factors responsible for the spatial variation of the absorbed laser energy include: (1) the spatial inhomogeneity of the incident beam; (2) the enhancement of absorption by surface defects; (3) interference of the incident laser light with the excited surface electromagnetic waves due to structural defects. When the incident laser fluence is close to the laser ablation

threshold, the spatial variations in deposited laser energy can produce a melt at localized nanoscale sites within the irradiated spot. Once the localized nanoscale melts have been formed, a high radial temperature gradient in a nanomelt can induce a radial surface tension gradient that expels the liquid to the periphery of the nanomelt. This will lead to the formation of nanocavities, nanoprotusions, and nanorims due to fast freezing of the expelled liquid on the boundary with the solid state material (see FIG. 20(b)). This mechanism may also be used to explain the formation of nanobumps on a thin metal film. These initially induced surface random nanostructures can enhance the absorption of laser light and facilitate the further growth of surface nanoroughness due to the increased spatial non-uniform energy absorption.

[0158] When laser fluence is sufficiently high to produce ablation, the atoms ejected from the nanomelts produce a recoil pressure that squirts liquid metal outside of the nanomelt. For multi-pulse ablation, the repeating vaporization and re-deposition of nanoparticles back onto the surface may also affect the surface nanostructuring. SEM morphology study at high fluence ($F > 5 \text{ J/cm}^2$; i.e., strong ablation) shows that melt occurs over a large area of the ablated spot (see FIG. 18) and the flow dynamics in this large melt pool predominantly results in microstructuring. We have also studied the ambient gas pressure effect on nanostructuring by taking SEM images of platinum following single-pulse ablation in 1-atm air and in a vacuum at a base pressure of 8×10^{-3} Torr. Although we have observed a greater amount of re-deposited nanoparticles in air than in vacuum, the morphology of nanostructures is still quite similar under different air pressures. Our study was performed with samples mounted vertically. It should be noted that the amount of re-deposited ablated particles back onto the sample surface may be different when the sample is positioned vertically versus horizontally, but further studies are required in this aspect of nanostructuring using fs laser pulses.

Example 4

[0159] Laser-induced periodic surface structures (LIPSS) on solids have been studied in a number of works in the past. Typically, LIPSS show regular groove structure with a period on the incident laser wavelength scale and oriented perpendicularly to the polarization of the incident light. LIPSS are commonly seen following long pulse irradiation on a variety of materials, including semiconductors, metals, and dielectrics.

[0160] In contrast to previous work performed mostly at relatively high fluence, we studied the formation of LIPSS on platinum and gold in a special fluence regime, namely, at near damage-threshold fluence. We found a unique type of LIPSS entirely covered with nanostructures. A distinctive feature of the nanostructure-covered LIPSS (NC-LIPSS) is that its period is appreciably less than that of the regular LIPSS whose period is approximately equal to the laser wavelength at normal incident laser light. The reduced period of the nanostructure-covered LIPSS is caused by a significant increase of the real part of the effective refractive index of the air-metal interface when nanostructures develop on a metal surface that affects the propagation of excited surface plasmon polaritons. Nanostructure-covered LIPSS has a variety of potential applications, such as modifying optical properties of materials and chemical catalysts where high surface-to-volume ratio is a crucial factor.

[0161] In this experiment, we used an amplified Ti:sapphire laser system that generates 65-fs laser pulses with energy about 1 mJ/pulse at a 1 kHz repetition rate and with a central wavelength $\lambda = 0.8 \mu\text{m}$. The horizontally-polarized laser beam is focused onto a vertically standing metal sample in air at normal incidence. The number of laser shots, N , applied to the sample is selected with an electromechanical shutter. We studied the evolution of NC-LIPSS on metals following irradiation with $N = 1, 2, 4, 8, 10, 20, 30, 40, 50, 100, 200, 300, 400, 500$ pulses at near damage-threshold fluence. The studied metals were platinum and gold. The laser fluence of the incident light was varied by changing the distance between the focusing lens and sample. To measure the laser pulse energy incident upon the sample, a fraction of the incident laser beam is split off by a beamsplitter and diverted to a pyroelectric joulemeter. The morphology of the produced periodic structures is examined using a scanning electron microscope (SEM). The surface profile is measured with an atomic force microscope (AFM). All sample surfaces were mechanically polished using 0.1 μm grade aluminum oxide powder.

[0162] The evolution of surface structures produced on Pt following ablation at near damage-threshold laser fluence of $F = 0.16 \text{ J/cm}^2$ is shown in FIGS. 21(a)-(b). FIG. 21(a) demonstrates surface random nanoroughness produced after 10 shot ablation. The inset in FIG. 21(a) shows that this initial surface modification is characterized by nanocavities and nanoprotusions of various forms. At $N = 20$, a microscale periodic pattern starts to form over the initially produced random nanoroughness. At this stage, only small patches of periodical structures are observed in various isolated locations within the irradiated spot, referred to below as intermediate LIPSS. With increasing N , the intermediate LIPSS grow and coalesce into a clear extended LIPSS with a period of 0.61 μm at $N = 30$ (FIG. 21(b)). For N greater than 70 shots, LIPSS starts to disappear gradually in the central spot area (FIGS. 22(a) and 22(b)). However, clear NC-LIPSS continue to form in the peripheral area (FIGS. 22(c) and 22(d)). Using AFM, the initial undamaged surface rms roughness is found to be about 5.6 nm after polishing, and a typical AFM surface profile measurement on Pt is shown in FIG. 23(a). Following ablation with $N = 1, 2$, and 10 shots, surface rms roughness is found to be about 16.5, 35.2, and 79.8 nm, respectively. FIG. 23(b) shows typical surface roughness after $N = 10$ shots. The surface profile of LIPSS after 30 laser shots is shown in FIG. 24. To gain the insight of how initial nanoroughness affects the formation of NC-LIPSS, we performed a SEM study of the formation of NC-LIPSS with samples of different initial surface conditions. We found that the extended LIPSS is produced with a smaller number of laser shots when the sample has a greater surface nanoroughness. To understand the material dependency in forming the nanostructure-covered LIPSS, we also performed a detailed SEM study of surface structural modifications on Au. Our data show that the general trend is similar for Au and Pt in forming the initial nanoroughness. The period of nanostructure-covered LIPSS on Au is observed to be 0.58 μm and is also markedly less than the laser wavelength (FIG. 25). However, the periodic patterns on Au are much less clear compared to Pt. Recently, we performed a comparison study on regular LIPSS on various metals following femtosecond laser radiation where LIPSS shows distinctly different level of morphological clearness among various metals even under identical experimental

conditions. The electron-phonon energy coupling coefficient, g , is shown to directly correlate to the morphological clearness of LIPSS. A larger g coefficient usually leads to more pronounced LIPSS. In this study, g coefficient for Pt and Au are 25×10^{16} and 2.1×10^{16} W/m³K, respectively, and the much larger g coefficient explains why LIPSS is much more clear on Pt than Au.

[0163] The periodic patterns induced by femtosecond laser processing are distinctly different from those produced by longer pulses in two aspects. First, femtosecond laser-induced periodic structures are covered by random nanostructures. Secondly, the LIPSS period induced by femtosecond pulses at normal incidence is appreciably less than the laser wavelength while the period is roughly equal to the wavelength for longer pulses. To account for our observation, we carefully examined the evolution of surface structural modifications on both Pt and Au, and we propose the following mechanism for the formation of NC-LIPSS. The first few laser shots usually produce sparsely and randomly distributed nanostructures. It is known that surface plasmons, both localized and propagating along a surface, can be excited by coupling laser energy into nanostructures. With further increase of the number of laser shots, more nanostructures appear allowing excitation of more localized and propagating surface plasmons. The produced nanoroughness includes nanorods, nanocones, and nanospheres, and these nanostructures will excite propagating cylindrical surface plasmons that subsequently interfere with the incident light. This interference causes the formation of intermediate periodic surface microstructures. As the number of laser shots increases, the intermediate microstructures will grow as well as the area occupied by these structures. The developed intermediate periodic surface microstructures will further excite propagating plane surface plasmons that interfere with the plane incident laser light wave, and this interference will finally result in the permanent extended periodic microstructures.

[0164] For normally incident linearly polarized light, the period d of the surface grating formed due to the interference between the incident laser light and the excited surface plasmon wave is given by equation 1 as:

$$d = \lambda \eta \quad (1)$$

with $g \parallel E$, where λ is the incident light wavelength, $\eta = \text{Re}[\epsilon/(\epsilon+1)]^{1/2}$ is the real part of the effective refractive index of the air-metal interface for surface plasmons, ϵ is the dielectric constant of the metal, g is the grating vector, and E is the electrical field vector of the incident wave. For a plane vacuum-metal interface, η is calculated to be 1.0096 at $\lambda=800$ nm for Pt ($\epsilon_1=-15.5$ and $\epsilon_2=23.5$) and 1.022 for Au ($\epsilon_1=-23.4$, $\epsilon_2=1.55$). Using Eq. (1), the grating period is found to be 0.79 μm for Pt and 0.78 μm for Au. However, the observed period is 0.61 μm for Pt (FIG. 1(b)) and 0.58 μm for Au (FIG. 5). If we substitute these values of the observed period into Eq. (1), we will have $\eta=1.31$ for Pt and $\eta=1.38$ for Au. To explain this discrepancy, we note that the table values of ϵ_1 and ϵ_2 for Pt and Au are obtained from smooth surface and at room temperature, and therefore these values may not be suitable when the metals are heated by high-intensity femtosecond pulses and covered with nano- and micro-structures. To better understand the high-intensity effects on NC-LIPSS period, we performed a detailed study of LIPSS in various locations within the damaged spots on metals. From these data summarized in Table 1, we can see

that the NC-LIPSS period remains the same in the central and peripheral areas of an irradiated spot despite the fact that the two locations have different intensities due to the Gaussian beam profile. On the other hand, the period of our NC-LIPSS decreases with increasing N when the surface roughness grows while the light intensity remains constant. Furthermore, the NC-LIPSS produced using a higher fluence of 0.16 J/cm² exhibit a similar period as that produced at $F=0.084$ J/cm². Our observations indicate that the high-intensity effect on dielectric constant is not essential, whereas the effects of surface morphology (nano- and micro-roughness) are more dominant. It is known that surface roughness causes an increase in the modulus of the surface plasmon wave vector, and this will correspond to an increase in the real part of the refractive index. According to Eq. (1), an increased real part of the refractive index for propagating surface plasmons will cause a reduced NC-LIPSS period, which agrees with our experimental observation.

TABLE 1

Nanostructure-covered LIPSS period in different areas of the irradiated spot on platinum at $F = 0.084$ J/cm ² .		
LIPSS period (μm)		
Number of shots	Central area	Peripheral area
30	0.62	0.61
50	0.58	0.61
100	0.57	0.57
200	0.55	0.54
500	0.55	0.53

[0165] Under certain conditions we also produced a large number of nanoprotusions and nanocavities on a metal surface (see FIG. 22). The nanostructures produced can greatly increase the effective surface area, which may be of importance in many technological applications, such as but not limited to producing better chemical catalysts where a high surface-to-volume ratio is a crucial factor.

Example 5

[0166] In this study we performed a femtosecond laser surface treatment of titanium to help determine the potential of this technology for surface structuring of titanium implants. We found that femtosecond laser processing produces a large variety of nanostructures (nanopores, nanoprotusions) with a size down to 20 nm, multiple parallel grooved surface patterns with a period on the sub-micron level, microroughness in the range of 1-15 μm with various configurations, smooth surface with smooth micro-inhomogeneities, and smooth surface with sphere-like nanostructures down to 10 nm. Also, we have determined the optimal conditions for producing these surface structural modifications. Femtosecond laser treatment may produce a richer variety of surface structures on titanium for implants and other biomedical applications than long-pulse laser treatments.

[0167] Due to good biostability, biocompatibility, mechanical performance, and long-term durability, titanium has been widely used in a variety of biomedical applications such as dental and orthopedic implants, and implantable electronic devices. In numerous in vitro and in vivo studies, surface topography of titanium implants has been shown to be important in enhancing implant performance. It has been

shown that both microstructures and nanostructures influence biological processes at implant interfaces. Various methods of implant surface structuring have been studied in the past such as grit-blasting, chemical etching, laser treatment, and the combinations of the various methods. Recent studies have shown that laser processing of implant surfaces provides both suitable surface topography and less surface contamination as compared with other methods. Another advantage of laser processing is that the technique is also suitable for texturing of more complicated shapes. In the past, surface structures have been produced using long-pulse lasers, including nanosecond Nd:YAG laser, copper vapor laser, nanosecond excimer lasers, picosecond Nd:YAG laser, and sub-picosecond excimer laser. Femtosecond lasers have advantages over nanosecond lasers in aspects of higher precision, reduced heat-affected zone, and smaller amount of debris around the ablated spot.

[0168] The effects of laser fluence and the number of applied pulses on laser-induced surface topography in titanium are reported herein. We found that a femtosecond laser produces a large variety of nanostructures (nanopores, nanoprotusions) with a size down to 20 nm, multiple parallel grooved surface patterns with a period on the sub-micron level, microroughness in the range of 1-15 μm with various configurations, smooth surface with smooth micro-inhomogeneities, and smooth surface with sphere-like nanostructures down to 10 nm. Our results suggest that femtosecond laser treatment can produce a richer variety of surface structures on titanium for implants and other biomedical applications than long-pulse laser treatments.

[0169] Commercially pure titanium flat plates with a dimension of $15 \times 17 \times 1.5$ mm were used in our experiment. The plates were mechanically polished using 0.1- μm -grade aluminum oxide powder and further cleaned with acetone. For surface texturing, we used an amplified Ti:sapphire laser system that generates 65-fs laser pulses with the pulse energy over 1 mJ at a 1 kHz repetition rate with a central wavelength of 0.8 μm . The laser beam is horizontally polarized and was focused at normal incidence onto a vertically standing titanium sample in air at a pressure of 1 atm. For laser beam focusing, we used an achromatic lens with a focal length of 20 cm. The laser fluence of the incident light was varied by changing the distance between the focusing lens and the sample. The diameter of laser-irradiated spots on the titanium sample was varied from 100 to 1200 μm . The number of laser shots, N, applied to the sample was selected with an electromechanical shutter. The surface structuring of titanium was studied following the treatment with laser fluence of $F=0.067, 0.084, 0.16, 0.35, 0.48,$ and 2.9 J/cm^2 and the number of applied pulses, N, in the range of 1-30,000. Following femtosecond laser treatment, the topography of surface modifications was studied using a SEM.

[0170] As a reference, FIG. 26(a) shows a SEM image of the titanium surface prior to laser irradiation. FIGS. 26(b) through 26(d) demonstrate surface topography produced by femtosecond laser processing at near-damage-threshold fluence of $F=0.067 \text{ J/cm}^2$ for different numbers of laser shots, where the characteristic features are random nanopores and sphere-like nanoprotusions with the size down to about 15-20 nm. Laser-induced surface nano-topography depends on both the number of applied pulses and laser fluence. At higher fluence of $F=0.084 \text{ J/cm}^2$, the nanoroughness produced is shown in FIGS. 27(a) through 27(d), where the

average size of the nanostructures at this higher fluence is larger than those at lower fluence in FIG. 1. For $N>10-15$, periodic ordering of surface nanoroughness begins to occur. FIGS. 28 and 29 show some typical periodic patterns for laser fluences $F=0.067$ and 0.084 J/cm^2 , respectively. The period of the grooves is about 0.53 μm . These periodic patterns with sub-micron periods are covered with nanoroughness, as shown in detail in FIGS. 28(d) and 29(d). With increasing laser fluence, the periodic patterns are less likely produced and microroughness becomes a more dominant surface structure. FIG. 30 shows surface topography produced following treatment at $F=0.16 \text{ J/cm}^2$ at various N. At this middle-level laser fluence, pure nanoroughness is observed only after one-shot laser processing (FIG. 30(a)). A clear microscale roughness covered with nanoroughness develops after 20-shot treatment (FIG. 30(b)). With further increasing N, microroughness continues to develop with deepening of cavities (FIG. 30(c)). At a large enough N, columnar surface micro-structures covered with nanoroughness are seen in FIG. 30(d). At higher laser fluence of $F=0.35 \text{ J/cm}^2$, a combination of nano- and micro-structures is produced after only one laser shot, as shown in FIG. 31(a). With increasing N, columnar microstructures rapidly develop as the dominating structures (see FIGS. 31(b)-31(d)). When the laser fluence is increased to the level of $F=0.48 \text{ J/cm}^2$, a different type of surface microstructures is observed, as shown in FIGS. 32(a)-32(c). At this laser fluence and for $N>1000$, a pore of the size of the focused laser beam can be created. An example of such a pore with the diameter of 350 μm is shown in FIG. 32(d), where microstructures are also seen at bottom of the pore. At the highest fluence used in our experiment, $F=2.9 \text{ J/cm}^2$, one laser shot can produce surface melting over the entire irradiated surface area, and resolidification of this surface melt results in a smooth surface covered with some micro-inhomogeneities as shown in FIG. 33(a). Following two-pulse irradiation, an even smoother surface is seen in FIG. 33(b). A magnified picture showing nanoscale features of such smooth surfaces is shown in FIG. 33(c). A detail picture of the titanium surface after four laser shots is shown in FIG. 33(d), where one can see nanoscale structures as small as down to 10 nm. The smooth surface is produced with a low number of laser shots ($N<10$). At a larger $N(N>10)$, micro-inhomogeneities develop rapidly and eventually a crater of the size of the focused laser beam will be formed.

[0171] It has been shown that implant surface topography is an important factor affecting the behaviors of both proteins and cells on implant surfaces. It is generally accepted that proteins typically respond to surface structural features (pits, pillars, steps) about 1-10 nm, while cells can be sensitive to structural features on the scale of 15 nm-100 μm . It was also found that structured implants have a better mechanical interlocking of the bone-implant interfaces than smooth implant surfaces due to an increased surface area. Also, it has been reported that extended parallel groove structures may cause cells to align and migrate along the grooves, a contact guidance phenomenon. Our SEM study shows that all of these types of surface textures can be produced by femtosecond laser treatment.

[0172] Little work has been done on laser fabrication of surface nanostructures on titanium. Our study shows that femtosecond laser technique can produce a large variety of both pure nanostructures (FIGS. 26(b)-26(d), 27(a)-27(d), and 33(c)) and various combinations of micro- and nano-

structures (FIGS. 28(d), 29(d), 30, 31). There are two types of pure nanostructures observed in our experiment. The first type (FIGS. 26(b)-26(d), 27(a)-27(d)) is produced at low laser fluence (near the damage threshold) and a low number of laser shots; the size of these nanostructures is down to 20 nm. The second type (FIGS. 33(c) and 33(d)) is produced at high fluence and low N when laser irradiation causes the surface to melt uniformly over the entire irradiated area; the size of these nanostructures is down to 10 nm.

[0173] Examination of shot-to-shot SEM images of surface topography suggests the following mechanism for the formation of nanostructures of the first type. It is seen from FIG. 26(d) that a nanopore is always accompanied by a nearby nanoprotusion, indicating a nanoscale material relocation to an adjacent site. This one-to-one nanoscale pores/protusions relationship occurs randomly over the laser spot, suggesting an initial non-uniform laser energy deposition. When the incident laser fluence is close to the laser damage threshold, spatial non-uniformity in the deposited laser energy can produce a melt at localized nanoscale sites within the irradiated spot. Once the localized nanoscale melt has been formed, a high radial temperature gradient in a nanomelt can induce a radial surface tension gradient that expels the liquid to the periphery of the nanomelt. This can lead to the formation of nanocavities and nanoprotusions due to fast freezing of the expelled liquid on the boundary with the solid state material. These initially induced surface random nanostructures enhance the absorption of laser light and facilitate further growth of surface nanoroughness with increasing number of laser shots due to the increased spatial non-uniform energy absorption. When laser fluence is sufficiently high to produce ablation, particles will be ejected from the nanomelts and produce a recoil pressure that squirts the liquid metal outside of the nanomelt. It should be noted that for multi-pulse ablation, the repeating vaporization and re-deposition of nanoparticles back onto the surface can also promote surface nanostructuring. As seen from FIGS. 26 and 27, the average size and density of femtosecond laser-induced nanostructural features can be controlled by varying both the laser fluence and number of laser shots.

[0174] Mechanisms for the formation of nanostructures of the second type cannot be straightforwardly derived from our SEM study. The formation of these nanostructural features may be due to redeposition of ablated nanoparticles back onto the irradiated surface.

[0175] Multiple parallel grooved surface patterns for biomedical applications are commonly produced using lithographic or laser holographic techniques. However, fabrication of these type of patterns on biomaterials using a single laser beam has not been reported. Below we discuss the optimal conditions for producing these structures and explain the physical mechanisms of their formation.

[0176] Our study shows that optimal conditions for producing periodic groove patterns on titanium are at near-damage-threshold fluence and with the laser shot number in the range between 20 and 800. In the past, multiple parallel grooved surface patterns have been produced by long-pulse lasers and are known as laser-induced periodic surface structures (LIPSS). The formation of LIPSS on metals is believed to result from the interference of the incident laser light with the excited surface plasmon polaritons that result in spatial periodic energy distribution on the surface. Usually, LIPSS shows a regular groove structure with a period on the incident laser wavelength scale and is oriented

perpendicularly to the polarization of the incident light. Our results of the evolution of surface structural modifications on titanium suggest the following mechanism for the formation of the observed LIPSS. In our experiment, the first few laser shots produce sparsely and randomly distributed nanostructures. It is known that propagating cylindrical surface plasmons can be excited by coupling laser energy into nanoroughness, and this can give rise to their interference with the incident light. This interference will, first, cause the formation of intermediate periodic surface structures in localized areas of the irradiated spot. An example of such intermediate periodic surface structure can be seen in FIG. 26(c). With further increasing number of laser shots, the number of intermediate periodic structures will grow as well as the area occupied by these structures. The developed intermediate periodic surface structures will further excite propagating plane surface plasmons and their interference with the plane incident laser light wave will, finally, result in the permanent extended periodic grating.

[0177] For linearly polarized incident laser light, the period d of the surface grating formed due to the interference between the incident laser light wave and the excited surface plasmon wave is given by $d = \lambda / (\eta \pm \sin \theta)$ with $g \parallel E$, where in this equation λ is the incident light wavelength, $\eta = \text{Re}[\epsilon / (\epsilon + 1)]^{1/2}$ is the real part of the effective refractive index of the air-metal interface for surface plasmons, ϵ is the dielectric constant of the metal, θ is the laser light incidence angle, g is the grating vector, and E is the electrical field vector of the incident wave. The above equation shows that the period of laser-fabricated grating can be varied by changing the laser wavelength, the incidence angle, or the real part of the effective refractive index. An important parameter affecting the cell behavior is known to be groove depth, and this parameter in fabricating LIPSS can be controlled by the number of applied laser shots.

[0178] A unique feature of the periodic groove structures produced according to the embodiments herein is that both ridges and grooves are covered with nanoroughness following femtosecond laser treatment, in contrast to rectangular surface grooves fabricated using lithography techniques that usually have smooth ridges and rough floors.

[0179] Laser microtexturing of titanium has been studied in the past using long-pulse lasers. It has been shown that laser processing of implant surfaces provides both suitable surface microstructures and the least surface contamination as compared with other methods. As shown in FIGS. 30(b)-30(d), 31(a)-31(d), 32(a)-32(c), and 33(a), a rich variety of microstructures can be produced by femtosecond laser treatment, and these structures can be characterized as the following two types. The first type (see FIGS. 30(b)-30(d), 31(a)-31(d), 32(a)-32(c)) is produced at the middle levels of the laser fluence ($F=0.16$ and 0.35 J/cm^2). The characteristic size of this type of microroughness is in the range of 1-15 μm . Both the characteristic size and configuration of the surface microroughness can be controlled by both laser fluence and the number of applied shots. This type of microroughness seems to be only produced by femtosecond laser treatment. The second type of microroughness (see FIG. 33(a)) is characterized by a smooth surface with smooth micro-inhomogeneities. This type of microroughness is produced at the highest laser fluence in our experiment ($F=2.9 \text{ J/cm}^2$) when melting occurs over the entire irradiated area. If the melted surface has some structural

inhomogeneities, fast resolidification of this melted surface may result in smooth micro-scale roughness.

[0180] Some parts of implant surfaces may be required to be smooth. Previously, nanosecond excimer lasers have been used for polishing machined titanium implants, and effects of both polishing and cleaning of the surfaces have been reported). Our study shows that smoothed surface can be also obtained with femtosecond laser treatment, as shown in FIG. 33(b).

[0181] It is known that open pores with a diameter in the range of 100-400 μm can improve the strength of bone-implant interfaces. Recently, long-pulse lasers have been used for fabricating 100-300 μm pores on Ti6Al4V implants. Our study shows that pores of this size can be produced with femtosecond laser treatment, as shown in FIG. 32(d). We note that we can further produce various surface structures on the pore bottom through femtosecond laser treatment.

Example 6

[0182] Another application of femtosecond laser surface structuring to produce the materials processing of the presently embodied invention is to provide the controllable modification of the optical properties of metals, where these optical properties range from the UV to THz spectral range, and where the modifications may be used to create various black, grayed, and colored metals.

[0183] As an example, FIG. 34 shows the % reflectance from 0.25 to 2.5 μm of "black" aluminum obtained by the materials processing methods of the present invention. In the visible this aluminum appears pitch black as illustrated in FIG. 35(a).

[0184] By varying the materials processing parameters, we have also produced aluminum that appears to be various shades of gray. Thus in the case of the grayed aluminum as shown in FIG. 35(b), the materials processing was performed at laser fluence $F=7.9 \text{ J/cm}^2$, a scanning speed of the laser beam across the surface of the Al of $v=1 \text{ mm/s}$, and translation between scanning lines $S=100 \mu\text{m}$. The two gray shades of aluminum shown in FIG. 35(b) are obtained by varying the laser pulse repetition rate ($f=100 \text{ Hz}$ for the darker shade and 93 Hz for the lighter one). The spectral reflectance of this darker gray aluminum sample is shown in FIG. 34.

[0185] In addition to producing various shades of gray as discussed above, the materials processing methods of the present invention can also produce colored metals; i.e., metals that appear to have a particular color or that appear to have multiple colors.

[0186] To produce colored metals, two types of femtosecond laser processing techniques were performed. The first technique involved tailoring laser-induced surface random structures, while the second technique produced femtosecond laser-induced periodic surface structures (FLIPSS). The colored metals produced by the first technique exhibit the same apparent color at various viewing angles, while the colored metals produced by the second technique exhibit different colors at different viewing angles due to a grating effect.

[0187] FIG. 35(c) shows a picture of a colored aluminum sample produced by the controlled tailoring of random surface roughness. The aluminum appears golden in color because the tailored surface structures preferentially

enhance the absorption at blue and green wavelengths. The spectral reflectance of the golden aluminum is shown in FIG. 34.

[0188] Colored metals produced by the second technique, FLIPSS, exhibit different colors at different viewing angles. FIG. 36 shows various colors of an aluminum sample structured with FLIPSS under experimental conditions of $F=0.05 \text{ J/cm}^2$, $f=83 \text{ Hz}$, $v=1 \text{ mm/s}$, and $S=100 \mu\text{m}$. The spectral reflectance of the color aluminum structured with FLIPSS is shown in FIG. 34. Structuring with FLIPSS can cause a polarization effect on the absorption of light that provides an additional way for controlling the optical properties. The size of the optically modified metal surface area can be as small as a tightly focused laser spot; i.e. down to about 10 μm , or as large as desired by using a scanning laser beam (for example, FIGS. 35 and 36 show samples with structurally modified area of about 24 mm in diameter).

[0189] Given the additional advantages of laser processing such as low contamination and capability to process complicated shapes, the black, grayed, and colored metals created by femtosecond laser surface structuring have numerous potential applications in such areas including, but not limited to, photonics, plasmonics, optoelectronics, stealth technology, thermal radiation sources, solar cell absorbers, radiative heat transfer devices, infrared sensing, bio-optical devices, thermophotovoltaics, and airborne/space borne devices.

Superwicking and Superwetting

[0190] Wetting properties of a solid surface are characterized by the contact angle of a water/liquid drop deposited on the horizontal surface of the solid as shown in FIG. 37. The surface can be smooth or structured. A surface is called hydrophilic when it exhibits the water contact angle smaller than 90 degrees. The smaller the contact angle, the better the wetting. A surface is commonly referred to as superhydrophilic (or superwetting) when the water/liquid spreads to zero or nearly a zero contact angle. When a smooth surface is originally hydrophilic, any surface structure produced on the surface will enhance the hydrophilicity (wettability).

[0191] 'Wicking' means that the surface has capillary properties. In non-limiting, illustrative aspects of the invention, capillary properties are due to microgrooves engineered into the surface of the material. The capillary effect in a pipe is well known. However, when the pipe is cut along its axis into a half-pipe, the capillary effect will occur as well, albeit to a much lesser extent than in the full pipe.

[0192] Strictly speaking, most any material surface structure has capillary properties because most any structure can be viewed as a two-dimensional network of micro- or nano-channels. However, most surface structures exhibit negligible capillary effect unless they are specifically engineered to do so. Therefore both smooth and structured surfaces can be superwetting/superhydrophilic with a water contact angle close to zero; however, they will not have capillary properties and are not capable of wicking. To make the surface wicking, we produce engineered surface structures that are capable of generating strong capillary forces. Non-limiting, exemplary engineered surface structures are an array of parallel microgrooves that can be reduced to a single channel if necessitated by a particular design application. Similar to non-wicking surfaces, the water/liquid

contact angle on wicking surfaces also can be zero or close to zero, and we can say that they are superhydrophilic/superwetting.

[0193] The femtosecond laser-produced microgrooves disclosed herein generate strong capillary action that enables water, for example, to run vertically (against gravity) uphill. This degree of capillary effect in pipes and grooves is observed when the material is hydrophilic. The surface of the embodied microgrooves is covered with a hierarchical surface structure composed of fine microroughness in the form of protrusions, cavities, spheres, rods, and/or other irregularly shaped features having heights and/or widths on the order of 0.5 to 100 microns, and nanoroughness in the form of protrusions, cavities, spheres, rods, grooves, and/or other irregularly shaped features having heights and/or widths on the order of 1 to 500 nanometers. As mentioned above, most any surface structure on an originally hydrophilic surface will enhance the original hydrophilicity. The novel hierarchical surface structure that covers the surface of the embodied engineered microgrooves significantly enhances the hydrophilicity of the microgroove surface and, this hierarchical surface structure makes the microgroove surface superhydrophilic/superwetting since the values of the water contact angle, θ , are close to or substantially zero degrees. The capillary force is proportional to $\cos \theta$; therefore, when $\theta \approx 0$, the capillary effect achieves a maximum effect under the same other conditions.

[0194] Similarly for the other embodiments disclosed herein, the laser parameters for controlling the formation of appropriate surface structures include laser fluence, number of laser shots N , focused spot diameter, scanning speed, pulse repetition rate, scanning step, laser light polarization, incidence angle of the laser beam, laser pulse duration, spatial intensity profile, wavelength, kind and pressure of ambient medium. To produce any surface structure, laser fluence must exceed the material's ablation threshold. Thus as one skilled in the art will appreciate, the range of laser fluence is any value of laser fluence above the particular ablation threshold. The range of number of laser shots (which may be overlapped), N is $N \geq 1$. The focused laser spot diameter determines the width of the microgrooves. Typically, the smallest laser spot diameter is about 3-5 μm ; however, using tightly focused spots (3-5 μm) having a Gaussian spatial intensity profile, 100 nm diameter holes can be produced at ablation threshold fluence. Scanning the sample across the laser beam can then produce nanogrooves having widths down to about 100 nm. Since increasing the laser spot diameter leads to decreasing the laser fluence, the upper limit on the laser spot diameter is governed by the value of laser ablation threshold laser fluence. However, this is not limiting for producing wider grooves. For example, we can produce a 1 mm-width groove using 100 μm -diameter spots using overlapped scan lines. Other parameters can be tuned for achieving strong capillary action depending on material being processed.

[0195] Arrays of parallel microgrooves (one-dimensional grating) in the material's surface provided unidirectional spreading of liquid. Two-dimensional gratings exhibited uniform two-dimensional spreading of the liquid. Although experiments were performed with straight grooves, curvilinear or other shaped groove forms are expected to be equally as effective.

[0196] The embodied femtosecond processing methods for creating superwicking and superwetting materials are or

appear to be suitable for metals, semiconductors, dielectrics (glasses), polymers, enamels, hard biological tissues (teeth, bones, etc.) and other materials containing hydroxyapatite.

[0197] Wetting properties of solids can be also modified through surface chemistry. For example, a silicon structured surface becomes superhydrophobic after coating with a monolayer of dimethyldichlorosilane $[(\text{CH}_3)_2\text{SiCl}_2]$ reagent. Therefore, the embodied technique for producing wicking surfaces can be supplemented with chemical treatment for further improving the superwicking and superwetting performance of appropriate materials.

[0198] The production of the fine microstructures described hereinabove may be made or controlled by a variety of method modifications; that is to say, once a material has been selected and the general ablation parameters have been determined, alterations of or in the material's surface can be performed in a variety of ways. For example, a desired indentation in the material in the form of a crater may be made at time t_1 . At time t_2 , another desired indentation may be made in the surface; and so on and so forth where Δt may be seconds, hours, days, weeks, and so on. Thus, for example, a two dimensional array of grooves containing fine microstructural and nanostructural features thereon may be created in a single step process (as appropriate) or a multi-step process, with none or various actions between the steps, as we believe a person skilled in the art will readily understand.

[0199] According to a non-limiting, illustrative two step process, in a first step, we produce grooves in the surface of the material of interest using relatively high laser fluence. In a second step, we reduce the laser fluence to a value most favorable for producing nano- and micro-structures and process the surface again. Relatively low values of laser fluence may be more favorable for producing nanoroughness, while relatively moderate values may be more favorable for producing a combination of nanoroughness and fine microroughness. Multiscale surface structures, for example, may be more efficient for modifying hydrophilicity or hydrophobicity. Multiscale fine structures may thus be more favorable when seeking to enhance the wettability of the grooved surface. We are able to produce non-wicking (strictly speaking, slightly wicking because any surface structure can be considered as a 2D network of capillary channels) structures in the form of microgrooves. To produce wicking structures on the microgroove surface, we can set the number of overlapping pulses and laser fluence in the second step to values that are favorable for producing laser-induced periodic structures (LIPSS; LIPSS are 1D nanogratings), as discussed elsewhere herein.

[0200] Typically, their structure is an array of parallel nanogrooves having a width of about 200-300 nm, a depth of about 100 nm, and a period of about 500-600 nm, for the fundamental wavelength of a Ti-sapphire laser. Furthermore, the surface of LIPSS is extensively covered with fine nanostructures. Since the direction of LIPSS nanogrooves depends on the light polarization direction, we can produce LIPSS nanogrooves that are parallel to the microgrooves.

Superwicking

[0201] The following is a non-limiting, illustrative description of superwicking embodiments of the invention in a glass material. Glass has been widely used in traditional fluidic devices and more recently in optofluidic devices. The behavior of liquids on a solid surface is determined by the

surface wettability, which can be controllably modified through engineered surface structuring. According to an embodied aspect of the femtosecond laser structuring method, we created novel surface patterns that transform a regular glass surface into a superwicking material surface for water, which in a gravity defying way, enabled water to sprint vertically upwardly along the structured glass surface at an unprecedented velocity of 3.8 cm/sec, following a square root of time dependence.

Experimental Setup

[0202] To create the embodied structural alteration of a glass surface, we used (as described elsewhere herein above) an amplified Ti:sapphire laser system that generated 65 fs pulses with energy around 1.1 mJ/pulse at a maximum repetition rate of 1 kHz with a central wavelength of 800 nm. The laser beam was horizontally polarized and was focused normally onto the glass samples mounted vertically on a translation stage. The samples were microscope glass slides with a dimension of 25×25×1 mm³. We produced a 20 mm long microgroove along the horizontal direction by scanning the sample across the laser beam, followed by a vertical shift of the sample by 100 μm. This process was repeated to create an extended array of parallel microgroove structures. The resulting structured area was 20×9 mm². A scanning electron microscope (SEM) and three dimensional (3D) laser scanning microscope from Keyence were used to examine the surface structures following the femtosecond laser treatments. Contact angle measurements were performed with a VCA 2500XE video contact angle system.

Experimental Results and Discussion

[0203] A photograph of the laser treated glass sample is shown in FIG. 38(a). SEM images of the surface structures created on the glass surface are shown in FIGS. 38(b-d). FIG. 38(b) shows that the treated surface has multiple parallel microgrooves with a period of 100 μm, corresponding to the vertical step between two horizontal scanning lines. More detailed surface structural features are shown in FIGS. 38(c) and (d), where both ridges and valleys of the microgrooves are covered with nano- and fine micro-structures. As seen from FIG. 38(d), the nanostructures include both nanopillars and nanocavities, while the fine microstructures include microcavities and microscale aggregates from nanoparticles that fuse onto each other and on the glass surface. FIG. 39 shows a 3D optical image of the treated surface.

[0204] We studied the wetting properties of the structured glass sample both along and perpendicular to the groove orientation. Distilled water was used in our study, and we recorded the water spreading dynamics on the structured surface using a camera. FIGS. 40(a-f) show the wetting dynamics of a 3 μl water droplet pipetted on the horizontally positioned structured glass surface. For comparison, the behavior of a 3 μl water droplet pipetted on an untreated glass surface is also shown in FIGS. 40(a-f). As shown, the water drop spread highly anisotropically on the treated area and it flowed preferentially along the microgrooves. We repeated the experiments with different volumes of water in the range of 1-6 μl, all of which showed a similar highly anisotropic wetting behavior. When the glass slide was stood vertically with the grooves oriented parallel to the table, the highly anisotropic water spreading behavior remained the

same, and we observed no noticeable downward flowing. This can be clearly seen from FIGS. 41(a-f). From FIG. 40(b) we can also deduce that the average initial velocity of water spreading is about 5.8 cm/s within the first 0.2 s. As shown in FIGS. 40(c-f), the water spreading velocity decreased with time.

[0205] We next oriented the glass slide with the grooves perpendicular to the table. When we pipetted a water droplet on the bottom of the groove area, the water immediately sprinted vertically uphill (against gravity), as shown in FIGS. 42(a-f). It can be seen from the figures that this gravity-defying uphill motion extends over several centimeters. We noted that the water spread to the very top of the sample and we expect that the water would continue to spread higher with a taller sample. This experiment clearly demonstrated that we transformed a regular glass surface into a superwicking surface having a capillary driving force much stronger than gravity. From FIGS. 42(a-f) we deduced that the average water spreading velocity was about 3.8 cm/sec within the first 0.2 s, slightly lower than the water spreading velocity along the horizontal grooves.

[0206] Wetting of textured surfaces is commonly explained by the classical Wenzel and Cassie models (R. N. Wenzel, *Ind. Eng. Chem.* 28, 988 (1936); A. B. D. Cassie and S. Baxter, *Trans. Faraday Soc.* 40, 546 (1944)). The Wenzel model assumes that a liquid penetrating into a surface texture will completely wet the surface, whereas in the Cassie model the liquid does not fill the texture and there are air pockets between the liquid and the textured solid surface. The liquid drop is very adhesive in the Wenzel regime, while it will roll easily on the surface at small tilts in the Cassie regime. In the Wenzel model, the wetting is described by relation $\cos \theta^* = r \cos \theta$, where θ^* is the apparent contact angle on a rough surface, r is the roughness factor (the ratio of the actual surface area to the geometrically projected area on the horizontal plane), and θ is the contact angle on a smooth horizontal surface of the same material. Since r is always greater than 1, the surface texture will enhance the hydrophilicity of an originally hydrophilic surface ($\theta < 90^\circ$) and enhances the hydrophobicity of an originally hydrophobic surface ($\theta > 90^\circ$). In our study, the contact angle θ for water on a smooth glass surface before the laser treatment was measured to be 15° and, therefore, the smooth glass surface is originally hydrophilic ($\theta < 90^\circ$). According to the Wenzel model, a surface texture should enhance the hydrophilicity of the glass. In our experiment, the apparent contact angle for the laser treated surface was found to be essentially 0° . Therefore the surface structure produced here turns the glass surface superhydrophilic. As demonstrated in FIGS. 40-42, the water drop deposited onto our textured surface is immediately sucked into the texture and water spreads quickly along the microgrooves for an extended distance from the point of deposition.

[0207] In the past, liquid flow has been studied in capillary systems such as tubes, open surface grooves, and two dimensional arrays of pillars. In 1921, Washburn (E. W. Washburn, *Phys. Rev.* 17, 273 (1921)) showed that motion of a wetting liquid in a capillary tube follows a diffusion law as $z(t) \propto D(t)^{1/2}$, where z is the distance traveled by the liquid, t is the time, and D is the diffusion constant. Following Washburn's work, behaviors of wetting liquids have been studied for open capillary systems such as surface grooves and two-dimensional arrays of pillars. Rye et al. (R. R. Rye, J. A. Mann, and F. G. Yost, *Langmuir* 12, 555 (1996)) have

shown that the wicking dynamics in open V-shaped grooves also follows the Washburn-type $t^{1/2}$ dependence as $z^2 = K(\alpha, \theta)[\gamma h_0/\mu]t$, where $K(\alpha, \theta)$ is the geometry term with α and θ being the groove angle and the contact angle, γ and μ are the surface tension and viscosity of the liquid, and h_0 is the groove depth. Therefore, a structured surface can be viewed as a network of open capillaries, where the liquid spreading from a reservoir usually follows the Washburn-type scaling law $z \propto (Dt)^{1/2}$, where D is the diffusion constant. Deviations from the $t^{1/2}$ dynamics have been observed at short initial stages of the fluid motion in tube capillaries, where fluid flow exhibits $z \propto t^2$ and $z \propto t$ dependences before reaching the Washburn behavior. To determine the imbibition dynamics of our ultrafast laser-structured surface, we plotted the uphill travel distance z as a function of $t^{1/2}$ for the vertically standing sample, as shown in FIG. 43. One can see that the spreading distance linearly depends on $t^{1/2}$ for our glass surface despite its complex surface geometry. Similar spreading dynamics are also observed on the horizontally positioned sample. We believe that the superwicking action of the structure created here is due to combined capillary effects of open microgrooves and finer structures at nano- and fine micro-scale superimposed on the microgrooves.

Superwetting

[0208] The following is a non-limiting, illustrative description of superwetting embodiments of the invention in dentin and/or enamel materials.

[0209] Good wettability of enamel and dentin surfaces is an important factor in enhancing adhesion of restorative materials in dentistry. In general, the wetting of a solid surface by a liquid depends on three major factors: (1) the surface energy of the solid and the liquid; (2) the viscosity of the liquid; and (3) the surface topography of the solid. Therefore, surface texturing of the enamel and dentin surfaces is one of the approaches for improving the wettability and consequently, bonding strength. Furthermore, the surface texturing increases the surface area, which enhances mechanical interlocking between a restorative material and enamel or dentin. At the present time, etching with an acidic or basic solution is a widely used approach for surface texturing in adhesive dentistry, having known disadvantages.

[0210] According to the embodied invention, a femtosecond laser is used to texture the surface of hard dental tissues that makes both the enamel and dentine surfaces superwetting. In contrast to the traditional chemical etching which yields a random surface roughness, the embodied technique produces an engineered surface structure with a strong capillary action that enables controllable modification of the wetting in any extent between the initial wetting and superwetting. In an illustrative aspect, the engineered surface structure is an array of parallel microgrooves that generates a strong capillary force. Due to the powerful capillary action, water is immediately sucked into this engineered surface structure and spreads even on a vertical surface against gravity at a high speed of about 20 mm/s. The embodied approach for controllable improving the wettability of a dentin/enamel material can be extended to bones (because both (human) teeth and bones are mainly composed of hydroxyapatite) and may be also used for hydroxyapatite coatings of implants, for example. The embodied method for modifying the wettability is also suitable for a

variety of biocompatible materials used in dentistry, medicine, biomedicine, and biosensing.

[0211] The superwetting work disclosed herein below was performed on extracted caries-free human molars. Prior to femtosecond laser treatment, enamel/dentine surfaces were flattened with 240-, 600-, 1000-, and 2000-grit SiC abrasive papers. After sanding, the teeth were rinsed in distilled water and stored in distilled water up to the laser treatment. For surface texturing of enamel/dentine specimens, we used an amplified Ti:sapphire laser system that generated 65-fs pulses with energy around 1.2 mJ/pulse at a maximum repetition rate of 1 kHz at a central wavelength of 800 nm. The laser beam was horizontally polarized and was focused normally onto the specimen mounted vertically on a translation stage. We scanned the specimen across the laser beam to produce a 6 mm long microgroove along the horizontal direction followed by a vertical shift of the specimen by 100 μ m. This process was repeated to create an extended array of parallel microgrooves. A surface area textured with the microgroove pattern was 2.5 \times 6 and 2.2 \times 6 mm² on the enamel and dentin specimens, respectively. To obtain desired wetting properties, the surface structure was tailored by varying laser fluence, pulse repetition rate, scanning speed, and focused laser spot diameter.

[0212] A scanning electron microscope (SEM) and 3D laser-scanning microscope VK-9700 from Keyence Co were used to examine the surface structures following femtosecond laser treatments. The wetting properties of the dental hard tissues are reportedly often tested using water contact angle measurements. We also tested the wettability of the treated specimens by measuring the contact angle θ of a distilled water drop with a volume of 1 μ l. The water contact angle on both the laser treated and untreated surfaces was measured by the sessile-drop method using a VCA 2500XE video contact angle system. The spreading dynamics of distilled water on the treated surface was studied using a video camera.

[0213] Photographs of the laser treated enamel and dentine specimens are shown in FIGS. 44(a) and 45(a), respectively. The 3D optical images of the surface structures produced on the enamel and dentine specimens are shown in FIGS. 44(b) and 45(b), respectively. The treated surfaces have multiple parallel microgrooves with a period of 100 μ m, corresponding to the step between two laser scanning lines. The depth of the microgrooves on the enamel and dentine specimens is about 120 μ m and 100 μ m, respectively. The SEM images in FIGS. 44(c), (d) and 45(c), (d) show fine structural details of the microgroove surface. The water contact angle before the laser treatment was measured to be 42° and 48° on the enamel and dentine specimens, respectively. The contact angle on the laser-treated surface was found to be ~0° for both the enamel and dentin specimens. A liquid wets a solid surface when its contact angle on the surface is smaller than 90°. Commonly, a surface is referred to superwetting (or superhydrophilic) when the water/liquid spreads to zero or nearly zero contact angle. Therefore the illustrative surface structures turn both the enamel and dentin surfaces superwetting.

[0214] Snapshots in FIGS. 46(a) and 46(b) show the spreading dynamics of a 1 μ l water droplet pipetted on the horizontally-positioned enamel surface, where one can see that the water rapidly spreads over the laser-treated area. As seen in FIG. 46(b), the water spreads for a distance of about 4.5 mm in 0.2 s. From these data, we can deduce that an

average velocity of water spreading is about 22.3 mm/s within the first 0.2 s. The spreading dynamics of a 1 μ l water droplet pipetted on the vertically-positioned enamel surface with the microgrooves oriented perpendicular to the table is shown in FIGS. 46(c) and 46(d), where it is seen that the water immediately sprints vertically uphill against gravity. From FIGS. 46(c) and 46(d), we can infer that the average water spreading velocity is about 21.5 mm/s within the first 0.2 sec, slightly lower than that on the horizontal enamel surface. Similar superwetting behavior of the water is also observed on the laser-treated dentin specimen as shown in FIG. 47 for horizontal and vertical orientations of the dentin surface. FIGS. 47(a) and 47(b) show that the horizontally-oriented treated surface is completely wetted at $t=0.2$ s. From FIGS. 47(c) and 47(d), we can derive that the average water spreading velocity on the vertical dentin surface is about 21.7 mm/s within the first 0.2 s. Our data clearly show that the water completely wets a large structured area within a fraction of a second.

[0215] Human enamel and dentin are heterogeneous substances, dentin more especially than enamel, which consists of 95% hydroxyapatite ($\text{Ca}_{10}(\text{PO}_4)_6(\text{OH})_2$), 4% water, and 1% collagen fibers. The dentin is highly heterogeneous and contains 70% hydroxyapatite, 20% collagen fibers, and 10% water. Moreover, the dentin also has a structural complexity due to the dentinal tubules. As a consequence, the wettability modification of the dentin using the commonly known chemical approaches is a much more complicated procedure than that for the enamel. In contrast to the common chemical approaches, the embodied method easily improves the wettability of both the enamel and dentin.

[0216] Previously reported behavior of wetting liquids in open capillary systems such as surface grooves has shown that the capillary effect in the surface grooves depends on their geometry. For example, it has been reported that the liquid spreading in open V-shaped grooves is given by the relation $z^2=K(\alpha,\theta)[\gamma h_0/\mu]t$, where z is the spreading distance, $K(\alpha,\theta)$ is the geometry term with α and θ being the groove angle and the contact angle, γ and μ are the surface tension and viscosity of the liquid, h_0 is the groove depth, and t is the time. Therefore, varying the geometry of the grooves allows the controllable modification of the wetting in any extent between the initial wetting and superwetting. In addition to a regular 1D-array of capillary microgrooves, other networks of capillary channels (regular or irregular) for improving the wettability can be designed and fabricated (for example, a regular 2D-array of microgrooves with a uniform liquid spreading in all directions).

[0217] Previous studies on applications of femtosecond lasers in dentistry have demonstrated such advantages as (i) minimal collateral damage (thermal and mechanical), (ii) high precision, (iii) producing microcrack-free cavities, (iv) the absence of a chemical change in the treated dental hard tissues, and (v) high processing controllability through a spectroscopic feedback. The embodied invention demonstrates that this list can be expanded by the ability of the femtosecond laser to improve significantly the wettability of the dental hard tissues for enhanced bonding through producing engineered surface structures.

[0218] In another demonstrative application, high-intensity femtosecond laser pulses were used to create a superwetting surface pattern on platinum and gold plates, all having a dimension of 25 \times 25 mm². The structured metals were created with an amplified Ti:sapphire laser that gen-

erated 65 fs pulses with energy around 1.1 mJ/pulse at a maximum repetition rate of 1 kHz at a central wavelength of 800 nm. The samples were mounted vertically on a translation stage. The laser beam was horizontally polarized and was focused normally onto the samples. We produce an extended area of surface structures by scanning the samples across the laser beam along the horizontal direction followed by a vertical shift. This process was repeated to obtain a structured circular area of 24 mm in diameter. A scanning electron microscope (SEM) was used to examine surface structures following femtosecond laser treatment.

[0219] FIG. 48 shows typical surface pattern created on the metals following femtosecond laser treatment. FIG. 48(a) shows that the surface has multiple parallel microgrooves with a period of 100 μ m, corresponding to the vertical step between two horizontal scanning lines. As shown in FIGS. 48(b-d), a combination of porous nanostructures and fine microstructures are superimposed on both ridges and valleys of the grooved pattern. From FIGS. 48(c) and (d), one can see that the nanostructures include nanoprotusions and nanocavities, while fine microstructures include microcavities and microscale aggregates of nanoparticles that fuse onto each other and on the metal surface. As further illustrated in FIG. 49, the structured surfaces appear pitch black, indicating a significant change in optical properties of the studied metals as reported herein above.

[0220] The surface wetting properties of the structured platinum were studied by positioning the sample horizontally, vertically, and tilted at a 45° angle. The liquid used was methanol. The spreading dynamics of methanol on the structured surfaces was recorded using a video camera at a speed of 30 frames/s. FIGS. 49(a-d) show the wetting dynamics for a large drop of methanol pipetted on the horizontal surface of the structured platinum. The liquid can be seen to spread highly anisotropically and preferentially flow along the surface microgrooves. Similar experiments with smaller methanol drops at a volume in the range of 1-10 μ l also showed similar highly anisotropic wetting responses. To determine whether the wetting anisotropy of the structured platinum was caused by the parallel microgrooves, as shown in FIG. 48(a), we produced another platinum sample with orthogonally crossed microgrooves. In this case, the methanol spread uniformly along all directions indicating that the capillary effect in the open microgrooves plays a dominant role in directionally guiding the liquid.

[0221] When we positioned the platinum sample upward at 45° and vertically at 90°, the drop of methanol moved rapidly uphill against gravity, as seen in FIGS. 50(a-d) for the vertically standing sample. To confirm that the uphill motion of the liquid was caused by the metal surface structures, we repeated the above experiments with an untreated platinum sample and found that the methanol did not flow upward at all. To study the wetting dynamics, we videotape the liquid spreading from the moment when methanol was dropped on the structured metal surface, and FIGS. 49 and 50 show the frames as the liquid moves with time. We observed that the average wetting velocity was 1.6, 1.18, and 1 cm/s for the treated platinum oriented horizontally, 45° upward, and 90° upward, respectively. We believe that these are the highest liquid moving speeds upward that one has observed on a metal surface.

[0222] When the bottom part of a vertically standing sample of structured platinum was submerged in a methanol reservoir, the methanol spread only along the microgrooves

that were submerged in the methanol, but did not expand laterally to grooves that were not initially in contact with the methanol in the reservoir. However, when the sample was enclosed in a transparent container to suppress evaporation, a similar vertical wetting strip was formed rapidly, but the liquid also spread slowly in the lateral directions until the entire structured black surface became wet. The methanol spreading speed in the lateral direction was about an order of magnitude lower than that along the vertical grooves. Thus in addition to the engineered capillary effect, evaporation also plays a role for the unidirectional spreading of methanol in open air. Therefore, in addition to a physical wetting boundary formed by the outmost groove walls that are in contact with the methanol reservoir, the evaporation actually creates a virtual wall leading to a significantly enhanced anisotropic (essentially unidirectional) wetting behavior. When evaporation was suppressed in the enclosed container, the observed wetting for the vertically standing black platinum in all directions showed that the nano- and micro-structures superimposed on the groove pattern also enhanced the wicking effect of the platinum specimen.

[0223] Another observed property of the structured platinum was that a significant amount of liquid could be transported uphill due to a strong capillary pumping effect. To illustrate this effect, we structured a long stripe of surface area of 2 mm wide and 25 mm long on a platinum foil and bent the foil into an L shape, as shown in FIG. 50(e). We then immersed the bottom edge of the black stripe in a methanol reservoir. Within 10 min, a large drop of methanol accumulated at the upper end of the black stripe that was 10 mm above the methanol reservoir surface, as shown in FIG. 50(f). The accumulated liquid volume was measured to be about 10 μl , indicating that the structured platinum can draw a significant amount of liquid against gravity to an elevated point.

[0224] The self-propelled motion of liquids against gravity has been observed in the past when the surface has a hydrophobicity gradient that causes a liquid drop to move from a more hydrophobic surface area to a less hydrophobic area. In our experiments, however, there is no hydrophobicity gradient along the direction of the liquid spreading and therefore, this mechanism could be ruled out. Another known mechanism that drives liquids uphill on an inclined surface is the classical “tears of wine” phenomenon, originally observed in a glass of strong wine and explained by Thomson (J. Thomson, Philos. Mag, 10(4), 330 (1855)). This phenomenon is caused by a preferential evaporation of alcohol from alcohol-water mixture that produces a concentration gradient and a surface tension gradient that generates a force driving a liquid film upward on the wine glass wall. The drawn-up liquid accumulates on the glass walls and then forms running-down droplets called tears of wine. To determine whether the vertically upflowing liquid is a similar evaporation-driven phenomenon in our experiment, we placed the methanol reservoir with the submerged sample shown in FIG. 3(f) in a closed transparent container, and observed that liquid did not accumulate at the top end of the black metal track any more, although the blackened track was wetted due to the capillary effect. The accumulation of methanol on the top end of the blackened track occurred again as soon as the container was reopened. We thus believe that the methanol accumulation was due to the evaporation-driven Marangoni effect, where fluid flow is induced by surface tension gradients in volatile liquids. Although we

used a single-component volatile liquid, the absorption of water from the atmosphere can make our liquid become a two-component mixture to some degree. The fact that the vertically standing structured metal surface remained constantly wet in a closed container showed that the surface structures alone have an extraordinarily strong wicking effect even in the absence of the driving force from the evaporation.

[0225] Table I shows a variety of laser processing parameters for various materials including platinum (Pt), glass, dentine, and enamel. Therein below, Table I also lists exemplary engineered features in the various materials in the left column and dimensional ranges for these features in the right column. Table I thus provides a recipe that will enable the skilled person to create the embodied superwicking and/or superwetting effects in various materials and for various applications.

TABLE I

Laser processing parameters	
	Parameter range
Metal sample (Pt)	
Laser fluence:	0.05-200 J/cm ²
Spot diameter:	0.1 μm -5 cm
Pulse duration:	5 fs-continuous wave
Pulse repetition rate:	1 Hz-50 MHz
Scanning speed:	0.1 $\mu\text{m}/\text{sec}$ -5 cm/sec
Step between scanning lines:	0.1 μm -5 cm
Ambient gas:	air; inert or chemically active gases; inert or chemically active liquids; Vacuum
Glass sample	
Laser fluence:	0.5-500 J/cm ²
Spot diameter:	0.1 μm -2 cm
Pulse duration:	5 fs-continuous wave
Pulse repetition rate:	1 Hz-80 MHz
Scanning speed:	0.1 $\mu\text{m}/\text{sec}$ -2 cm/sec
Step between scanning lines:	0.1 μm -2 cm
Ambient gas:	air; inert or chemically active gases; inert or chemically active liquids; Vacuum
Dentine sample	
Laser fluence:	0.05-50 J/cm ²
Spot diameter:	0.1 μm -1 cm
Pulse duration:	5 fs-continuous wave
Pulse repetition rate:	1 Hz-80 MHz
Scanning speed:	0.1 $\mu\text{m}/\text{sec}$ -1 cm/sec
Step between scanning lines:	0.1-500 μm
Ambient gas:	air; blowing inert or chemically active gases
Enamel sample	
Laser fluence:	0.05-50 J/cm ²
Spot diameter:	0.1 μm -1 cm
Pulse duration:	5 fs-continuous wave
Pulse repetition rate:	1 Hz-80 MHz
Scanning speed:	0.1 $\mu\text{m}/\text{sec}$ -1 cm/sec
Step between scanning lines:	0.1-500 μm
Ambient gas:	air; blowing inert or chemically active gases

TABLE I-continued

Laser processing parameters	
Structures	Structure range
Grooves on metal (Pt)	
Period: 100 μm	10 nm-10 cm
Width: 100 μm	10 nm-5 mm
Depth: 75 μm	10 nm-5 mm
Grooves on glass	
Period: 100 μm	10 nm-10 cm
Width: 100 μm	10 nm-5 mm
Depth: 40 μm	10 nm-5 mm
Grooves on dentin	
Period: 95 μm	10 nm-2 mm
Width: 95 μm	10 nm-2 mm
Depth: 100 μm	10 nm-2 mm
Laser processing parameters	
Grooves on enamel	
Period: 100 μm	10 nm-2 mm
Width: 100 μm	10 nm-2 mm
Depth: 120 μm	10 nm-2 mm
Fine microroughness covering the groove surface of metal, glass, dentin, and enamel	
Size: 0.5-10 μm	0.5-100 μm
Shape: various	protrusion, cavity, sphere, rod, other irregular shapes
Nanoroughness covering the groove surface of metal, glass, dentin, and enamel	
Size: 5-500 nm	1-500 nm
Shape: various	protrusion, cavity, sphere, rod, and other irregular shapes

Biomimetic Multifunctional Surfaces Produced by Femtosecond Laser Pulses

[0226] The following is a non-limiting, illustrative description of embodiments of multifunctional surfaces produced by femtosecond laser pulses.

[0227] A multifunctional metal surface (including metal alloys) may be produced having hierarchical nano- and micro-structures using femtosecond laser pulses. In some embodiments, the multifunctional surface produced exhibits dramatically enhanced broadband absorption, superhydrophobicity, and self-cleaning effects.

[0228] The superhydrophobic effect, in some instances, may be demonstrated by a falling water droplet repelled away from a clean altered surface with 30% of the droplet kinetic energy conserved, while the self-cleaning effect may be shown, in some instances, by each water droplet taking away a significant amount of dust particles from an altered surface covered with dust. The enhanced light absorption of certain embodiments of a multifunctional metal surface may be useful whenever light collection is needed, for example in sensors and solar energy absorbers. The superhydrophobicity and self-cleaning effects may, in some instances, improve the performance and reduce the maintenance of the devices that utilize these surfaces.

[0229] In some embodiments, such multifunctional properties may be similar to properties exhibited by certain biological surfaces. One of the examples is the water-

repelling lotus leaves. The lotus leaves have a number of functionalities, such as superhydrophobicity, self-cleaning, and defense against pathogens. Studies have shown that the lotus leaf surface has a hierarchical structure containing a larger micro-scale structure in the range of 10-50 μm and a finer structure in the range of 0.2-2 μm . This hierarchical structure along with a hydrophobic epicuticular wax coating imparts the superhydrophobicity to lotus leaves. Furthermore, the hierarchical surface structure significantly reduces the adhesion of contaminants to the surface. Both enhanced hydrophobicity and reduced contaminant adhesion produce the lotus self-cleaning effects, often referred as the "lotus effect." The lotus self-cleaning is achieved when water drops roll over the leaves, pick up the dust particles, and carry them away when rolling off the leaves. Another example of the multifunctional biological surface is the Morpho butterfly wing. The surface structures of the wings produce a blue color and also make the wing surface superhydrophobic and self-cleaning.

[0230] As discussed above, femtosecond laser surface processing can produce a wide variety of hierarchical nano- and micro-structures that can significantly modify optical and wetting properties of metals. In the experiments described below, we produce nature-inspired hierarchical surface structures on metals and demonstrate that the structured surfaces exhibit multifunctional properties, including superhydrophobicity, self-cleaning, and enhanced broadband absorption from the ultraviolet to mid-infrared. The enhanced light absorption may be useful, for example, whenever light collection is needed, for example in sensors and solar energy absorbers. The superhydrophobicity and self-cleaning effects may improve, for example, the performance and reduce the maintenance of the devices that utilize these surfaces. Furthermore, our multifunctional surfaces also should possess, in at least some instances, other highly desirable functionalities, such as anti-corrosion, anti-adhesive, anti-icing, anti-fouling, antimicrobial, and self-sanitation, which are intrinsically associated with the superhydrophobicity.

[0231] A laser-treated platinum surface is shown in FIG. 51(a). The treated surface appears velvet black at all viewing angles, indicating a significant increase of optical absorption. A hierarchical surface structure produced on platinum is shown in FIGS. 51(b)-(d). In this particular example, this structure is an array of parallel microgrooves covered by extensive nanostructures. The microgroove spacing is about 100 μm , and the depth is about 75 μm . In other non-limiting examples microgroove spacing may be in a range of 0.1-500 μm and microgroove depth may be in a range of 0.1-500 μm . In other non-limiting examples microgroove spacing may be in a range of 10-250 μm and microgroove depth may be in a range of 10-250 μm . In other non-limiting examples microgroove spacing may be in a range of 50-150 μm and microgroove depth may be in a range of 50-150 μm . In other examples, the structure is an array of periodic and/or random nanostructure-covered microcolumns, nanostructure-covered microcones, and/or nanostructure-covered microcavities. In some of these other examples, the depth or height of the microstructures may be in a range of 0.1-500 μm , 10-250 μm , or 50-150 μm and the spacing of the microstructures may be in the range of 0.1-500 μm , 10-250 μm , or 50-150 μm .

[0232] SEM examination shows that the smallest nanoscale features, in this particular example, are about 5-10

nm. In some embodiments, the nanoscale features may include nanosphere and/or other nanoprotusions extending outwardly from an associated microstructure and having dimensions (such as a width, diameter, and/or height) in the range of 1-100 nm, 1-50 nm, and/or 1-25 nm as well as larger nanoscale features. In some embodiments, the nanoscale features may include nanocavities, nanodepressions, and/or other nanostructures extending into an associated microstructure and having dimensions (such as a width, diameter, and/or depth) in the range of 1-100 nm, 1-50 nm, and/or 1-25 nm as well as larger nanoscale features.

[0233] Following the laser treatment, superhydrophobicity develops after the sample is exposed to air. In some instances, laser parameters, such as fluence, pulse duration, wavelength, repetition rate, and/or scanning speed may be chosen to obtain the desired results. Sometimes, two-step processing, where microstructures and nanostructures are produced separately, may be utilized. In one example of two-step processing, first the microstructures are produced using a set of laser parameters favorable for microstructuring and then the produced microstructures are treated with a different set of laser parameters to produce nanostructures on the surface of the microstructures.

[0234] In at least some instances, an intrinsic hydrophilic surface will become more hydrophilic with hierarchical structures, while an intrinsic hydrophobic surface will become more hydrophobic with hierarchical structures. Therefore, a super-hydrophobic surface with hierarchical micro and nano-scale structures may not necessarily be structurally very different from a super-hydrophilic surface. However, in some examples, a superhydrophilic material with hierarchical structures can become superhydrophobic by changing its surface chemical property, such as coating it with a hydrophobizing agent. In such examples, the hierarchical surface structure remains the same but the transition from superhydrophilicity to superhydrophobicity occurs due to a change of surface chemistry. In other examples, it is also possible to turn a hydrophilic surface to hydrophobic or vice versa purely by changing the surface structures.

[0235] To characterize the hydrophobicity of the treated platinum surface in the example shown in FIGS. 51(a)-(d), we measured the water contact angle on the surface to be 158°, and a water drop will slide on the treated surface at a tilt angle of only 4°. More remarkably, when a drop of water is released and falls towards the treated surface, the water droplet is repelled by the treated surface to such a degree that it bounces off the surface, lands again due to the gravity, and bounces again and slides off the treated surface, as shown in FIG. 52. Here, the water drop is released 19 mm above the surface, reaches a height of 5.3 mm after the first bounce, and lands 13.75 mm away from the first bounce before bouncing off the surface. About 30% of the water droplet kinetic energy is conserved from the first bounce. The two bouncing motions last less than 0.5 second, and, as shown in FIG. 52(f) the laser-treated surface remains completely dry afterwards.

[0236] A decrease of surface tension on a solid surface can also enhance the hydrophobicity. Therefore, another approach to increase the hydrophobicity is to decrease the surface tension by coating a hydrophobic layer on the solid surface. The largest water contact angle ever achieved in the past through coating on a smooth surface is only about 120°, which is far less than 150°, the minimum water contact angle required for being qualified as superhydrophobicity. How-

ever, in at least some instances, a combination of surface structuring (e.g. a hierarchical surface structure such as the ones discussed in this application) and a hydrophobic chemical coating can produce strong superhydrophobicity. Non-limiting examples of chemical coatings include non-polar, hydrophobic groups with low surface energies such as hydrocarbons ($-C_mH_{2m+1}$), silicones ($CH_3-(Si-O)-CH_3$), and fluorocarbons ($-C_mF_{2m+1}$). Metals are intrinsically hydrophilic; immediately after femtosecond laser surface structuring, they first become more hydrophilic, but the exposure to air turns the metals superhydrophobic. This transition is explained by chemical interaction between the surface and the ambient CO_2 , resulting in an accumulation of carbon and its compounds on the laser-treated surface. We believe that the laser-induced surface nanostructures may also play an important role in enhancing this chemical interaction due to nanochemical effects.

[0237] In nature, self-cleaning occurs on a superhydrophobic surface with water from rain, dew, and fog. These water sources supply falling, rolling, and sliding drops. The rolling and falling drops are more efficient in removing dust particles than the sliding drops. FIG. 53 shows self-cleaning of dust particles on the black platinum of FIG. 51(a) by applying a string of water drops. The dust particles are a collection of real-life dusts from a vacuum cleaner; the size of the particles is in the range of 0.1-2 mm. Before cleaning, about 40 particles are present on the surface and about 50% of the dust particles are removed with only 3 drops of water. The amount of dust particles decreases to a half again with 4 more water drops, see FIG. 53(c). After about 14 water drops, the surface becomes virtually clean. Afterwards, the laser-treated superhydrophobic surface area remains completely dry, while we can see that water sticks to the untreated area even upside down. We also apply water on an untreated platinum sample covered with dust particles. In contrast to our superhydrophobic surface, water remains on the untreated surface with all the dust particles floating inside [FIG. 53(f)]. After water vaporizes, all the dust particles remain on the surface of the untreated surface. In our study, we repeatedly perform 20 cleanings on the superhydrophobic surface and did not observe any degradation of the self-cleaning effect.

[0238] Self-cleaning surfaces in accordance with some, although not necessarily all, embodiments of the present invention should have the following properties: (i) large water contact angle exceeding 150°, (ii) small sliding angle ($<10^\circ$) to cause water drops easily roll off the surface, and (iii) the adhesion between the surface and dust particles on the surface should be smaller than that between the dust particles and water. In some instances, the sliding angle may be the minimum angle when a liquid droplet (e.g. a droplet of distilled water or another "clean" liquid) begins to slide down on the inclined surface at room temperature. The surface structures we produced benefit self-cleaning in two ways. First, the surface structures turn a metal surface superhydrophobic; secondly, the surface structures also reduce the adhesion of dust particles to the solid surface. When the size of dust particles is larger than surface cavities, the particles will sit on the top of surface protrusions, and this reduces the adhesion due to a decrease of the contact area. Therefore, these particles can be easily removed by rolling water drops. However, when the particle size is smaller than the surface cavities, the rolling drops may not be efficient for cleaning. In this situation, falling drops with

a sufficiently high kinetic energy are needed to penetrate into the cavities and remove the small dust particles. In addition to self-cleaning, the superhydrophobicity also enables a number of other potential functionalities, such as anticorrosion, anti-icing, anti-biofouling, anti-microbial, low flow resistance, and platelet anti-adhesion.

[0239] We have also produced multifunctional black and superhydrophobic titanium and brass surfaces, which show similar self-cleaning behavior as the Pt surface described above. To characterize the optical property of these three multifunctional surfaces, we measured the wavelength dependent reflectance of their surfaces with the spectrophotometer and FTIR spectrometer. The results of these measurements are shown in FIG. 54. For comparison, we also measured the reflectance of mechanically polished surfaces of the three metals before laser treatment. As shown in FIG. 54, the multifunctional surfaces have a very low reflectance over a broad range of wavelengths. The reflectance in the visible wavelengths is in a range of 1.3-3.5%, 3.3-4.1%, and 4.2-4.5% for brass, Pt, and Ti, respectively. For comparison, the reflectance of mechanically polished surfaces of the three samples is much higher as shown in FIG. 54. Because of the extremely low reflectance, all three sample surfaces appear pitch black. Furthermore, these surfaces also have low reflectance in the near infrared, which increases with wavelength slightly for Pt and Ti but significantly for brass. At 16 μm , the absorption is 9% for Pt, 18% for Ti, and 73% for brass. The measured reflectance shows that the black Pt and Ti surfaces are excellent broadband absorbers of electromagnetic radiation from the ultraviolet to mid-infrared.

[0240] It is known that absorptance, A , of a clean structured metallic surface is given by $A(\lambda) = A_{INTR}(\lambda) + A_{SS}(\lambda)$, where A_{INTR} is the intrinsic absorptance of a flat, clean, and ideally smooth surface and A_{SS} is the contribution of surface structures. The dramatically enhanced absorption of our structured surface over a broad spectral range comes from several mechanisms. The surface structures smaller than light wavelength (nanostructures and fine microstructures) enhance absorptance through antireflection effect of the graded refractive index formed by subwavelength surface textures at the air/solid interface. Furthermore, these subwavelength surface structures significantly enhance absorptance through plasmonic absorption. On the other hand, the surface structures greater than the light wavelength enhance absorptance through light trapping in surface cavities and the Fresnel angular dependent reflection. All these absorption mechanisms contribute to the broadband high absorption, leading to the structural black color in the visible spectral range. The hierarchical surface structures produced on Pt and Ti are more optimized for the broadband absorption in the wavelength range of 0.25-16 μm . The surface structures on metals can also be optimized for efficient absorption in the THz range, where regular metals are perfect reflectors.

[0241] One application for the enhanced light absorption is building better solar absorbers for efficient conversion of solar energy to thermal or electrical energy. Solar radiation is broadband and mainly composes of ultraviolet ($\lambda < 0.4 \mu\text{m}$), visible ($0.4 < \lambda < 0.7 \mu\text{m}$), and infrared radiation ($0.7 < \lambda < 100 \mu\text{m}$). At the sea level, the fraction of solar energy in the ultraviolet, visible, and infrared wavelengths are about 4%, 42%, and 54%, respectively. From practical point of view, almost all solar energy is contained in the wavelength range of $0.2 < \lambda < 3 \mu\text{m}$. FIG. 54 shows that our

samples have a very high absorptance in this wavelength range, especially for Pt and Ti. An ideal solar energy absorber should not only absorb solar energy efficiently in this wavelength range but also minimize radiative thermal loss to the environment at longer wavelengths. Therefore, the ideal wavelength dependent reflectance should be $R(\lambda) = 0$ at $0.3 < \lambda < 3 \mu\text{m}$ and $R(\lambda) = 1$ at $3 < \lambda < 50 \mu\text{m}$. A dashed line in FIG. 54 shows this ideal reflectance. To provide high reflectance at $\lambda > 3 \mu\text{m}$, the surface structures we created on brass contain shallow microgrooves covered by nanostructures. FIG. 51 shows a comparison of the microgrooves of brass versus Ti and Pt. The microgroove depth is about 10 μm for brass, but 50 and 75 μm for Ti and Pt. Because a shallower microgroove traps less infrared radiation at longer wavelengths, brass has a significantly higher reflectance in the infrared. We believe that a closer resemble of the ideal reflection step function can be achieved by further optimizing the structural period and depth. In some instances, this can be further optimized by reducing groove spacing and depth to the 5-10 μm and 3-5 μm range, respectively. Alternatively, a nanotextured microcolumnar hierarchical surface structure may provide a better structure for achieving the ideal reflection step function.

[0242] In summary, for the first time, we create a multifunctional metal surface by producing a hierarchical nano- and micro-structures with femtosecond laser pulses. The multifunctional surfaces exhibit excellent broadband light absorption, superhydrophobicity, and self-cleaning effects. This surface should also possess other highly desirable functionalities such as anti-corrosion, anti-icing, anti-biofouling, and self-sanitation, since these properties are directly related to superhydrophobicity.

[0243] To produce the hierarchical surface structures described above in the non-limiting examples, we used an amplified Ti:sapphire laser system that generates 65-fs pulses with a central wavelength of 800 nm. The laser beam was focused onto the sample surface by a lens onto a sample mounted on a computerized XY-translation stage. The samples in our study were platinum, titanium, and brass. A scanning electron microscope (SEM) and a 3D laser scanning microscope were used to examine the surface structures. Superhydrophobic properties were studied by measuring both water contact angle and the surface tilt angle for water sliding. The self-cleaning properties were studied with real-life dust particles collected from a vacuum cleaner. For cleaning, we use rolling and falling water drops. The rolling drops with nearly zero kinetic energy are produced by pipetting water drops near the sample surface, while the falling drops are produced by pipetting drops at a height of 3-8 cm above the sample surface. The diameter of the pipetted water drops is in the range of 2-5 mm. The self-cleaning action is recorded with a video camera. To characterize the optical properties, we measure the total hemispherical optical reflection of the samples using a Perkin-Elmer Lambda 900 spectrophotometer and Bruker IFS 66/S FTIR spectrometer, each equipped with an integrating sphere. The two spectrometers allow us to measure the spectral reflectance in the wavelength range of 0.25-2.5 μm and 2.5-16 μm , respectively.

[0244] In some instances, commercial devices may be used to measure the contact angle. In our study, for example, we used a VCA 2500XE video contact angle system. When using such a system, a water droplet is placed on the surface, and an image is taken and an algorithm will be applied to

calculate the contact angle based on the image. Commonly, measurements are performed under normal atmospheric pressure and room temperature. In some instances, measurements are made using clean water, such as distilled water.

[0245] All references, including publications, patent applications, and patents, cited herein are hereby incorporated by reference to the same extent as if each reference were individually and specifically indicated to be incorporated by reference and were set forth in its entirety herein.

[0246] The use of the terms “a” and “an” and “the” and similar referents in the context of describing the invention (especially in the context of the following claims) are to be construed to cover both the singular and the plural, unless otherwise indicated herein or clearly contradicted by context. The terms “comprising,” “having,” “including,” and “containing” are to be construed as open-ended terms (i.e., meaning “including, but not limited to,”) unless otherwise noted. The term “connected” is to be construed as partly or wholly contained within, attached to, or joined together, even if there is something intervening.

[0247] The recitation of ranges of values herein are merely intended to serve as a shorthand method of referring individually to each separate value falling within the range, unless otherwise indicated herein, and each separate value is incorporated into the specification as if it were individually recited herein.

[0248] All methods described herein can be performed in any suitable order unless otherwise indicated herein or otherwise clearly contradicted by context. The use of any and all examples, or exemplary language (e.g., “such as”)

provided herein, is intended merely to better illuminate embodiments of the invention and does not impose a limitation on the scope of the invention unless otherwise claimed.

[0249] No language in the specification should be construed as indicating any non-claimed element as essential to the practice of the invention.

[0250] It will be apparent to those skilled in the art that various modifications and variations can be made to the present invention without departing from the spirit and scope of the invention. There is no intention to limit the invention to the specific form or forms disclosed, but on the contrary, the intention is to cover all modifications, alternative constructions, and equivalents falling within the spirit and scope of the invention, as defined in the appended claims. Thus, it is intended that the present invention cover the modifications and variations of this invention provided they come within the scope of the appended claims and their equivalents.

1. A metal or metal alloy comprising at least one surface region including a plurality of micro-scale structure shapes having a depth or height in the range of 0.1 to 500 μm and a plurality of nano-scale structure shapes having at least one dimension that is less than 1 μm , wherein the at least one surface region is super-hydrophobic having a water contact angle of 150° or greater, wherein the at least one surface portion has a spectral reflectance of less than 60% for at least some wavelengths of electromagnetic radiation in the range of 0.1 μm to 500 μm .

* * * * *